Angular power spectrum of the diffuse gamma-ray emission as measured by the Fermi Large Area Telescope and constraints on its dark matter interpretation

Mattia Fornasa, Alessandro Cuoco, Jesús Zavala, Jennifer M. Gaskins, Miguel A. Sánchez-Conde, German Gomez-Vargas, Eiichiro Komatsu, Tim Linden, Francisco Prada, Fabio Zandanel, and Aldo Morselli

Phys. Rev. D **94**, 123005 — Published 9 December 2016

DOI: 10.1103/PhysRevD.94.123005

The angular power spectrum of the diffuse gamma-ray emission as measured by the *Fermi* Large Area Telescope and constraints on its Dark Matter interpretation

Mattia Fornasa,[1,*] Alessandro Cuoco,[2,†] Jesús Zavala,[3,4,‡] Jennifer M. Gaskins,[1,5] Miguel A. Sánchez-Conde,[6,7] German Gomez-Vargas,[8] Eiichiro Komatsu,[9,10] Tim Linden,[11,12] Francisco Prada,[13,14,15] Fabio Zandanel,[1] and Aldo Morselli[16]

[1] *GRAPPA, University of Amsterdam, Science Park, 1098 XH Amsterdam, Netherlands*
[2] *Institute for Theoretical Particle Physics and Cosmology (TTK), RWTH Aachen University, D-52056 Aachen, Germany*
[3] *Dark Cosmology Centre, Niels Bohr Institute, University of Copenhagen, Juliane Maries Vej 30, 2100 Copenhagen, Denmark*
[4] *Center for Astrophysics and Cosmology, Science Institute, University of Iceland, Dunhagi 5, 107 Reykjavik, Iceland*
[5] *California Institute of Technology, Pasadena, California, 91125, United States of America*
[6] *The Oskar Klein Centre for Cosmoparticle Physics, AlbaNova, SE-106 91 Stockholm, Sweden*
[7] *Department of Physics, Stockholm University, AlbaNova, SE-106 91 Stockholm, Sweden*
[8] *Instituto de Astrofisíca, Pontificia Universidad Catolica de Chile, Avenida Vicuna Mackenna 4860, Santiago, Chile*
[9] *Max-Planck-Institut für Astrophysik, 85740 Garching bei München, Germany*
[10] *Kavli Institute for the Physics and Mathematics of the Universe (Kavli IPMU, WPI), Todai Institutes for Advanced Study, The University of Tokyo, Kashiwa 277-8583, Japan*
[11] *University of Chicago, Kavli Institute for Cosmological Physics, Chicago, Illinois, 60637, United States of America*
[12] *Ohio State University, Center for Cosmology and AstroParticle Physcis (CCAPP), Columbus, Ohio, 43210, United States of America*
[13] *Instituto de Física Teórica, (UAM/CSIC), Universidad Autónoma de Madrid, Cantoblanco, E-28049 Madrid, Spain*
[14] *Campus of International Excellence UAM+CSIC, Cantoblanco, E-28049 Madrid, Spain*
[15] *Instituto de Astrofísica de Andalucía (IAA-CSIC), Glorieta de la Astronomía, E-18008, Granada, Spain*
[16] *Istituto Nazionale di Fisica Nucleare, Sezione di Roma "Tor Vergata", I-00133 Roma, Italy*

The isotropic gamma-ray background arises from the contribution of unresolved sources, including members of confirmed source classes and proposed gamma-ray emitters such as the radiation induced by dark matter annihilation and decay. Clues about the properties of the contributing sources are imprinted in the anisotropy characteristics of the gamma-ray background. We use 81 months of Pass 7 Reprocessed data from the *Fermi* Large Area Telescope to perform a measurement of the anisotropy angular power spectrum of the gamma-ray background. We analyze energies between 0.5 and 500 GeV, extending the range considered in the previous measurement based on 22 months of data. We also compute, for the first time, the cross-correlation angular power spectrum between different energy bins. We find that the derived angular spectra are compatible with being Poissonian, i.e. constant in multipole. Moreover, the energy dependence of the anisotropy suggests that the signal is due to two populations of sources, contributing, respectively, below and above $\sim$2 GeV. Finally, using data from state-of-the-art numerical simulations to model the dark matter distribution, we constrain the contribution from dark matter annihilation and decay in Galactic and extragalactic structures to the measured anisotropy. These constraints are competitive with those that can be derived from the average intensity of the isotropic gamma-ray background.

I. INTRODUCTION

In 2012, the *Fermi* Large Area Telescope (LAT) Collaboration measured for the first time the auto-correlation angular power spectrum (auto-APS) of the diffuse gamma-ray emission detected far from the Galactic plane [1]. In that analysis, point sources in the first *Fermi* LAT source catalog (1FGL) [2] and a band along the Galactic plane with Galactic latitude $|b| < 30^\circ$ were masked in order to isolate the contribution to the auto-APS from the so-called Isotropic Gamma-Ray Background (IGRB).

* fornasam@gmail.com
† cuoco@physik.rwth-aachen.de
‡ jzavala@dark-cosmology.dk; Marie Curie Fellow

The IGRB is what remains of the gamma-ray sky after the subtraction of the emission from resolved sources and from the Galactic diffuse foreground induced by cosmic rays [3, 4]. It dominates the gamma-ray sky at large Galactic latitudes and its intensity energy spectrum is found to be compatible with a power-law with a slope of 2.32 ± 0.02 between 100 MeV and ∼300 GeV, and with an exponential cut-off at higher energies [4]. These values for the spectral slope and for the energy cut-off are those found when "model A" from Ref. [4] is used to describe the Galactic diffuse foreground emission. A different foreground model for the Galaxy would lead to a slightly different energy spectrum for the IGRB. Deviations can be as large as 20-30% depending on energy.

The IGRB is interpreted as the cumulative emission of sources (e.g., blazars, star-forming and radio galaxies) that are too faint to be detected individually (see Ref. [5] for a recent review and the references therein)[1]. Yet, its exact composition remains unknown. It is expected to be isotropic on large angular scales but it can still contain anisotropies on small angular scales. Indeed, the contribution to the IGRB from unresolved sources imprints anisotropies in the diffuse emission which can be used to infer the properties of the contributing sources (see Refs. [6–15] among others). For example, the detection of a significant angular power in Ref. [1] determined an upper limit to the contribution of unresolved blazars [10, 11, 16] to the IGRB. Additional tools to reconstruct the nature of the IGRB are the study of its cross-correlation with catalogs of resolved galaxies [17–22], with gravitational lensing cosmic shear [23] and with lensing of the cosmic microwave background radiation [24]. Complementary information can also be inferred by modeling its 1-point photon count distribution [25–27].

The detection of the auto-APS presented in Ref. [1] was based on ∼22 months of data. Since then, *Fermi* LAT has increased its statistics by approximately a factor of 4. Therefore, we expect that an updated measurement of the auto-APS will significantly improve our understanding of the IGRB. In the first part of this work, we perform this measurement by analyzing 81 months of *Fermi* LAT data from 0.5 to 500 GeV, extending the 1-50 GeV energy range considered in Ref. [1]. This enables a more precise characterization of the energy dependence of the auto-APS. Indeed, looking for features in the so-called "anisotropy energy spectrum" is a powerful way to single out different components of the IGRB [28]. We also compute, for the first time, the cross-correlation angular power spectrum (cross-APS) of the diffuse gamma-ray emission between different energy bins. The cross-APS additionally enhances our ability to break down the IGRB into its different components since it provides information about the degree of correlation of the emission at different energies, which is stronger if the emission originates from one single source population (see, e.g., Ref. [29, 30]).

In the second part of this paper, we focus our analysis on one possible contributor to the IGRB, namely the emission induced by dark matter (DM). If DM is a weakly-interacting massive particle (WIMP), its annihilation or decay could generate gamma rays. The radiation produced in extragalactic and Galactic DM structures could contribute to the IGRB (see Ref. [5] and references therein) and, therefore, the IGRB could be used to indirectly search for non-gravitational DM interactions. Indeed, both the measurement of the IGRB energy spectrum [4] and of its auto-APS [1] have been already used to set constraints on the possible DM-induced gamma-ray emission [14, 31–33].

In this work, we also update the predictions for the auto- and cross-APS expected from DM annihilation or decay with respect to Ref. [34]. The distribution and properties of DM structures are modeled according to the results of state-of-the-art N-body cosmological simulations. We also employ well-motivated semi-analytical recipes to account for the emission of DM structures below the mass resolution of the simulations. The latter is a significant part of the expected signal, at least in the case of annihilating DM. We take special care to estimate the uncertainties introduced when modeling the clustering of DM, especially at the smallest scales. Our predicted DM signal is then compared to the updated *Fermi* LAT measurement of the auto- and cross-APS. In the most conservative scenario, this comparison provides an upper limit to the gamma-ray production rate by DM particles, i.e. an upper limit to its annihilation cross section or a lower limit to its decay lifetime, as a function of DM mass.

The paper is organized as follows: in Sec. II we provide details on the data set that will be used in Sec. III, where we describe our data analysis pipeline. We validate the latter in Sec. IV A on Monte Carlo (MC) simulations of the unresolved gamma-ray sky. In Sec. V, we present our results for the auto- and cross-APS, and we describe the validation tests performed. Sec. VI provides a phenomenological interpretation of our results in terms of one or multiple populations of gamma-ray sources. In Sec. VII we focus on DM-induced gamma-ray emission: we provide details on how this signal is simulated, distinguishing among different components and discussing the main uncertainties affecting its calculation. In Sec. VIII the auto- and cross-APS expected from DM are compared to the measurements and exclusion limits are derived. Finally, Sec. IX summarizes our conclusions.

[1] Instead, the sum of the emission from the resolved and unresolved sources is generally referred to as the Extragalactic Gamma-ray Background.

II. DATA SELECTION AND PROCESSING

The data analysis pipeline proceeds similarly to what is described in Ref. [1]. We use Pass 7 Reprocessed *Fermi* LAT data taken between August 4 2008 and May 25 2015 (MET Range: 239557417 – 454279160), and restrict ourselves to photons passing the ULTRACLEAN event selection. Thus, we use P7REP_ULTRACLEAN_V15 as the instrument response functions (IRFs). We place standard selection cuts on the *Fermi* LAT data, removing events entering the detector with a zenith angle exceeding 100°, events recorded when the *Fermi* LAT instrument was oriented at a rocking angle exceeding 52° and events recorded while the *Fermi* LAT was passing through the South Atlantic anomaly, or when it was not in science survey mode. Since photons which pair-convert in the front of the *Fermi* LAT detector have a better angular resolution, we split our data set into front- and back-converting events, running each data set through the same data analysis pipeline. The front-converting events will represent our default deta set, with the corresponding P7REP_ULTRACLEAN_V15 IRF. To produce flux maps we bin the resulting *Fermi* LAT event counts and exposure maps into HEALPix-format maps[2] [35] with angular bins of size ∼0.06° (HEALPix order 10, `Nside`=1024), as well as into 100 logarithmically-spaced energy bins spanning the energy range between 104.46 MeV and 1044.65 GeV. The conversion of the exposure maps into HEALPix-format maps is performed with the GaRDiAn package [36]. Flux maps are, then, built by dividing the count map by the corresponding exposure map, in each energy bin. The flux maps obtained with the fine energy binning are later co-added into 13 larger bins spanning the energy range between 500 MeV and 500 GeV. This is done to ensure sufficient statistics within each energy bin. We use the smaller energy bins to calculate the beam window function and the photon noise within each larger energy bin, as described in Sec. III.

III. ANISOTROPY ANALYSIS

A. Auto- and cross-correlation angular power spectra

An intensity sky map can be decomposed into spherical harmonics as follows:

$$I(\psi) = \sum_{\ell m} a_{\ell,m} Y_{\ell,m}(\psi), \tag{1}$$

where $I(\psi)$ is the intensity from the line-of-sight direction ψ and $Y_{\ell,m}(\psi)$ are the spherical harmonic functions. The auto-APS C_ℓ of the intensity map is given by the $a_{\ell,m}$ coefficients as:

$$C_\ell = \frac{1}{2\ell+1} \sum_{m=-\ell}^{\ell} |a_{\ell,m}|^2. \tag{2}$$

Similarly, the cross-APS between two intensity maps I_i and I_j is constructed from the individual $a^i_{\ell,m}$ and $a^j_{\ell,m}$ coefficients, obtained from the decomposition in the two energy bins, independently:

$$C^{ij}_\ell = \frac{1}{2\ell+1} \sum_{m=-\ell}^{\ell} a^i_{\ell,m} a^{j\star}_{\ell,m}. \tag{3}$$

The auto- and cross-APS are computed with specific numerical tools as, e.g., HEALPix and PolSpice [37]. However, before applying Eqs. 2 and 3, the data set must be prepared, accounting for possible masking, foreground subtraction and pixelization. Additionally the calculations are complicated by the finite angular resolution of the instrument. In the following subsections, we summarize how these aspects are taken into consideration.

B. Masking

We apply a mask to the all-sky data to reduce contamination from Galactic diffuse foregrounds and from sources already detected in the third *Fermi* LAT source catalog (3FGL) [38]. The mask applied in our default analysis

[2] http://healpix.jpl.nasa.gov

excludes low Galactic latitudes ($|b| < 30^\circ$). We also mask each point-like source in 3FGL with a disk whose radius depends on the flux detected from the source between 0.1 and 100 GeV: for the 500 brightest sources we consider a disk with a radius of 3.5°, for the following 500 sources a disk with a radius of 2.5°, a disk with a radius of of 1.5° for the following 1000 sources, and, finally, a radius of 1.0° for the remaining objects. Validation of the choice for the mask will be performed in Sec. V C. The 3FGL catalog contains 3 extended sources at moderate and high latitudes: Centaurus A and the Large and Small Magellanic Clouds. Centaurus A and the Large Magellanic Cloud are each masked excluding a 10°-region from their center in the catalog. We employ a 5°-mask for the Small Magellanic Cloud. The fraction $f_{\rm sky}$ of the sky outside the mask is 0.275.

We also consider an alternative mask that covers the same strip around the Galactic plane but only the sources in the second *Fermi* LAT source catalog (2FGL) [39]. In this case, we mask all the sources with a 2°-radius disk. The validation for this choice is performed in Sec. V C and, in this case, $f_{\rm sky} = 0.309$.

As an illustrative example, the intensity sky maps of the data between 1.0 and 2.0 GeV are shown in Fig. 1, both unmasked (top panel) and with the default mask excluding sources in the 3FGL (bottom panel).

C. Foreground cleaning

Despite applying a generous cut in Galactic latitude, some Galactic diffuse emission remains visible in the unmasked area of the sky map, particularly at low energies (see Fig. 1). To reduce this contamination further, we perform foreground cleaning by subtracting a model of the Galactic diffuse emission. We use the recommended model for Pass 7 Reprocessed data analysis, i.e. `gll_iem_v05_rev1.fit`[3]. Details of the derivation of the model are described in Ref. [40]. This foreground model, together with an isotropic component, is fitted to the data in the unmasked region of the sky and in each one of the 13 coarser energy bins, using GARDIAN. The default mask is adopted when fitting the diffuse components. The resulting best-fit model is then subtracted from the intensity maps in each energy bin to obtain residual intensity maps, on which the anisotropy measurements are performed. Fig. 2 shows an example of the residual intensity map for the data in the energy bin between 1 and 2 GeV.

We investigate the impact of foreground cleaning on the auto- and cross-APS measurements in Sec. V C.

D. Noise and beam window functions

We calculate the auto- and cross-APS of the intensity maps using the POLSPICE package [37] to deconvolve the effect of the mask on the spectra and to provide the covariance matrix for the estimated C_ℓ.

Both the finite angular resolution of the instrument (given by its point-spread function, PSF) and the finite angular resolution of the map (i.e., the pixelization scheme) suppress the measured auto- and cross-APS at large multipoles (i.e. small angular scales). This effect is described using the beam window function $W_\ell^{\rm beam}$ and pixel window function $W_\ell^{\rm pix}$, respectively. We note that they affect the signal but not the noise term $C_{\rm N}$ (see Ref. [1]). We use the beam and pixel window functions to correct the suppression at large multipoles so that our estimation for the auto- and cross-APS is as follows[4]:

$$C_\ell^{{\rm signal},ij} = \frac{C_\ell^{{\rm Pol},ij} - \delta^{ij} C_{\rm N}^i}{(W_\ell^{{\rm beam},i} W_\ell^{{\rm beam},j})(W_\ell^{\rm pix})^2}, \tag{4}$$

where the i and j indexes run from 1 to 13 and label emission in different energy bins. The case $i = j$ corresponds to the auto-APS and the one with $i \neq j$ to the cross-APS between energy bins. Also, $C_\ell^{{\rm Pol},ij}$ is the APS delivered by POLSPICE, which is already corrected for the effect of masking. The noise term $\delta^{ij} C_{\rm N}^i$ is equal to zero for the cross-APS since it is due to shot noise from the finite statistics of the gamma-ray events, which is uncorrelated between different energy bins. We compute $C_{\rm N}^i$ from the shot noise $C_{\rm N}^k$ of the 100 *finely-gridded* intensity maps, where

$$C_{\rm N}^k = \frac{\langle n_{\gamma,{\rm pix}}^k / (A_{\rm pix}^k)^2 \rangle}{\Omega_{\rm pix}}, \tag{5}$$

where $n_{\gamma,{\rm pix}}^k$ and $A_{\rm pix}^k$ are the number of observed events and the exposure, respectively, in each pixel and for the k-th finely-gridded energy bin. The averaging is done over the unmasked pixels. $\Omega_{\rm pix}$ is the pixel solid angle, which is the

[3] http://fermi.gsfc.nasa.gov/ssc/data/access/lat/BackgroundModels.html

[4] In the remainder of the paper, we commonly refer to this estimator simply by C_ℓ instead of $C_\ell^{\rm signal}$.

same for each pixel. See Appendix A for a derivation of Eq. 5. The noise term $C_{\rm N}^i$ for the auto-APS in the i-th large energy bin is given by the sum of the noise terms in Eq. 5 of all the finely-gridded energy bins covered by the i-th bin. We note that Eq. 5 is more accurate than the shot noise used in Ref. [1], i.e. $C_{\rm N} = \langle n_{\gamma,{\rm pix}}\rangle/(\Omega_{\rm pix}\langle A_{\rm pix}^2\rangle)$.

The beam window function is computed as follows:

$$W_\ell^{\rm beam}(E) = 2\pi \int_{-1}^{1} d\cos\theta P_\ell(\cos(\theta)){\rm PSF}(\theta;{\rm E}), \tag{6}$$

where $P_\ell(\cos(\theta))$ are the Legendre polynomials and ${\rm PSF}(\theta;{\rm E})$ is the energy-dependent PSF for a given set of IRFs, with θ denoting the angular distance in the PSF. We use the *gtpsf* tool in the Science Tools package to calculate the effective PSF, as a function of energy, averaged over the actual pointing and live-time history of the LAT. The beam window functions are calculated separately for the P7REP_ULTRACLEAN_V15 front- and back-converting events. Finally, the pixel window function $W_\ell^{\rm pix}$ is computed using the tools provided in the HEALPix package for `Nside`=1024. Since we use the same map resolution for all maps, the pixel window function does not depend on the energy.

The pixel window function and the beam window function for front and back events are shown separately in Fig. 3, for the P7REP_ULTRACLEAN_V15 IRF at 4 representative energies. They are also available at https://www-glast.stanford.edu/pub_data/552. Note that the pixel window function (short-dashed gray line) has a negligible effect up to multipoles of, at least, ∼500 and it is subdominant with respect to the beam window functions at all multipoles and energies. At energies below ∼0.5 GeV, the beam window function leads to a strong suppression of power for $\ell \gtrsim 100$, even with the front event selection.

Given that the PSF of the *Fermi* LAT varies significantly over the energy range considered in this analysis, and in some cases within the individual energy bins used when computing the auto- and cross-APS, it is necessary to calculate an effective beam window function for each energy bin. Therefore, for the i-th energy bin, we define the average window function $\langle W_\ell^{{\rm beam},i}\rangle$ by weighting Eq. 6 with the intensity spectrum of the events in that bin outside the mask:

$$\langle W_\ell^{{\rm beam},i}\rangle = \frac{1}{I_{\rm bin}} \int_{E_{{\rm min},i}}^{E_{{\rm max},i}} {\rm d}E\, W_\ell^{\rm beam}(E)\, \frac{{\rm d}I(E)}{{\rm d}E}, \tag{7}$$

where $I_{\rm bin} \equiv \int_{E_{{\rm min},i}}^{E_{{\rm max},i}} {\rm d}E\, ({\rm d}I/{\rm d}E)$ and $E_{{\rm min},i}$ and $E_{{\rm max},i}$ are the lower and upper bounds of the i-th energy bin. We approximate the energy spectrum of the data by using the measured differential intensity ${\rm d}I/{\rm d}E$ outside the mask in each intensity map for the finely-binned energy bins.

IV. MONTE CARLO VALIDATION OF THE BINNING OF THE APS AND OF ITS POISSONIAN FIT

A. Auto-correlation angular power spectrum

In this section we describe in detail the procedure used to bin the auto-APS estimated in Eq. 4 into large multipole bins. Binning is required in order to reduce the correlation among nearby C_ℓ due to the presence of the mask.

In contrast with the analysis of Ref. [1], in the present work the binned spectra $\overline{C_l}$ are taken to be the unweighted average of the individual C_ℓ in the bin. Also, the error $\overline{\sigma_\ell}$ on $\overline{C_l}$ is computed by averaging all the entries of the covariance matrix provided by PolSpice in the block corresponding to the bin under consideration. A dedicated set of MC simulations of all-sky data are produced to validate these choices and to additionally test alternative binning schemes. The MC validation procedure is described below.

1. Monte Carlo simulations

The simulations are performed for a single energy bin from 1 to 10 GeV. We assume an underlying population of sources with a power-law source-count distribution, i.e., $dN/dS = A\ (S/S_0)^{-\alpha}$. The parameters A, S_0 and α are fixed to the values 3.8×10^8 cm^2 s sr^{-1}, 10^{-8} cm^{-2}s^{-1} and 2.0, respectively, in agreement with the best-fit results of Ref. [26]. We consider sources with fluxes (in the energy range between 1 and 10 GeV) from 10^{-11} cm^{-2}s^{-1} to 10^{-10} cm^{-2}s^{-1}. The upper value is roughly equal to the 3FGL sensitivity threshold. In this way, the level of anisotropy expected from these sources is roughly equal to that observed in the data when masking the 3FGL sources. The lower value is not crucial since the auto-APS is dominated by the sources just below the detection threshold. From the source count distribution dN/dS, we create a realization of the source population, producing about 40,000 objects

and assigning them random positions on the sky. This creates a map with a Poissonian (i.e., constant in multipole) auto-APS, $C_{\rm P}$, whose value can be computed by summing together the squared flux, Φ_i^2, of all the simulated sources divided by 4π: $C_{\rm P} = \sum_i \Phi_i^2/4\pi$. This is equivalent to the usual way of calculating $C_{\rm P}$ by integrating $S^2 dN/dS$ over the range in flux mentioned above. The resulting Poissonian auto-APS $C_{\rm P}$ is $3.42 \times 10^{-18}\,{\rm cm}^{-4}{\rm s}^{-2}{\rm sr}^{-1}$. This is the nominal auto-APS that we want to recover by applying our analysis pipeline to the simulations.

We use the exposure (averaged in the energy range between 1 and 10 GeV) for 5 years of data-taking to convert the intensity map into a counts map. The map is also convolved with the average PSF for the P7REP_ULTRACLEAN_V15 IRFs for front-converting events (averaged in the 1-10 GeV range, assuming an energy spectrum $\propto E^{-2.3}$). The result is a HEALPix-formatted map with resolution `Nside`=1024 containing the expected emission, in counts, from the simulated sources. Purely isotropic emission is also included by adding an isotropic template to the map, which was also convolved with the IRFs and normalized to give the number of counts expected from the IGRB measured in the 1-10 GeV energy range, including the contamination from residual cosmic rays. For simplicity we did not model the Galactic foregrounds. This final map is then Poisson-sampled pixel-by-pixel 200 times to yield 200 different realizations of the expected counts. The auto-APS of each map is calculated with PolSpice, after applying the default mask used in the analysis of the real data, i.e., excluding the region with $|b| < 30^\circ$ and the sources in 3FGL, even though the simulation does not include those sources. Finally, noise subtraction and beam correction are also applied as described in Sec. III D.

2. *Binning validation*

We first validate our recipe to determine the binned auto-APS. In this case, the standard analytic error σ_ℓ on each C_ℓ (assuming that C_ℓ follows a $\chi^2_{2\ell+1}$ distribution [41]) is:

$$\sigma_\ell = \sqrt{\frac{2}{(2\ell+1)\, f_{\rm sky}}} \left(C_\ell + \frac{C_{\rm N}}{W_\ell^2} \right), \tag{8}$$

with $W_\ell = W_\ell^{\rm beam} W_\ell^{\rm pix}$. We test three approaches to obtain $\overline{C_\ell}$: *i*) computing the weighted average of the C_ℓ in each multipole bin, using $w_\ell = \sigma_\ell^{-2}$ as weight, *ii*) computing the weighted average of the C_ℓ in the bin, with a weight $w_\ell = \sigma_\ell^{-2}$, defining σ_ℓ as in Eq. 8 but *only with the noise term* $C_{\rm N}/W_\ell^2$ and *iii*) computing the unweighted average of the C_ℓ in the bin. Note that in the first approach, the weight w_ℓ depends on the data via the C_ℓ term in Eq. 8, while in the second and third methods there is no dependence on the estimated auto-APS. The first method is the one employed in Ref. [1].

In Fig. 4, we show a histogram of the binned $\overline{C_\ell}$ in the bin between $\ell = 243$ and 317 for the 200 MC realizations. The nominal $C_{\rm P}$ is denoted by the grey vertical solid line. The solid black histogram refers to the case in which no weights are used (method *iii*), while the dashed blue histogram is for the weighted average with weights from Eq. 8 (method *i*). The results for method *ii* (i.e., weighted average but with only the noise term in Eq. 8) are not plotted but they are similar to the solid black histogram. It is clear that binning the data by means of a weighted average which includes the data C_ℓ itself gives a result which underestimates the nominal $C_{\rm P}$. On the other hand, using the unweighted average (as we do in the current analysis) or weighting using only the noise term gives results compatible with the input. The intuitive reason for this bias can be traced to the fact that method *i*) uses the measured auto-APS in the estimation of the error: at each multipole the measured auto-APS fluctuates up and down significantly. If we use Eq. 8 with the measured C_ℓ to weight the data at each multipole, a downward fluctuation of C_ℓ is assigned a smaller error bar and, thus, a larger weight. This will lead to a downward biased $\overline{C_\ell}$. Finally, the histograms also show that the distribution of the $\overline{C_\ell}$ obtained from the MC realizations is, to a good approximation, Gaussian. Indeed, it agrees well with the solid red curve representing a Gaussian distribution centered on the nominal $C_{\rm P}$ and with a standard deviation of $9.3 \times 10^{-19}{\rm cm}^{-4}{\rm s}^{-2}{\rm sr}^{-1}$ (see below).

To assign an error $\overline{\sigma_\ell}$ to the binned auto-APS $\overline{C_\ell}$ we also test three methods: *i*) the unweighted average of σ_ℓ^2 from Eq. 8 in the bin, *ii*) the weighted average of σ_ℓ^2 from Eq. 8 with weight $w_\ell = \sigma_\ell^{-2}$ and *iii*) the average of the covariance matrix computed by PolSpice in the bin[5]. Differently from the estimation of $\overline{C_\ell}$, the three methods for the estimation of $\overline{\sigma_\ell}$ produce similar results. Thus, we decide to choose method *iii*) as our standard prescription. This has also the advantage that, by averaging different blocks of the covariance matrix provided by PolSpice, one can build a covariance matrix for the binned auto-APS. The average of $\overline{\sigma_\ell}$ from method *iii*) in the multipole bin between

[5] PolSpice returns the covariance matrix of the beam-uncorrected C_ℓ, denoted here by $V_{\ell\ell'}$. In method *iii*) the error $\overline{\sigma_\ell}^2$ is defined as $\sum_{\ell\ell'} V_{\ell\ell'}/(W_\ell^2 W_{\ell'}^2 \Delta\ell^2)$, where the sum runs over the ℓ, ℓ' inside each multipole bin and $\Delta\ell$ is the width of the bin.

$\ell = 243$ and 317 over the 200 MC realizations is $9.3 \times 10^{-19}\mathrm{cm}^{-4}\mathrm{s}^{-2}\mathrm{sr}^{-1}$, i.e. the value considered in Fig. 4 for the standard deviation of the red curve. Our validation with MC simulations shows that our estimate of the errors is realiable and that higher-order effects, e.g. those related to the bispectrum and trispectrum discussed in Ref. [42], can be neglected. It remains interesting, nonetheless, to understand if a small bispectrum and trispectrum can be used to independently constrain the sources contributing to the IGRB.

3. Poissonian fit validation

Having validated the binning procedure for the measured auto-APS, we are now interested in fitting the binned auto-APS $\overline{C_\ell}$ with a constant value. Indeed, a Poissonian APS $C_{\rm P}$ (i.e. an APS that is constant in multipole) is a natural expectation for the anisotropies induced by unclustered unresolved point sources. One possibility is to infer $C_{\rm P}$ by minimizing the following χ^2 function:

$$\chi^2(C_{\rm P}) = \sum_\ell \frac{(\overline{C_\ell} - C_{\rm P})^2}{\overline{\sigma_\ell}^2}, \tag{9}$$

where $\overline{C_\ell}$ and $\overline{\sigma_\ell}$ are the the binned data and their errors, as described in the previous section.

A second possibility is to consider a likelihood function $\mathcal{L}$ that, up to a normalization constant, can be written as follows:

$$\log \mathcal{L}(C_{\rm P}) = -\sum_\ell \log(\overline{\sigma_\ell}) - \frac{1}{2}\sum_\ell \frac{(\overline{C_\ell} - C_{\rm P})^2}{\overline{\sigma_\ell}^2}. \tag{10}$$

This expression for the likelihood takes into account the fact that $\overline{\sigma_\ell}$ also depends on $C_{\rm P}$, since $\overline{\sigma_\ell}^2$ in Eq. 10 is defined as the average of

$$\sigma_\ell^2 = \frac{2}{(2\ell+1) f_{\rm sky}} \left(C_{\rm P} + \frac{C_{\rm N}}{W_\ell^2}\right)^2, \tag{11}$$

over the specific multipole bin. In fact, for large multipoles, the expected $\chi^2_{2\ell+1}$ distribution of a given C_ℓ can be approximated by a Gaussian for which *the mean and the standard deviation are not independent* but related as in Eq. 11. Thus, the main difference between the χ^2 minimization (as in Eq. 9) and the likelihood method is that, in the latter, $\overline{\sigma_\ell}$ depends on $C_{\rm P}$. Ignoring such a dependence may bias the result of the fit.

The two methods described above are used to determine the best-fit $C_{\rm P}$ for the 200 MC realizations described above, by considering 10 $\overline{C_\ell}$ in 10 bins in multipole uniformly spaced in $\log \ell$ between $\ell = 49$ and 706. As we discuss in Sec. V, this multipole range excludes the large angular scales where the reconstructed C_ℓ are most uncertain due to possible contamination of the Galactic foreground, and the high-multipole range where the effect of the window functions becomes too severe. The results are summarized in Fig. 5: the vertical grey line is the nominal $C_{\rm P}$, while the solid black histogram shows the distribution of the $C_{\rm P}$ determined by maximazing the $\log \mathcal{L}$ of Eq. 10 if the binned $\overline{C_\ell}$ are computed with no weights. This approach produces a distribution that is approximately Gaussian and centered on the nominal $C_{\rm P}$. On the other hand, if the binned $\overline{C_\ell}$ are computed with the weights from Eq. 8, then the maximization of $\log \mathcal{L}$ underestimates the Poissonian auto-APS (long-dashed blue histogram in Fig. 5). Making use of the χ^2 function in Eq. 9 instead of the $\log \mathcal{L}$ in Eq. 10 gives similar results, i.e. an unbiased distribution for $C_{\rm P}$ if the binned $\overline{C_\ell}$ are computed without weights (short-dashed pink line) and an underestimation of the nominal $C_{\rm P}$ when weights are included (not shown in Fig. 5)[6]. The error associated to the best-fit $C_{\rm P}$ corresponds to the 68% confidence-level (CL) region. We note that the $\log \mathcal{L}$ approach yields slightly smaller errors and we decide to adopt this as our standard way to measure the Poissonian auto-APS in the following. The average of the error on the best-fit $C_{\rm P}$ over the 200 MC realizations is $2.6 \times 10^{-19}\,\mathrm{cm}^{-4}\mathrm{s}^{-2}\mathrm{sr}^{-1}$, i.e. the value used as the standard deviation for the Gaussian function plotted as the solid red line in Fig. 5, which is centered on the nominal $C_{\rm P}$.

[6] Note that applying the $\log \mathcal{L}$ or the χ^2 approach to the unbinned C_ℓ provided by PolSpice also leads to an underestimation of $C_{\rm P}$.

B. Cross-correlation angular power spectrum

Similar checks to what is described above for the auto-APS are performed for the cross-APS between two energy bins. In this case, the standard analytical error is:

$$\sigma_\ell^2 = \frac{1}{(2\ell+1)\, f_{\rm sky}} \left[C_\ell^2 + \left(C_{1,\ell} + \frac{C_{1,\rm N}}{W_{1,\ell}^2} \right) \left(C_{2,\ell} + \frac{C_{2,\rm N}}{W_{2,\ell}^2} \right) \right], \tag{12}$$

where C_ℓ is the cross-APS and $C_{1,\ell}$ and $C_{2,\ell}$ are the auto-APS for the two energy bins. Similarly, $W_{1,\ell}$ and $W_{2,\ell}$ are the window functions for the two energies considered and $C_{1,\rm N}$ and $C_{2,\rm N}$ are the two photon noises. After testing different averaging schemes, we decide to use the same method as for the auto-APS case, i.e. to bin the cross-APS with an unweighted average and to estimate $\overline{\sigma_\ell}$ by computing the block-average of the covariance matrix provided by PolSpice.

Similarly, we tested the likelihood and χ^2 approach to derive the Poissonian best-fit $C_{\rm P}$ to the cross-APS data. For the likelihood approach, $\overline{\sigma_\ell}^2$ is now defined as the average of Eq. 12 after having replaced C_ℓ by $C_{\rm P}$. As for the auto-APS, we find compatible results between the two methods, with the likelihood approach providing slightly smaller errors. Therefore, in the following, we will quote Poissonian cross-APS derived with this method.

We end this section by noting that the proper way to estimate $C_{\rm P}$ for the cross-APS would be to use the likelihood method but replacing the auto-APS $C_{1,\ell}$ and $C_{2,\ell}$ in Eq. 12 with their Poissonian estimates $C_{1,\rm P}$ and $C_{2,\rm P}$, and to perform a joint likelihood fit to all three quantities, i.e. $C_{\rm P}$, $C_{1,\rm P}$ and $C_{2,\rm P}$. However, this approach would not provide results that are significantly different than the ones obtained as described above. In fact, at present, the noise terms in Eq. 12 dominate over the signal terms, reducing the effect of covariance between energy bins[7].

V. MEASURED AUTO- AND CROSS-CORRELATION ANGULAR POWER SPECTRA OF THE ISOTROPIC GAMMA-RAY BACKGROUND

Following the analysis described in the previous section, we measure the auto- and cross-APS in 13 energy bins spanning the energy range between 500 MeV and 500 GeV.

A. Auto-correlation angular power spectra

The auto-APS of the IGRB is shown in Fig. 6 for two representative energy bins. The auto-APS for all 13 energy bins considered is shown in Appendix B and it is available at https://www-glast.stanford.edu/pub_data/552. The y-axis range of Fig. 6 and in Appendix B has been chosen to better illustrate the auto-APS in the multipole range of interest, i.e. between ℓ =49 and 706, divided into 10 bins equally spaced in $\log \ell$. The red circles indicate the auto-APS for our reference data set (i.e., P7REP_ULTRACLEAN_V15 front events) and the default mask covering the region with $|b| < 30^\circ$ and 3FGL sources, as described in Sec. III B. Instead, the blue triangles refer to the same data set but using the default mask covering only 2FGL sources (see Sec. III B). Note that the blue triangles are systematically higher than the red circles, due to the anisotropy power associated with the sources that are present in 3FGL but still unresolved in 2FGL.

Fig. 7 shows the auto-APS for the two same energy bins but over a broader multipole range, i.e. from $\ell = 10$ to 2000. This illustrates the behavior of the auto-APS above and below the signal region used in our analysis, i.e. between $\ell = 49$ and 706. At large scales (i.e., low multipoles), there might be some residual contamination from the Galactic foregrounds. This motivates our choice of neglecting the APS below $\ell = 49$. In Sec. V C the effect of foreground contamination is discussed in more detail. On the other hand, at high multipoles and at low energies (left panel), the size of the error bars increases dramatically due to the strong signal suppression caused by the beam window functions. Our signal region neglects any $\overline{C_\ell}$ above 706. At high energies (right panel), the effect of the beam window function is more modest, even up to $\ell = 2000$ (see Fig. 3). In principle, for high energies, we could consider a signal region in multipole that extends to smaller scales. However, we prefer to work with a window in multipole that is independent of the energy bin and, therefore, we choose the value of $\ell = 706$ as a reasonable compromise.

Note that each individual data point in Figs. 6 and 7 can be negative, since our auto-APS estimator quantifies the excess of power with respect to the photon noise $C_{\rm N}$. We fit the auto-APS (between $\ell = 49$ and 706) in each energy

[7] The noise terms in Eq. 12 are a factor of 4-5 larger than $C_{\rm P}$, $C_{1,\rm P}$ and $C_{2,\rm P}$. Therefore, not performing the joint likelihood fit as described in the text generates an error of, at most, 10-20% on σ_ℓ. The effect on the estimated best-fit Poissonian auto- and cross-APS will be even smaller.

bin to a constant value, in order to determine the Poissonian $C_{\rm P}$ (the possibility of a non-constant $\overline{C_\ell}$ is considered later). The fit is performed as discussed in the previous section. The best-fit $C_{\rm P}$ are reported in Tabs. I and II for the different energy bins and for the masks around 3FGL and 2FGL sources, respectively. They are also available at https://www-glast.stanford.edu/pub_data/552 and they are reported as the solid red and dashed blue lines in Figs. 6, 7, 29 and 30, when masking sources in 3FGL and 2FGL, respectively. In the former case, we also show the estimated 68% CL error on $C_{\rm P}$ as a pink band. The significance of the measured Poissonian auto-APS can be quantified by computing the Test Statistics (TS) of the best-fit $C_{\rm P}$, defined as the difference between the $-2\ln\mathcal{L}$ of the best fit and the $-2\ln\mathcal{L}$ of the null hypothesis. The latter is obtained from Eq. 10 by setting $C_{\rm P}$ to zero. Assuming Wilks' theorem, TS is distributed as χ^2 distribution with 1 degree of freedom and, thus, it can be used to estimate the significance associated to $C_{\rm P}$. For the default data set masking 3FGL sources, the significance of the measured auto-APS $C_{\rm P}$ is larger than 3σ for all energy bins up to 21.8 GeV, except between 5.00 and 10.45 GeV. The significance of the detection is reported in italics in Tabs. I and II. In the case of the mask around 3FGL sources, the highest significance in the auto-APS is 6.3σ and it is reached in the second energy bin, i.e. between 0.72 and 1.04 GeV.

The way the auto- and cross-APS depend on the energy (i.e. the so-called "anisotropy energy spectrum") is an informative observable that can provide insight into the emission causing the anisotropic signal. In fact, in the case that the auto-APS is produced by a single population of sources, the anisotropy energy spectrum allows their energy spectrum to be reconstructed [28, 43, 44][8]. If more than one class of objects are responsible for the signal, then, by detecting features in the anisotropy energy spectrum, it may be possible to identify energy regimes where the different classes dominate the signal.

The measured anisotropy energy spectrum for the auto-APS is shown in Fig. 8. In the figure, the data points are weighted by $E^4/\Delta E^2$ where E is the log-center of the energy bin and ΔE is the width of the bin. This weighting is introduced in order to compare the anisotropy energy spectrum directly with the squared intensity energy spectrum of the sources responsible for the anisotropy signal. Fig. 8 compares the auto-APS $C_{\rm P}$ for the case of the mask excluding 3FGL sources (red circles) to that of the mask excluding 2FGL sources (blue triangles). As already mentioned, the amplitude of the auto-APS is lower when we exclude the sources in 3FGL. In both data sets, the low-energy part of the spectrum appears generally consistent with a power law, while a feature is apparent around 7 GeV. We comment further on the structure of the anisotropy energy spectrum in Sec. VI.

B. Cross-correlation angular power spectra

Two examples of the cross-APS between energy bins are shown in Fig. 9. The left panel is for the cross-APS between bins at low energies. A clear correlation is detected in the multipole range of interest (bounded by the vertical grey lines in the figure). Note the effect of the beam window function on the error bars at high multipoles, as in Fig. 7. The right panel shows the cross-APS between two high-energy bins. This combination does not correspond to a significant detection, as the best-fit $C_{\rm P}$ is compatible with zero at a 2σ level.

The best-fit $C_{\rm P}$ for the cross-APS between the i-th and the j-th energy bins are shown in Appendix C, multiplied by $E_i^2 E_j^2/\Delta E_i \Delta E_j$ and for all the possible combinations of energy bins. Cross-APS $C_{\rm P}$ is detected in most combinations of energy bins, with the ones failing to yield a detection mainly involving the two highest energy bins. Tabs. I and II report the detected cross-APS with their significance[9] The largest detection significance is 7.8σ for the case of the cross-APS between the energy bin from 1.99 and 3.15 GeV and the energy bin between 3.15 and 5.0 GeV.

The tables also report in bold the χ^2 associated with the best-fit $C_{\rm P}$ according to the definition in Eq. 9. Fig. 10 shows the distribution of the 91 χ^2 of best-fit $C_{\rm P}$ in the 91 independent combinations of the 13 energy bins. The solid black line refers to the case when all sources in the 3FGL are masked and the dashed blue line when only sources in the 2FGL are masked. Both distributions are compatible with that of a χ^2 distribution with 9 degrees of freedom (i.e. the 10 data points inside the signal region in multipole minus 1 fitted parameter). The latter is represented by a solid red line in Fig. 10. Only 3 (4) combinations of energy bins have a χ^2 larger than 16.9 (that would correspond to a p-value of 0.05) when masking 3FGL (2FGL) sources.

Together with the auto-APS in Fig. 8, the cross-APS provides an important handle to characterize the emission responsible for the anisotropy signal. In particular, if the latter is due to only one class of unresolved sources, the auto-APS $C_{\rm P}^{i,i}$ allows us to reconstruct their energy spectrum and the cross-APS can be *predicted* as $C_{\rm P}^{i,j} = \sqrt{C_{\rm P}^{i,i} C_{\rm P}^{j,j}}$. Alternatively, if we define the so-called cross-correlation coefficients $r_{i,j}$ as $C_{\rm P}^{i,j}/\sqrt{C_{\rm P}^{i,i} C_{\rm P}^{j,j}}$, any deviation from 1 when

[8] The anisotropy energy spectrum traces the intensity energy spectrum of the sources responsible for the anisotropy signal only if the clustering of the source population is independent of energy.

[9] Note that in some cases the best-fit $C_{\rm P}$ is negative. However, whenever that happens the estimated error is large and the measurement is compatible with zero.

$i \neq j$ can be interpreted as an indication of multiple source classes contributing to the signal. In Fig. 11, we show the cross-correlation coefficients corresponding to the best-fit $C_{\rm P}^{i,j}$ for the data set obtained masking 2FGL sources (left panel) and masking 3FGL sources (right panel). In the former case, it is clear that the cross-correlation coefficients of low-energy bins are systematically smaller than 1, when correlated with high-energy bins. This is in qualitative agreement with the findings of Ref. [16], in which the auto-APS measured in Ref. [1] was explained by the sum of two different populations of unresolved blazars at low energies, while, above ∼10 GeV, the signal was compatible with only one source class. Figs. 33 and 34 in Appendix D show, for each energy bin i, how the cross-correlation coefficents $r_{i,j}$ depend on energy E_j.

When 3FGL sources are masked (right panel) the situation is less clear as errors are larger (especially at high energies) and the estimated $C_{\rm P}$ more uncertain. We further discuss about the nature of our auto- and cross-APS in Sec. VI. Note that in some cases the coefficients $r_{i,j}$ shown in Fig. 11 are larger than 1, since only the best-fit values are plotted. They are, however, compatible with 1, within their uncertainty. Also, some coefficients are negative (and they are associated with a black pixel). Although within the error bars these negative $r_{i,j}$ are actually compatible with 0, we note that negative values are allowed, in the case of anti-correlations between two energy bins.

We finish this section by studying whether the binned auto- and cross-APS $\overline{C_\ell}$ are better described by an APS that changes with multipole, instead of a constant value. We fit the binned $\overline{C_\ell}$ with a power law[10], i.e., $C_\ell = A(\ell/\ell_0)^{-\alpha}$, with $\ell_0 = 100$. We leave the normalization A free to vary independently in all the 91 combinations of energy bins but we consider one common slope[11], i.e. α. The best-fit value of α is -0.06 ± 0.08 and it corresponds to a χ^2 per degree of freedom of 0.91. This should be compared to the global (i.e. for all the 91 combinations of energy bins) Poissonian fit, with also has a χ^2 per degree of freedom of 0.91. Therefore, we cannot deduce any preference for the power-law scenario.

C. Validation studies

We note that the uncertainties reported in the last section only include statistical errors. It is therefore important to estimate any systematic errors as, e.g., those related to the analysis (such as the foreground cleaning and the use of the mask) or to the characterization of the instrument, which may affect the effective area and beam window functions. We discuss possible sources of systematic errors in the following sections.

1. Foreground cleaning

The Galactic diffuse emission is bright, especially at low energies, and generally displays an approximate symmetry around the disk of the Galaxy, leading to excess power at low multipoles, corresponding to large angular scales. The measured auto-APS calculated both with and without performing foreground cleaning is shown in the left panel of Fig. 12 (red dots and blue triangles, respectively) for a selected energy bin at low energy. The default mask and data set are used. The effect of foreground cleaning is dramatic at low multipoles, significantly reducing the measured $\overline{C_\ell}$ below ℓ ∼50. On the other hand, our analysis only considers multipoles larger than $\ell = 49$, where the effect of foreground cleaning is smaller, although still important enough to be non-negligible. Above ℓ ∼150, however, it is clear its impact becomes subdominant, and the APS could be measured even without performed any cleaning. This is confirmed by the right panel of Fig. 12, where the best-fit Poissonian auto-APS for the case with foreground cleaning and our signal region, i.e. ℓ between 49 and 706 (red circles, the same as in Fig.8), is compared to the best-fit $C_{\rm P}$ for the case without foreground cleaning but performing the fit only between $\ell = 143$ and 706 (blue triangles), i.e. neglecting the first four bins in multipole inside our signal region. Errors at low energies are larger for the uncleaned case than for the cleaned one. This is due to the fact that, at low energies, only the few $\overline{C_\ell}$ with $\ell \lesssim 300$ play a role in the determination of the best-fit $C_{\rm P}$, since at larger ℓ the beam suppression is too strong. Therefore, cutting the signal region at $\ell = 143$ means that the best-fit $C_{\rm P}$ is determined only by very few data. Nonetheless, the two cases are found to be in good agreement within their uncertainties at all energies. From this we can conclude that the foreground cleaning is effective even down to $\ell \sim 50$, therefore validating our choice for the signal region in multipole.

Also, from the left panel of Fig. 12, it is clear that the binned APS $\overline{C_\ell}$ without foreground cleaning is characterized by much larger error bars than with cleaning, at least for $\ell \lesssim 150$. The reason for this can be understood by

[10] The fit is performed with MINUIT2 v5.34.14, http://lcgapp.cern.ch/project/cls/work-packages/mathlibs/minuit/index.html.

[11] If the auto- and cross-APS are interpreted as produced by a population of unresolved sources, they can be expressed in terms of the 3-dimensional power spectrum of the density field associated with the sources of the gamma-ray emission [5, 45, 46]. The latter determines the dependence on multipole, hence the shape of the auto- and cross-APS. Normally, the 3-dimensional power spectrum is only mildly dependent on the gamma-ray energy, which is encoded in the "window function". Therefore, the APS associated with different combinations of energy bins is expected to have approximately an energy-independent shape. It is therefore reasonable to assume a constant α.

looking at the covariance matrix of the binned auto-APS: in Fig. 12 the errors on $\overline{C_\ell}$ are simply the square root of the diagonal elements of the covariance matrix, while the full covariance matrix is plotted in Fig. 13, for the data between 1.04 and 1.38 GeV, with (left panel) and without foreground cleaning (right panel). Each pixel in the panels corresponds to a pair of bins in multipole and its color provides the covariance between those two bins. We do not directly plot the covariance matrix but, instead, each element $\sigma_{i,j}$ is divided by the square root of the product of the corresponding diagonal elements $\sqrt{\sigma_{i,i}\sigma_{j,j}}$. The main difference between the two panels is at low multipoles, where the case without foreground cleaning is characterized by a large covariance among different bins. This large covariance causes the diagonal terms at $\ell \lesssim 30$ to correlate with diagonal terms at higher multipoles. But multipoles $\ell \lesssim 30$ are characterized by larger $\overline{C_\ell}$ (and, thus, also larger errors) for the uncleaned data set than for the cleaned one. This translates into large error bars also around around $\ell \sim$50-100, for the case without foreground cleaning.

Therefore, the introduction of the foreground cleaning reduces the intensity of the signal at $\ell \lesssim 50$ and it considerably removes the coupling between multipoles, leading to smaller and weakly correlated estimated errors. It also justifies the use of Eqs. 9 and 10 for the determination of the Poissonian APS, since they are valid only under the hypothesis that covariances are negligible[12].

2. Data selection

Next we consider the impact of our choice of data set. As described in Sec. II, our analysis is based on P7REP_ULTRACLEAN_V15 front events. For comparison, we now show the results for two different event selections using Pass 8 data, i.e., the most recent revision of the event-level *Fermi* LAT reconstruction analysis [47]. In particular, we will use the P8R2_ULTRACLEANVETO_V6 class, designed to reduce the cosmic-ray contamination significantly. We consider separately two event selections, i.e. only Pass 8 front-converting events and the so-called PSF3 events. PSF3 is a new selection available with Pass 8 data and it is characterized by an improved angular resolution. The effective area for the PSF3 events is roughly a factor of two smaller than that for the front events, since PSF3 represents the quartile of events with the best angular resolution, while the front events constitute approximately half the total events gathered by the LAT. The same analysis pipeline applied to the Pass 7 data is employed to the Pass 8 data, including foreground cleaning with the same Galactic diffuse model (refitted to the Pass 8 events outside the mask).

In Fig. 14 we compare the measured auto-APS in one energy bin between the default data set (i.e., Pass 7, denoted by red circles) and the two Pass 8 selections: Pass 8 front-converting events in the left panel (orange squares) and Pass 8 PSF3 in the right panel (blue triangles). The auto-APS is shown over the multipole range between $\ell = 10$ and 2000. The two Pass 8 data sets are overall in good agreement with the default Pass 7 data set in the multipole range used for analysis, marked by the two grey vertical dashed lines in the figure.

In Fig. 15 we show the anisotropy energy spectra for the three data sets discussed above. Their Poissonian auto-APS agree well within the measurement uncertainties in the various energy bins. The sharp drop in $C_{\rm P}$ around $\sim$7 GeV apparent in the Pass 7 data is less significant in the Pass 8 PSF3 data and absent in the Pass 8 front data, suggesting that the feature in the Pass 7 data may be the result of a statistical fluctuation. Also, with Pass 8, the auto-APS around 70 GeV has a larger value than with Pass 7, although the difference is only at the 2σ level and, thus, not very significant. We stress that this is only a qualitative comparison and a more thorough analysis of the Pass 8 data should be performed. With Pass 8, the measurement of the auto-APS and cross-APS is expected to improve in several ways, e.g. taking advantange of the new PSF classes (from PSF0 to PSF3), especially at low energies where the measurement uncertainties in the Pass 7 data are dominated by the suppression induced by the beam window functions and (potentially) by the leaking from bright sources outside the mask (see Sec.V C 3). Also, new data selections are available with Pass 8, characterized by different balances between effective area and cosmic-ray contamination. In fact, the improvement expected from using Pass 8 PSF3 or Pass 8 front data can already been seen in the reduction of the error bars for the blue triangles and orange squared in Fig. 15, with respect to the red circles, especially at around 100 GeV. A detailed study with Pass 8 is beyond the scope of the present analysis and is left for future work.

We further investigate the impact of event selection by comparing the results obtained from the Pass 7 data using front data only (i.e., our default choice) to the results obtained using both the front and back data. Including back-converting events in the analysis has the advantage of increasing the statistics by enlarging the effective area by a factor of $\sim$2. However, the average PSF for the front+back data set is poorer than for the front events alone, leading to a larger suppression due to the beam window function and to a stronger leakage outside the mask from bright point-like sources. In this comparison it should be kept in mind that the data sets are not independent since, by

[12] Note that in Ref. [1] the covariance between multipole bins was not discussed.

definition, the front+back data set contains all the front-converting events. Also, it is important to note that due to the poorer PSF of the front+back data set, our source-masking scheme may not be sufficiently effective for that data set, particularly at low energies where the PSF is broadest (see also the discussion in Sec. V C 3).

The left panel of Fig. 16 shows the auto-APS $\overline{C_\ell}$ in a specific energy bin. Red circles refer to the Pass 7 front data set and the blue triangles to the Pass 7 front+back one. The right panel indicates the Poissonian auto-APS as a function of energy, with the same color code. The measured $\overline{C_\ell}$ is in good agreement between the two data sets at all multipoles in our signal region. The same is true for the Poissonian $C_{\rm P}$, except in the lowest energy bin, where the front+back data yields a significantly higher $C_{\rm P}$. This discrepancy is consistent with the possibility that, for the front+back data set, the mask employed here (covering all sources in the 3FGL) is not big enough to get rid of the emission of the sources at low energies. Note that, also in this case, the significance of the dip at $\sim$7 GeV is strongly reduced.

3. Mask around resolved sources

We now investigate the effect of any possible leakage of emission outside the mask around the resolved sources. We recall that our default mask excludes (in addition to a latitude cut of $|b| < 30^\circ$) a disk with a radius of 3.5° around the 500 brightest sources in the 3FGL catalog, a disk with a radius of 2.5° around the following 500 sources, one with a radius of 1.5° for the following 1000 sources and, finally, a disk with a region with a 1.0°-radius around all the remaining ones. This is what we refer to as our *default* mask when covering the sources in 3FGL. However, in order to validate our choice, we consider four additional masks. They are defined as follows:

- *4°-mask* excludes a disk with a radius of 4° around the 500 brightest sources in the 3FGL catalog, a disk with a radius of 3° for the following 500 sources, one with a radius of 1.5° for the next 1000 sources and one with a radius of 1° for the remaining ones;
- *3.5°-mask* excludes a disk with a radius of 3.5° around the 500 brightest sources in the 3FGL catalog, a disk with a radius of 2.5° for the following 500 sources, one with a radius of 2.0° for the next 1000 sources and a disk with a radius of 1.5° for the remaining ones;
- *2°-mask* covers a disk with a radius of 2.0° around the 500 brightest sources and a disk with a radius of 1.0° around the remaining sources;
- *1°-mask* excludes a disk with a radius of 1.0° around each source.

Our default mask is located between the 2°-mask and the 3.5°-mask, in terms of masked area. The specific details of the masks considered are not the result of an a-priori analysis and, thus, they are somewhat subjective. However, our goal is to identify a reasonable mask that is as small as possible without suffering from leakage from point-like sources. As proved in the following, our default mask provides a suitable choice.

Above few GeV, where the PSF is narrower, we expect the 1°-mask to be sufficient to exclude the emission of the sources detected in 3FGL. However, at low energies some leakage may appear. Results are summarized in Fig. 17. The left panel shows the measured auto-APS in the e nergy bin between 1.04 and 1.38 Gev, for the 1.0°-mask (orange squares), for the 2.0°-mask (blue triangles) and for the default one (red circles). It is clear that there is a significant contamination due to power leakage outside the 1.0°-mask, especially at $\ell < 50$, but up to $\ell \sim 80$. The other two more aggresive masks give consistent results in this energy bin. In the right panel, we plot the anisotropy energy spectrum for the 2°-masks (blue triangle), for the default one (red circle) and for the 3.5°-mask (green squares). While, at high energies, the three cases yield consistent results, the 2°-mask shows still an excess of power in the first energy bin. On the other hand, results for the 3.5°-mask are consistent with our default mask. The anisotropy energy spectrum for the 4°-mask (not shown in Fig. 17 for clarity) is also consistent with the default case. This validates our choice of the latter as our fiducial mask when dealing with 3FGL sources[13].

A similar validation is performed on the mask covering the sources in 2FGL. We find that cutting a 1°-disk around all 2FGL sources leads to some power excess at low energies. However, extending the mask by covering a disk with a radius of 2° for all sources is enough to get rid of the leakage and there is no need of more aggressive masks as for

[13] We also test an additional mask that covers exactly the same region of sky as our default mask for 3FGL sources but it also masks the region around Loop-I and the Galactic Lobes. The best-fit $C_{\rm P}$ with this more aggressive cut are compatible with the default Poissonian $C_{\rm P}$ in Fig. 8, within their statistical errors.

the case of 3FGL sources. This is probably due to the fact that, when masking 2FGL sources, the measured power spectra are intrinsically larger than when masking sources in 3FGL (see Sec. V). Thus, the contimation from leakage has *relatively* a minor impact.

D. Effect of the gamma-ray emission from the Sun

Steady gamma-ray emission from the Sun was detected in the *Fermi* LAT data in Ref. [48] from 0.1 to 10 GeV. Later, Ref. [49] extended the detection up to 100 GeV, also establishing that the flux varies with time and anti-correlates with Solar activity. Gamma rays are produced from the interaction of cosmic rays with the Solar atmosphere [50], as well as from Inverse-Compton (IC) scattering of cosmic-ray electrons and positrons with Solar photons [51–53].

The emission is quite difficult to see by eye because, even if quite significant, it is spread over the path followed by the Sun in the sky, i.e. the ecliptic. However, it may still induce some feature in the auto- and cross-APS. We test this possibility by masking the region of 1.5° above and below the ecliptic. The auto- and cross-APS obtained after having introduced this additional mask are compatible with our default case within their uncertainty. Thus, we conclude that the effect of the Sun on the measured anisotropies is negligible[14].

E. Comparison with previous measurement

We conclude this section by comparing our new measurement to the previous (indeed, the first) anisotropy measurement from Ref. [1]. Our current analysis includes many improvements with respect to the original one, both from the perspective of the data set (as we now use Pass 7 Reprocessed events and IRFs, compared to the Pass 6 events used in Ref. [1]) and in terms of analysis method, including an improved calculation of the noise term $C_{\rm N}$, the deconvolution of the mask (performed now with PolSpice) and a MC-validated procedure to bin the auto-APS in multipoles and to estimate its error. The improved data set also allows us to measure the auto-APS with better precision over a larger multipole range covering the window between $\ell = 49$ and 706, while the analysis in Ref. [1] was restricted to $\ell = 155 - 504$. We also extend the energy range, spanning the interval between 500 MeV and 500 GeV, compared to the original 1–50 GeV range. Moreover, we use an improved diffuse model for foreground cleaning, compared to what was available at the time of Ref. [1].

In Fig. 18 we compare the anisotropy energy spectrum reported in Ref. [1] for the mask covering the sources in 2FGL (grey squares) to our new measurement calculated for the same mask but with our new default data set. We report our results for the 13 energy bins used in this work (blue triangles) and we also compute the auto-APS in the same 4 energy bins used in Ref. [1] (red circles). While there is a slight trend toward a higher $C_{\rm P}$ in our current measurement compared to the original one, we find good consistency with Ref. [1]. The only exception is the highest energy bin of the original analysis, which is lower than the current measurement and inconsistent at about 3σ. Many factors may lead to the small systematic increase of the new $C_{\rm P}$ in the first 3 bins and to the larger difference in the last energy bin. However, we attribute this trend primarily to the way the data are binned in multipole and to the way the Poissonian fit $C_{\rm P}$ is determined. As discussed in Sec. IV A, in this analysis we follow a different procedure with respect to the original analysis in Ref. [1], after having verified that the latter can lead to a downward bias of both the $\overline{C_\ell}$ and the best-fit $C_{\rm P}$.

We end by noting that a concern about the auto-APS in Ref. [1] being somewhat underestimated was raised already in Ref. [55]. However, in that case it was claimed that the correct anisotropy should have been a factor 5-6 larger than the measured one for each energy. In the light of the present analysis, this is true only for the highest energy bin, while for the others the difference is only of 20-30%, and not significant within error bars.

VI. INTERPRETATION IN TERMS OF SOURCE POPULATIONS

In this section we provide a phenomenological interpretation of our measurement in terms of different populations of unresolved sources. The main observables that we consider are the results of the Poissonian fits to the auto- and cross-APS, i.e., the anisotropy energy spectrum.

We assume the sources responsible for the signal to be point-like and unclustered [7, 10, 16, 19], and that they give rise only to a Poissonian auto- and cross-APS. We also assume each population to be characterized by a common

[14] The high-energy emission of the Moon peaked at about 200 MeV, with a similar intensity than the Sun [54]. However, at higher energies, it has an energy spectrum that is steeper than that of the Sun. Therefore, above 500 MeV, the effect of the Moon on the APS measurement is expected to be negligible.

intensity energy spectrum $F_a(E)$. The index a runs over the number of source populations contributing to the signal. The contribution of the a-th source population to the auto-APS will be proportional to $F_a(E_i)^2$, while it will be proportional to $F_a(E_i)F_a(E_j)$ in the case of the cross-APS. Our choice of interpreting the auto- and cross-APS data in a phenomenological way is motivated by the desire to be model-independent. Alternative interpretations in terms of physically-motivated models of astrophysical gamma-ray emitters are on-going. We start by considering one single source population with a power-law spectrum, i.e.

$$F(E) = A \left(\frac{E}{E_0}\right)^{-\alpha}, \tag{13}$$

with $E_0 = 1$ GeV. We fit both the best-fit Poissonian auto- and cross-APS taken from Tab. I, i.e. for the mask around 3FGL sources. This scan and the following ones are performed with MultiNest 3.9 [56–58] with 20000 live-points and a tolerance of 10^{-4} in order to provide a good sampling of the likelihood. The prior probability is chosen to be flat for all free parameters, between -15.0 and -5.0 for $\log_{10}(A)$ (and all the normalizations, measured in $\mathrm{cm}^{-2}\mathrm{s}^{-1}\mathrm{sr}^{-1}$), between 0.0 and 5.0 for the slopes and between 5.0 GeV and 500.0 GeV for the energy breaks (see later). The best-fit solution is reported in Tab. III and is represented by a solid magenta line in the left panel of Fig. 19. The best fit has a χ^2 per degree of freedom which is 1.52, corresponding to a p-value of 0.001.

Alternatively, we also consider a broken power law parametrized as follows:

$$F(E) = \begin{cases} A\,(E/E_0)^{-\alpha} & \text{if } E \geq E_b \\ A\,(E_0/E_b)^{+\alpha-\beta}(E/E_0)^{-\beta} & \text{otherwise} \end{cases}. \tag{14}$$

In this case, the best-fit is reported in Tab. III and shown as a solid blue line in the left panel of Fig. 19. Its χ^2 per degree of freedom is 1.36 with a p-value of 0.01.

Then, we allow for the possibility of two independent populations, starting with the case of two power laws. The best-fit values are reported in Tab. III and the model is represented by the solid yellow line in the right panel of Fig. 19: one population explains the data points below a few GeV and another one reproduces the data at higher energies. The best fit has a χ^2 per degree of freedom of 1.47, corresponding to a p-value of 0.003.

We also consider the possibility of two broken power laws. With a χ^2 per degree of freedom of 1.10, it represents the best description to the data. The model is shown as a solid black line in both panels of Fig. 19: one broken power law reproduces the data at low energies (short-dashed black line) and the other one at higher energies (long-dashed black line). The best-fit solution for the cross-APS is shown in Figs. 31 and 32 in Appendix C.

Finally, we also test the hypothesis of one population emitting as a power law and one as a broken power law. This interpretation is characterized by a χ^2 per degree of freedom of 1.16 (with a p-value of 0.14) and it is represented in the right panel of Fig. 19 by a solid green line. The fit is slightly worse than the case with two broken power laws, especially around 3-4 GeV.

The difference between the χ^2 of the best-fit solution for a model with one population and the same quantity for the model with two populations can be used as a TS to determine whether we can exclude the one-source-population scenario. From the values of the χ^2 in Tab. III, the exclusion is at 95% CL in all cases[15]. We can test how the different interpretations perform also in a Bayesian framework. Indeed, we can define the Bayes Factor B as the ratio of the so-called "evidence" for two competing models (given the data) and it can be used to discriminate between them. In particular, with a $\ln B = 0.5$, there is not a preference between the interpretation with one or two power laws (according to the Jeffrey's scale [59]), while, with a $\ln B = 3.1$, there is a weak preference for the two-broken-power-laws solution over the one-broken-power-law one.

VII. SIMULATING THE GAMMA-RAY EMISSION INDUCED BY DARK MATTER

From this section onwards we focus our attention on the DM-induced gamma-ray emission: we first summarize how we simulate this component, and then we analyze our mock gamma-ray sky maps by computing their auto- and cross-APS. This will constitute our prediction for the APS associated with DM that will be compared to the measured auto- and cross-APS presented in the previous sections.

The simulated DM signal needs to account for all DM structures (halos and subhalos) around us, including the emission generated in the halo of our own Milky Way (MW). We divide the DM auto- and cross-APS into different

[15] In the comparison between one and two populations of sources, if the number of additional degrees of freedom is 2 (as for the case in which the sources in the second population emit as power laws), then the 95% CL exclusion corresponds to a $\Delta\chi^2$ of 5.99. On the other hand, if the second population emits as a broken power law, the number of additional degrees of freedom is 4 and the 95% CL limit is obtained for a $\Delta\chi^2$ of 9.49.

components that are discussed separately in the following subsections (from Sec. VII A to Sec. VII E). We follow closely the semi-analytical procedure developed in Ref. [34], i.e., we directly employ catalogs of DM (sub)halos from N-body simulations and complement them with well-motivated recipes to account for the emission of DM halos and subhalos below the mass resolution of the simulations. As in Ref. [34], we make use of the Millennium-II and Aquarius simulations, from the Virgo Consortium [60–62] to simulate the Galactic and extragalactic components, respectively.

We take particular care in estimating the systematic uncertainties associated with the DM auto- and cross-APS. In particular, each time we introduce a quantity that is not well determined, we consider a reasonable range of variability for it and determine its impact on the final DM signal.

We separately consider gamma-ray emission produced by annihilations or decays of DM particles, organizing our predictions in the form of HEALPix maps with `Nside`=512. This corresponds to 3145728 pixels and an angular size of approximately 0.115°. The order is lower than the one used in the data analysis (see Sec. III). However, note that we will only compare our predictions for the DM signal to the measured spectra below $\ell = 706$, i.e. for angular scales larger than 0.25°.

The gamma-ray flux (in units of $\mathrm{cm}^{-2}\mathrm{s}^{-1}$) produced by DM annihilations in the i-th energy bin and coming from the pixel centered towards direction $\mathbf{n}_j$ can be written as follows:

$$\Phi(E_i, \mathbf{n}_j) = \frac{\langle \sigma_{\rm ann} v \rangle}{8\pi m_\chi^2} \int_{\Delta\Omega_j} d\Omega_{\mathbf{n}} \int_{0.0}^{2.15} dz \, \frac{c(1+z)^3}{H(z)} \rho_\chi^2(z, \mathbf{n}_j) \int_{E_i}^{E_{i+1}} dE_\gamma \frac{dN_\gamma^{\rm ann}(E_\gamma(1+z))}{dE} \exp[-\tau_{\rm EBL}(E_\gamma(1+z))], \quad (15)$$

where the integration $d\Omega_{\mathbf{n}}$ extends over the pixel centered on $\mathbf{n}_j$. For redshifts higher than $\sim$2, the evolution of the DM density field, combined with the larger comoving volume probed attenuates the signal to a negligible level. The interaction with the Extragalactic Background Light (EBL) additionally reduces the emisson from large redshifts[16]. The EBL attenuation is modeled in Eq. 15 by the factor $\exp(-\tau_{\rm EBL}(E_\gamma(1+z)))$, which is taken from Ref. [64]. The thermal average of the cross section times the relative velocity and the mass of the DM particles are expressed by $\langle \sigma_{\rm ann} v \rangle$ and m_χ, while c and $H(z)$ are the speed of light and the Hubble parameter. The function $\rho_\chi(z, \mathbf{n}_j)$ denotes the DM density at redshift z towards the direction $\mathbf{n}_j$. The photon yield $dN_\gamma^{\rm ann}/dE$ determines the number of photons produced per annihilation. Different mechanisms of gamma-ray production contribute to $dN_\gamma^{\rm ann}/dE$. We specify which contribution is included when we discuss the different components of the total DM signal.

In the case of decaying DM, the expected gamma-ray emission is written as follows:

$$\Phi(E_i, \mathbf{n}_j) = \frac{1}{4\pi \, m_\chi \tau} \int_{\Delta\Omega_j} d\Omega_{\mathbf{n}} \int_{0.0}^{2.15} dz \, \frac{c}{H(z)} \rho_\chi(z, \mathbf{n}_j) \int_{E_i}^{E_{i+1}} dE_\gamma \frac{dN_\gamma^{\rm decay}(E_\gamma(1+z))}{dE} \exp[-\tau_{\rm EBL}(E_\gamma(1+z))]. \quad (16)$$

Contrary to Eq. 15, Eq. 16 depends linearly on the DM density and it features the DM decay lifetime τ, instead of $\langle \sigma_{\rm ann} v \rangle$.

A. Extragalactic resolved main halos and subhalos (EG-MSII)

We label halos and subhalos as "resolved" if they are present in the Millennium-II catalog [60] with a mass larger than $6.89 \times 10^8 M_\odot/h$. We employ the same procedure used in Ref. [34] to fill the region below $z = 2.15$ with copies of the original Millennium-II simulation box (see Refs. [29] and [34] for further details). This provides a possible realization of the distribution of resolved extragalactic DM halos and subhalos along the past light-cone. The sky map of their emission (i.e., what we call "EG-MSII" in the following) is obtained by determining, for each pixel in the map, which DM structures fall inside the angular area of the pixel (completely or partially, according to their size) and by summing together their gamma-ray flux. In the case of annihilating DM, the annihilation rate of a DM halo or subhalo is computed from $V_{\rm max}$ and $r_{\rm max}$ (i.e., the maximal circular velocity and the distance from the center of the

[16] Refs. [29, 34, 63] show that more than 90% of the emission is produced below $z = 2$.

halo where this occurs) and by assuming that all DM structures are characterized by a Navarro-Frenk-White (NFW) density profile [65]. A different choice of density profile would affect the overall intensity of the DM-induced emission (by a factor as large as 10, between extreme cases such as the Moore [66] and Burkert [67] profiles [29, 63]) but it would not affect the shape of the auto- and cross-APS since only a relatively small number of the halos in EG-MSII appear as extended, i.e., covering more than one pixel in our sky map. In the case of decaying DM, the decay rate of a halo depends only on its mass, which is independent of the choice of the density profile.

The Millennium-II and Aquarius N-body simulations were performed assuming cosmological parameters favored by WMAP 1. Adopting the most recent values in agreement with the Planck mission [68] could modify the clustering and abundance of DM structures in the simulations. However, it was shown that the increased matter density Ω_m and the decreased linear fluctuation amplitude σ_8 (with respect to WMAP 1) have compensating effects [69] and, therefore, we neglect the dependence of our results on the cosmological parameters (see also Ref. [70]).

As in Refs. [29, 34], the way the copies of the Millennium-II simulation box are positioned around the observer is a random process. Changing their orientation modifies the distribution of resolved DM halos and subhalos, affecting the shape of the auto- and cross-APS for EG-MSII. Ref. [34] showed that this is just a 10% effect that can be neglected in comparison with other sources of uncertainty that will be mentioned later.

For EG-MSII, the photon yield $dN_\gamma^{\rm ann}/dE$ includes the primary gamma-ray emission (taken from Ref. [71]), i.e. hadronization of particles produced in the annihilation, final state radiation and internal bremsstrahlung. We also consider secondary emission, namely the photons up-scattered by the IC of DM-induced electrons onto the cosmic microwave background (see Ref. [34] for details). In the case of decaying DM, the photon yield is determined as $dN_i^{\rm decay}(E)/dE = dN_i^{\rm ann}(2E)/dE$, where i stands for either photons or electrons.

B. Extragalactic unresolved main halos (EG-UNRESMain)

The emission of unresolved main halos (i.e. with a mass smaller than $6.89 \times 10^8 M_\odot/h$) all the way down to the mass of the smallest self-bound halos $M_{\rm min}$, is referred to as "EG-UNRESMain". $M_{\rm min}$ depends on the nature of the DM particle and on its interactions with normal matter but, at least within the context of supersymmetric WIMPs, values between $10^{-12} M_\odot/h$ and 1 $M_\odot/h$ are reasonable, while $M_{\rm min} = 10^{-6} M_\odot/h$ has become a popular benchmark [72, 73].

In order to estimate EG-UNRESMain, we assume that unresolved main halos share the same clustering properties of main halos with a mass between $1.39 \times 10^8 M_\odot/h$ and $6.89 \times 10^8 M_\odot/h$. These main halos are just below our threshold of resolved DM structures. They are barely resolved in the Millennium-II simulations (with a number of particles between 20 and 100) and they populate a regime in mass where the linear halo bias reaches a plateau [60]. Assuming that this remains true even below $1.39 \times 10^8 M_\odot/h$, it is reasonable to think that unresolved main halos will have a similar linear halo bias as the main halos with a mass between $1.39 \times 10^8 M_\odot/h$ and $6.89 \times 10^8 M_\odot/h$. Therefore, their emission can be accounted for simply by artificially enhancing the emission of the main halos between $1.39 \times 10^8 M_\odot/h$ and $6.89 \times 10^8 M_\odot/h$. Such an enhancement is implemented as follows:

$$\int_{M_{\rm min}}^{1.39\times10^8 M_\odot/h} dM \frac{dn_h(M)}{dM} L_h^i(M), \tag{17}$$

where dn_h/dM is the main-halo mass function and $L_h^i(M)$ is the gamma-ray flux produced by a single main halo with mass M. The index i stands for "ann" or "decay", accordingly. The mass function is assumed to follow a power law in mass, down to $M_{\rm min}$. Its normalization and slope are fixed by fitting the abundance of main halos above the mass resolution of Millennium-II, separately in the different snapshots of the simulation, in order to reproduce the redshift dependence of dn_h/dM.

Accounting for the contribution of main halos below the mass resolution of Millennium-II by enhancing the emission of the main halos with a mass between $1.39 \times 10^8 M_\odot/h$ and $6.89 \times 10^8 M_\odot/h$ is equivalent to assuming that the two populations of DM halos share the same spatial distribution. Following the formalism introduced in Ref. [45] this is also equivalent to assuming that they are characterized by the same 2-halo term.

In the case of annihilating DM, the computation of $L_h^{\rm ann}$ in Eq. 17 is very sensivite to the concentration of the halo $c(M, z)$. Contrary to Ref. [34], we consider only the concentration model described in Ref. [74]: this model allows for $c(M, z)$ to flatten as M decreases. Consequently, it agrees with the results of the recent N-body simulations in Refs. [75, 76] and is a more accurate model than the ones from Ref. [77, 78]. At $z = 0$ and for $M_{\rm min} = 10^{-6} M_\odot/h$, Eq. 17 is 24 times larger than the emission of all main DM halos with a mass between $1.39 \times 10^8 M_\odot/h$ and $6.89 \times 10^8 M_\odot/h$. For $M_{\rm min} = 10^{-12} M_\odot/h$ ($M_{\rm min} = 1$ $M_\odot/h$), the number is 28 (15).

For decaying DM, $L_h^{\rm decay}(M, z) = M$ and the enhancement (with respect to the emission of DM halos with a mass between $1.39 \times 10^8 M_\odot/h$ and $6.89 \times 10^8 M_\odot/h$) is 6.7, 6.5 and 5.8 for $M_{\rm min} = 10^{-12}$, 10^{-6} and 1 $M_\odot/h$, respectively.

C. Extragalactic unresolved subhalos

In order to account for the emission of the subhalos of unresolved halos, we modify Eq. 17 as follows:

$$\int_{M_{\rm min}}^{1.39\times10^8 M_\odot/h} dM \frac{dn_h(M)}{dM} L_h^i(M) B^i(M,z). \tag{18}$$

The additional term $B^i(M,z)$ is the so-called boost factor, describing how much the emission of main halos increases when the contribution of their subhalos is included. $B^{\rm decay}$ is equal to 1 for all DM halos and redshifts, while the value of $B^{\rm ann}(M,z)$ is quite uncertain. We consider two scenarios that we believe bracket the current uncertainty on $B^{\rm ann}(M,z)$:

- LOW scenario: this prescription is the same as in Ref. [34] and it is motivated by the parametrization (performed in Ref. [79] and extended in Ref. [80]) of the probability $P(\rho,r)$ of finding a value of the DM density between ρ and $\rho+d\rho$ in the data of the Via Lactea II N-body simulation. For this scenario and at $z=0$, the overall enhancement in Eq. 18 (with respect to the emission of DM main halos with a mass between $1.39\times10^8 M_\odot/h$ and $6.89\times10^8 M_\odot/h$) is 160, 88 and 23 for $M_{\rm min}=10^{-12}$, 10^{-6} and 1 $M_\odot/h$, respectively.

- HIGH scenario: this is the same as the LOW recipe below $10^8 M_\odot/h$ while it predicts a boost factor 5 times larger above that mass. Indeed, recent results favor boost factors that are larger than the ones of the LOW framework. Ref. [81] developed a semi-analytic model that accounts for the mass accretion rate of subhalos in larger host halos. The model also describes the effect of tidal stripping and dynamical friction experienced by subhalos. Including these effects increases the boost factor by a factor of 2-5, relative to the LOW scenario. A similar increase is expected when one accounts for the fact that the concentration of subhalos changes according to the distance of the subhalo from the center of the host halo [82]. Finally, Refs. [83, 84] developed a new statistical method to describe the behaviour of DM particles in collapsed structures, based on the modelling of the so-called Particle Phase-Space Average Density ($\rm P^2SAD$). Ref. [85] demonstrated that, when computed in the case of DM subhalos, the $\rm P^2SAD$ is universal over subhalos of halos with a mass that goes from that of dwarf galaxies to that of galaxy clusters. Employing a reasonable parametrisation of the $\rm P^2SAD$, Ref. [85] found boost factors that are as much as a factor of 5 larger than the LOW case, at least for massive DM halos. The boost factor predicted in Ref. [85] for DM halos with a mass below $10^8 M_\odot/h$ is, however, moderate (see their Fig. 5[17]). Thus, when we compute the emission of unresolved main halos from $10^{-6} M_\odot/h$ to $10^8 M_\odot/h$ as in Eq. 18, and we include the boost factor of Ref. [85], we find a very similar result to that of the LOW scenario. However, predictions are different for massive DM halos: for objects with a mass larger than $10^8 M_\odot/h$ a boost factor 5 times larger than for the LOW case is viable. We assume that such an increment is the same for all masses above $10^8 M_\odot/h$ and we do not concern ourselves with which mechanism (or combinations of mechanisms) is responsible for it among the ones mentioned above, since those studies agree on an increase of this magnitude. For the case with $M_{\rm min}=10^{-12} M_\odot/h$ ($M_{\rm min}=1\ M_\odot/h$), the HIGH boost factor is defined to be a factor 8.4 (2.1) larger than the LOW one (see Fig. 5 of Ref. [84][18]).

As in the case of resolved structures (EG-MSII), the emission of unresolved halos and subhalos is computed including the primary gamma-ray emission and that resulting from the IC scattering off the cosmic microwave background. The total extragalactic signal is defined as the sum of EG-MSII and EG-UNRESMain, boosted for the emission of unresolved subhalos. We refer to the total emission as "EG-LOW" and "EG-HIGH", depending on the subhalo boost factor scheme employed.

D. The smooth halo of the Milky Way (GAL-MWsmooth)

As in Ref. [34], the emission of the smooth halo of the MW (called "GAL-MWsmooth") is modeled by assuming that the MW halo follows an Einasto profile [86]:

$$\log\left(\frac{\rho}{\rho_s}\right) = -\frac{2}{\alpha}\left[\left(\frac{r}{r_s}\right)^\alpha - 1\right]. \tag{19}$$

[17] Note that the boost factor in Ref. [85] is defined in a different way than in Ref. [34]. Whenever we take some information from Ref. [85], we translate it into the same definition used in Ref. [34].

[18] Fig. 5 of Ref. [84] refers to the boost factor of MW-like DM halo. Assuming that similar results apply for all DM halos with a mass larger than $10^8 M_\odot/h$ is therefore an approximation.

The parameters in the above equation that provide the best fit to the data of the highest resolution halo, Aq-A-1, in the Aquarius simulation [61, 62] are: $\rho_s = 7.46 \times 10^{15} h^2 M_\odot/\mathrm{Mpc}^3$, $r_s = 11.05$ kpc$/h$ and $\alpha = 0.170$. This corresponds to a total MW halo mass of $1.34 \times 10^{12} M_\odot/h$, defined as the amount of DM contained in a sphere with an average density of 200 times the critical density of the Universe. Observationally, the mass of the MW DM halo remains uncertain: Fig. 1 of Ref. [87] shows how different methods (including, e.g., MW mass modeling, dynamics of different tracers and the study of the orbits of Andromeda and the MW) suggest values that go from $5.0 \times 10^{11} M_\odot$ to $2.0 \times 10^{12} M_\odot$. Halo Aq-A-1 described above is on the higher end of this range. In order to account for the uncertainty on the MW mass, we assume that ρ_s can vary from its nominal value of $7.46 \times 10^{15} h^2 M_\odot/\mathrm{Mpc}^3$ down to $1.87 \times 10^{10} h^2 M_\odot/\mathrm{Mpc}^3$. The latter corresponds to a MW mass that is 1/4 of the value of Aq-A-1[19]. Note that the intensity of the DM-induced gamma-ray emission is proportional to ρ_s^2 and to ρ_s for an annihilating and decaying DM candidate, respectively. On the other hand, the auto- and cross-APS of GAL-MWsmooth are proportional to ρ_s^4 for annihilation-induced gamma rays and to ρ_s^2 for decaying DM. Thus, the uncertainty on the MW halo mass is a major systematic for the predicted signal we are interested in.

Ref. [61] also showed that a NFW profile provides a reasonable fit to the Aq-A-1 data. We do not consider this alternative here, since the difference compared to the Einasto profile described above would be evident only below $\sim 30^\circ$ from the center of the MW, i.e. in a region located inside the mask considered in the data analysis (see Sec. III B and Refs. [34] and [88]).

In the case of GAL-MWsmooth, the photon yield is computed including primary emission and secondary emission from IC. The latter is computed using a full model for the interstellar radiation field of the MW, as described in Ref. [34], and not just the IC scattering off the cosmic microwave background. We also include the hadronic emission, produced in the interactions of DM-induced protons with the interstellar medium (see Ref. [34]).

E. The subhalos of the Milky Way (GAL-AQ)

The last component to be considered is called GAL-AQ and it accounts for the emission of the subhalos of the DM halo of the MW. We derive this component from the subhalo catalog produced in the Aquarius N-body simulation. Structures with a mass larger than $1.71 \times 10^5 M_\odot$ are treated as "resolved". We place the observer at a distance of $R_0 = 8.5$ kpc from the center of the MW and we compute the sky map of the emission of resolved Galactic subhalos by identifying which subhalos fall within each pixel of the map and summing up their gamma-ray flux. We neglect the contribution of unresolved subhalos (i.e., with a mass smaller than $1.71 \times 10^5 M_\odot$), as they do not contribute to the auto- and cross-APS as argued in Refs.[34] and [89][20].

As in Ref. [34], only the primary gamma-ray emission is considered when computing GAL-AQ.

Depending on the exact position of the observer on the sphere with radius R_0 and centered on the Galactic Center, the distribution of resolved subhalos changes, and so does the intensity of GAL-AQ and its auto- and cross-APS. We estimate this variability by producing 100 realizations of GAL-AQ, changing, each time, the position of the observer on the sphere. We compute the auto- and cross-APS for each realization[21] and note that, for annihilating DM, the 10% quantile of the distribution of the auto-APS (at $\ell = 400$) among the 100 realizations is a factor $\sim$1.5 below the median, while the 90% quantile is a factor $\sim$2.3 above. See the grey band in the left panel of Fig. 20. These numbers are 2.1 and 5.6 (1.4 and 2.2) at $\ell = 49$ ($\ell = 706$). We suspect that the distribution gets more peaked (i.e. less variable) at large multipoles because it becomes more sensitive to the inner structure of DM subhalos (which is constant among the realizations), instead of their distribution in the sky. In the case of decaying DM, the 10% and 90% quantiles are always less than a factor 1.5 away from the median (see the bands in the right panel of Fig. 20). The variability induced by changing the position of the observer is an important component in the total uncertainty of our DM predictions and it will be considered in the following sections.

When discussing GAL-MWsmooth (Sec. VII D), we considered the effect of allowing the MW mass to decrease by a factor 4 with respect to the nominal value of Aq-A-1. This has an impact also on GAL-AQ as the number of subhalos in a DM structure is found to be proportional to the mass of the host halo [90, 91]. If we define k as the fraction by which we decrease the MW mass, we consider 16 values of k, from 0.0 to 0.25. For each k, we randomly remove a fraction k of the subhalos in the Aquarius catalog, to simulate a lighter MW DM halo. For each value of k, we produce 100 realizations of GAL-AQ for different positions of the observer. We compute the auto- and cross-APS for each of the realizations. In Fig. 20, the lines show the median of the distribution of the auto-APS of GAL-AQ (for

[19] Since the observer is located approximately at a distance of R_0=8.5 kpc from the center of the MW, the best-fit Einasto profile to Aq-A-1 corresponds to a local DM density of 0.45 GeV/cm^3. An uncertainty of a factor 4 on ρ_s would generate a variability of the same size on the local DM density.

[20] However, unresolved Galactic subhalos are expected to contribute to the intensity of the DM-induced emission. This should be kept in mind when, in Fig. 23, we compute our predictions for the DM-induced gamma-ray intensity.

[21] Here and for all the sky maps simulating the DM-induced emission, the auto- and cross-APS are computed on the masked gamma-ray sky with the `anafast` routine of HEALPix after having subtracted the monopole and dipole contributions.

a fixed multipole) as a function of k (and, thus, as a function of the MW mass). The left panel is for annihilating DM and the right one for decaying DM. The solid black line is for the auto-APS at $\ell = 400$, while the long-dashed red (short-dashed blue) one is for $\ell = 49$ ($\ell = 706$). The coloured band (when present) denotes the scatter between the 10% and the 90% quantiles in the distribution among the 100 realizations. For annihilating DM (left panel), the band becomes larger as the map is populated by less and less subhalos and, therefore, it depends more and more on their distribution. The variability induced by our partial knowledge of the MW mass is another important source of uncertainty that will be considered in the following sections.

For some values of the DM mass, annihilation cross section and decay lifetime, the gamma-ray flux of some DM subhalos in GAL-AQ may exceed the *Fermi* LAT source sensitivity threshold. These DM subhalos would appear as resolved sources in the sky and they would be included in the 3FGL catalog. Since the auto- and cross-APS are measured masking the sources in 3FGL, DM subhalos that are bright enough to be detected should be neglected when simulating GAL-AQ. Being very bright, they may be responsible for a significant fraction of the auto- and cross-APS of GAL-AQ. Thus, neglecting them may affect significantly our predictions for GAL-AQ, as noticed in Ref. [33][22]. In order to test this, we define the so-called particle physics factors $\Phi_{\rm PP}^{\rm ann}$ and $\Phi_{\rm PP}^{\rm decay}$, which gathers all the terms in Eqs. 15 and 16 that do not depend on the DM distribution. More precisely:

$$\Phi_{\rm PP}^{\rm ann} = \frac{\langle \sigma_{\rm ann} v \rangle}{2 m_\chi^2} \int_{E_{\rm thr}}^{m_\chi} E \frac{dN_\gamma^{\rm ann}}{dE} dE \tag{20}$$

and

$$\Phi_{\rm PP}^{\rm decay} = \frac{1}{m_\chi \tau} \int_{E_{\rm thr}}^{m_\chi/2} E \frac{dN_\gamma^{\rm decay}}{dE} dE, \tag{21}$$

where we choose a reference energy $E_{\rm thr}$ of 0.1 GeV. We consider a reasonable range for the particle physics factors that goes from 10^{-30} to $10^{-25}{\rm cm}^3{\rm s}^{-1}{\rm GeV}^{-1}$ for $\Phi_{\rm PP}^{\rm ann}$ and from 10^{-30} and $10^{-24}{\rm s}^{-1}$ for $\Phi_{\rm PP}^{\rm decay}$[23]. This is divided in 50 logarithmic bins and, for each bin, we build 100 realizations of GAL-AQ, varying the position of the observer. For each particle physics factor and for each realization, we identify the subhalos (if any) with an energy flux above 0.1 GeV that is larger than the sensitivity flux in 3FGL at $|b| > 10^\circ$, i.e. 3×10^{-12}erg cm^{-2}s^{-1} [92]. We consider the energy flux and not the number flux, since the *Fermi* LAT sensitivity, expressed in terms of the energy flux, is more independent of the shape of the gamma-ray energy spectrum than when it is expressed by the number flux. Also, we use the sensitivity obtained for point sources, noting that the majority of the emission in a DM clump comes from a region within its scale radius r_s. In a typical realization of GAL-AQ, almost all resolved DM subhalos have a r_s that corresponds to an angular size smaller than 1 degree. This is a reasonable value for the angular resolution of *Fermi* LAT at the energies of interest here. Thus, DM subhalos in GAL-AQ are rarely extended and the use of the point-source sensitivity is well motivated.

In Fig. 21, the solid lines show the median (over the 100 realizations) of the number of subhalos that have been excluded because they are too bright, as a function of the annihilation (red line, bottom axis) and decay (blue line, top axis) particle physics factor. At the upper end of the range considered for $\Phi_{\rm PP}$, this correction affects between 500 and 2000 DM subhalos for annihilating and decaying DM, respectively. These numbers correspond to approximately 1-2% of the total number of subhalos considered in the Aquarius catalog[24]. The colored bands indicate the variability associated with the 10% and 90% quantiles among the 100 realizations. The dashed vertical lines are included as a reference and they correspond to the particle physics factor for an annihilating DM candidate with a mass of 200 GeV and $\langle \sigma_{\rm ann} v \rangle = 10^{-24}{\rm cm}^3{\rm s}^{-1}$ (dashed red line) and for a decaying DM candidate with the same mass and $\tau = 2 \times 10^{26}$s (dashed blue line). In both cases annihilations/decays into $b\bar{b}$ are considered and the values chosen for $\langle \sigma_{\rm ann} v \rangle$ and τ correspond approximately to their exclusion limits (for $m_\chi = 200$ GeV and for the REF benchmark scenario, see later) as they will be computed in the following sections. This tells us that, for a given DM mass, the allowed region in the parameter space of decaying DM would have almost no DM subhalos that are too bright. On the other hand, the impact of bright subhalos may be important in the case of annihilating DM and this effect will be considered when deriving the exclusion limits on $\langle \sigma_{\rm ann} v \rangle$.

In Fig. 22 we see the effect on the auto-APS of neglecting the DM subhalos in Aquarius that are too bright. The left (right) panel shows the auto-APS at a specific multipole, for an annihilating (decaying) DM candidate as a function

[22] One should also check that none of the DM halos or subhalos in EG-MSII are bright enough to be detected individually. We do not perform such a test because, even if some DM structures were to be removed, this would hardly affect the prediction for the auto- and cross-APS of EG-LOW and EG-HIGH.

[23] For a DM mass of 200 GeV and annihilations (decays) into $b\bar{b}$, the range mentioned above corresponds to a variation between $3.0 \times 10^{-28}{\rm cm}^3{\rm s}^{-1}$ and $3.0 \times 10^{-22}{\rm cm}^3{\rm s}^{-1}$ for $\langle \sigma_{\rm ann} v \rangle$ (between 1.6×10^{23} s and 1.6×10^{29} s for τ).

[24] Note that only 1010 unidentified sources are present in 3FGL [38]. Therefore, a particle physics factor that yields more than 1010 DM subhalos with a flux larger than the 3FGL source sensitivity should be excluded. As we will see in the following sections, the region in the parameter space of DM that is not excluded by the measured auto- and cross-APS does not correspond to those extreme values of particle physics factor.

of $\Phi_{\rm PP}^{\rm ann}$ ($\Phi_{\rm PP}^{\rm decay}$). The auto-APS is multiplied by $(\Phi_{\rm PP}^{\rm ann})^{-2}$ and by $(\Phi_{\rm PP}^{\rm decay})^{-2}$, respectively, so that deviations with respect to a horizontal line indicate how much the auto-APS is suppressed due to the excluded subhalos. Note that the default mask covering the sources in 3FGL is used when computing the auto-APS. The solid black line is for $\ell = 400$, while the red and blue ones are for $\ell = 49$ and $\ell = 706$. They indicate the median over the 100 realizations, while the grey band (sometimes difficult to see because it is too narrow) represents the variablity between the 10% and 90% quantiles. As we anticipated in Fig. 21, the effect of neglecting bright subhalos starts to be important around $10^{-28}{\rm cm}^3{\rm s}^{-1}{\rm GeV}^{-1}$ in the left panel and around $10^{-27}{\rm s}^{-1}$ in the right panel. The same values of the Particle Physics factor marked by the vertical lines in Fig. 21 are plotted in Fig. 22 by the solid grey lines.

The effect of DM subhalos that are too bright is accounted for by defining the following quantity:

$$\kappa(\Phi_{\rm PP}, \ell) = \frac{C_\ell(\Phi_{\rm PP})}{C_\ell(\Phi_{\rm PP}^{\rm min})}, \tag{22}$$

where $\Phi_{\rm PP}^{\rm min} = 10^{-30}{\rm cm}^3{\rm s}^{-1}{\rm GeV}^{-1}$ for annihilating DM and $\Phi_{\rm PP}^{\rm min} = 10^{-30}{\rm s}^{-1}$ for decaying DM. κ is computed by using the median over the 100 realizations. We will employ it as a correction factor to account for the bright DM subhalos that should be masked and it will be multiplied by the APS of GAL-AQ with *all* the DM subhalos.

F. Results

In this section we define some benchmark cases that we will use in the following to discuss our main results:

- REF: this is our reference case and it is constructed by summing EG-MSII and EG-LOW, with $M_{\rm min} = 10^{-6} M_\odot$. We also include GAL-MWsmooth (for the nominal value of the MW DM halo, taken from Aq-A-1, of $1.34 \times 10^{12} M_\odot/h$) and the median of GAL-AQ over the 100 realizations produced for the nominal MW DM halo mass;

- MAX: we build this case by maximizing all the uncertainties considered (and discussed in the previous sections). Thus, we take it as a good estimate of the largest signal that can be associated with DM (for a given value of the particle physics factors and of $M_{\rm min}$). The MAX benchmark is defined by summing EG-MSII, EG-HIGH (for $M_{\rm min} = 10^{-6} M_\odot$), GAL-MWsmooth (for a nominal mass of the MW DM halo) and the 90% quantile among the 100 realizations of GAL-AQ relative to a $1.34 \times 10^{12} M_\odot/h$ MW;

- MIN: contrary to MAX, this benchmark is obtained by tuning all the uncertainties considered above to their minimal configuration. In particular, we sum EG-MSII, EG-LOW (for $M_{\rm min} = 10^{-6} M_\odot$), GAL-MWsmooth (for a MW mass that is 1/4 of the nominal value of Aq-A-1) and the 10% quantile of the 100 realizations of GAL-AQ for a MW mass that is 1/4 of the value of Aq-A-1.

In order to discuss the effect of changing $M_{\rm min}$, we also compute the MIN and MAX benchmarks for $M_{\rm min} = 10^{-12} M_\odot$ and $M_{\rm min} = 1\ M_\odot$.

Fig. 23 shows our predictions for the intensity of the DM-induced emission, averaged over the whole sky. The left panel is for annihilating DM with a mass of 212 GeV and $\langle \sigma_{\rm ann} v \rangle = 3 \times 10^{-26} {\rm cm}^3 {\rm s}^{-1}$, while the right panel is for a decaying candidate with the same mass and $\tau = 2 \times 10^{27}$ s. Annihilations and decays produce gamma rays via $b\bar{b}$. The solid black line is for the REF scenario, while the red and blue ones are for the MIN and MAX benchmark (for $M_{\rm min} = 10^{-6} M_\odot$). Thus, the grey band between the red and blue lines indicates how much our predictions change when accounting for the uncertainties mentioned above.

For annihilating DM, in the case of the REF benchmark, the emission is contributed, almost equally, by EG-LOW and GAL-MWsmooth. Thus, the difference between REF and MAX comes entirely from the different subhalo boost employed to describe unresolved extragalactic DM structures (see Sec. VII C). The boost factor is larger at higher redshifts and, therefore, at energies close to m_χ, where the emission is dominated by nearby sources, the red line approaches the black one. On the other hand, in the LOW scenario the contribution of GAL-MWsmooth is suppressed and, therefore, the intensity of the LOW benchmark is almost halved compared to REF.

Subhalo boosts do not affect the predictions for decaying DM and, therefore, the REF and the MAX benchmarks in the right panel overlap[25]. The lower intensity of the LOW case is, as before, due to the suppression of GAL-MWsmooth.

[25] The contribution of GAL-AQ is subdominant.

In the left panel, the blue and red shaded areas indicate how our predictions for MIN and MAX change when allowing $M_{\rm min}$ to vary in the range mentioned above. These uncertainty bands get larger for smaller energies, as the signal becomes sensitive to the emission at higher redshifts. Changing the minimal DM halo mass has a very minor effect on decaying DM and, thus, the shaded bands are not present.

The predictions of Fig. 23 can be compared with Fig. 12 of Ref. [34]: the main difference is the fact that our brightest configuration (i.e. the MAX scenario) predicts almost one order of magnitude less gamma-ray flux than in Ref. [34], given the new definition of the HIGH subhalo boost factor. On the other hand, our predictions are compatible with the results of Ref. [31].

In Fig. 24 we show the predicted auto-APS in the energy bin between 1.38 and 1.99 GeV, for the same DM candidates considered in Fig. 23. Note that these correspond to particle physics factors that are quite low and therefore none of the DM subhalos in GAL-AQ would be resolved by *Fermi* LAT. We can then neglect the κ correction discussed in Sec. VII E. The left panel is for annihilating DM and the right one for decaying DM. The predicted intensity APS is shown separately for the different components discussed above. We also include the Poissonian auto-APS measured by *Fermi* LAT in the same energy bin (solid black line) and its estimated error (grey band), for the mask around 3FGL sources. To compare the measurement with the predicted DM signal, the latter needs to be corrected for the presence of the mask. In the analysis of the *Fermi* LAT data, this is done automatically by PolSpice (see Sec. III B), while we correct our predictions by dividing the auto- and cross-APS obtained from the masked sky by $f_{\rm sky}$, i.e., the fraction of the sky outside the default mask defined in Sec. III B. Such a recipe is based on the assumption that the masked region is characterised by the same clustering properties of the unmasked one. We test this hypothesis by computing the auto-APS of our simulated sky maps with and without the mask. For the extragalactic signal we find that, indeed, dividing the masked auto-APS by $f_{\rm sky}$, we reproduce the unmasked one. On the other hand, for GAL-AQ, the masked auto-APS is 0.43 times smaller than the unmasked one (approximately at all multipoles). This factor is larger than $f_{\rm sky}$, which suggests that the distribution of DM subhalos outside the mask is slightly more isotropic than the distribution inside the mask. This is to be expected since DM subhalos are more clustered towards the center of the host halo. Finally, the auto-APS of GAL-MWsmooth is significantly different if we include the mask: the intensity of the auto-APS decreases as we are covering the region which produces the majority of the emission. Also, the morphology of the mask induces some spurious fluctuations on the auto-APS. A more sophisticated algorithm should be employed to correct for these features. Alternatively, the wiggles would be reduced by smoothing the edges of the mask. However, we note that, in the signal region defined in Sec. III, the GAL-MWsmooth component is not responsible for the majority of the signal and, therefore, using the reconstructed auto-APS of GAL-MWsmooth would not considerably change our results. Therefore, for both the GAL-AQ and the GAL-MWsmooth, we simply apply the $1/f_{\rm sky}$ correction.

In the left panel of Fig. 24 we note that the dominant contribution is GAL-AQ: the solid blue line is the median over the 100 realizations with different observers (in the case of a MW DM halo with the same mass as Aq-A-1), while the filled blue band shows the variabilty between the 10% and 90% quantiles. If we also include the possibility that the MW DM halo may be up to 4 times lighter (see Sec. VII E and Fig. 20), the uncertainty band extends downwards to include the shaded blue band. Over the signal region, GAL-AQ is not constant and it decreases by approximately a factor of 10. The extragalactic signal is plotted in red and purple, for a LOW and HIGH subhalo boost, respectively. This uncertainty gives rise to the pink band that covers approximately one order of magnitude. The extragalactic component becomes nearly constant for $\ell \gtrsim 300$ but, over the whole signal region, it decreases by a factor of 10. Finally, the GAL-MWsmooth is plotted in green and the green band indicates how much the signal decreases when the mass of MW DM halo is allowed to decrease by up to a factor of 4 with respect to the value of Aq-A-1.

If we had considered $M_{\rm min} = 10^{-12} M_\odot/h$ instead, the intensity of EG-LOW and EG-HIGH would have been approximately 4 times larger, while it would have decreased by a factor 50 if we had considered $M_{\rm min} = 1\ M_\odot/h$. However, since the EG-LOW and EG-HIGH are not dominant components, the effect of changing $M_{\rm min}$ on the total DM signal will not be as large.

In the right panel we follow the same color coding: the main difference with respect to the case of annihilating DM is the fact that the extragalactic contribution dominates the signal for most of the measured signal region. There is no uncertainty associated with the boost factor and, therefore, the red and purple lines coincide. As in the left panel, the auto-APS is nearly constant for $\ell \gtrsim 300$ and it decreases by a factor $\sim$50 overall. Another important difference, with respect to the case of DM annihilation, is the fact that the auto-APS of GAL-AQ is much steeper, decreasing by a factor $\sim$600 from $\ell = 49$ to $\ell = 716$.

Independently of how the different components are summed together[26], producing the different REF, MIN and MAX scenarios described above, the total signal associated with DM is *not* Poissonian but decreases at smaller

[26] In principle, one should include the cross-correlation between the different components considered. We do not expect any correlation between extragalactic and Galactic emission. The cross-correlation between GAL-MWsmooth and GAL-AQ was computed in Ref. [93] and it is at least one order of magnitude below the auto-correlation of GAL-AQ. We neglect it here.

angular scales. This will be crucial when comparing our predictions to the *Fermi* LAT data.

VIII. USING THE AUTO- AND CROSS-APS TO CONSTRAIN DARK MATTER ANNIHILATION AND DECAY

In this section we compare the predictions for the DM-induced auto- and cross-APS obtained in Sec. VII with the updated *Fermi* LAT measurement of the IGRB auto- and cross-APS presented in Sec. V. Such a comparison will allow us to determine whether the data are consistent with a DM interpretation or how we can use them to constrain the nature of DM. We follow two complementary approaches that will be described separately in the following subsections. Neither method finds a significant detection of DM in the auto- and cross-APS data and, therefore, the measurement is used to derive exclusion limits on the intensity of the DM-induced gamma-ray emission, as a function of m_χ.

A. Conservative exclusion limits

This first strategy is motivated by the desire to be conservative. In particular, the DM-induced APS, for any energy bin or combination of bins, must not exceed the measured data. For a certain benchmark case (among REF, MIN and MAX) and for a certain value of $M_{\rm min}$, imposing that constraint will translate into upper limits on the intensity of the DM-induced signal or, by fixing m_χ and the annihilation/decay channel, into upper limits on $\langle\sigma_{\rm ann}v\rangle$ for annihilating DM and into lower limits on τ for decaying DM. We refer to these exclusion limits as "conservative".

We consider 60 values of m_χ between 5 GeV and 5 TeV. For each value of m_χ, we compute the DM-induced auto- and cross-APS in the 13 energy bins defined in Sec. II, for the 3 benchmarks described in Sec. VII F, for 3 annihilation/decay channels (i.e., $b\bar{b}$, $\tau^+\tau^-$ and $\mu^+\mu^-$)[27] and for 3 values of $M_{\rm min}$ (i.e., 10^{-12}, 10^{-6} and 1 $M_\odot$). The APS associated with DM for energy bins i and j is averaged over the signal region in multipole and we require it to be smaller than the Poissonian APS measured for that pair of energy bins plus 1.64 times its error: $\langle C^{i,j}_{\ell,{\rm DM}}\rangle < C^{i,j}_{\rm P} + 1.64\,\sigma_{C^{i,j}_{\rm P}}$. Assuming that the measured $C_{\rm P}$ has a Gaussian probability distribution with a central value of $C_{\rm P}$ and a standard deviation of $\sigma_{C_{\rm P}}$, values further away than 1.64 times $\sigma_{C_{\rm P}}$ from the central value correspond to a cumulative probability distribution larger than 0.95. Thus, excluding them provides a 95% CL exclusion bound. For each m_χ, we take the most stringent limit among all the combinations of energy bins.

Fig. 25 shows the upper limits on the $\langle\sigma_{\rm ann}v\rangle$ (left panel) and the lower limits on τ (right panel), as a function of m_χ, for annihilations/decays into $b\bar{b}$ and for the different benchmark scenarios considered above. The black line is for REF while the blue and red ones are for MIN and MAX. Thus, the grey band represents our total systematic astrophysical uncertainty (for $M_{\rm min} = 10^{-6}M_\odot$) and it is as large as approximately a factor of 5 or 2, for annihilating and decaying DM, respectively. The limits have some wiggles because, depending on the DM mass, the emission peaks at different energies, and different combinations of energy bins are responsible for the exclusion limit. Solid lines are obtained considering all the possible combinations of energy bins, while for the black, blue and red dashed ones only the auto-APS is employed. The figure shows that, at large DM mass and both for annihilating and decaying DM, the exclusion limits are driven by the cross-APS and not by the auto-APS, approximately for $m_\chi > 200$ GeV for annihilating DM and for $m_\chi > 700$ GeV for decaying DM.

In the left panel, the red and blue shaded areas account for the effect of changing $M_{\rm min}$ between $10^{-12}M_\odot$ and 1 $M_\odot$ and they are computed only for the MIN and MAX scenarios. The effect is more important for the MIN case since the emission from extragalactic DM structures contributes more to the total signal in this case (see Fig. 24). If we include the variability on $M_{\rm min}$ in our budget for the systematic uncertainty, the systematic error grows to a factor of 40. Compared to the conservative upper limits on $\langle\sigma_{\rm ann}v\rangle$ derived by the intensity of the IGRB in Ref. [31], our uncertainty is approximately a factor of 2 larger. The long-dashed grey line is the thermal annihilation cross section computed in Ref. [94]. The line marks the beginning of the region where, for WIMP DM, one can find annihilation cross sections that correspond to a relic DM abundance in agreement with the Planck data [68]. Unfortunately, our conservative upper limits do not probe this region, as they are, at least, a factor 3 away from it. Also, the REF upper limit is approximately two orders of magnitude higher than the upper limit derived from the observation of 15 dwarf spheroidal galaxies performed by *Fermi* LAT [95] and included here as a grey dash-dotted line. Finally, it is a factor 2 higher than the conservative limits that can be derived from the intensity of the IGRB (short-dashed grey line) [31], at least below 100 GeV. Above this value, the IGRB intensity leads to an even more stringent exclusion.

[27] See Ref. [34] on how to compute the emission for multiple annihilation/decay channels without having to recompute, for each case, the mock sky maps from the N-body simulations.

In the right panel, it can be seen that the lower limits on τ derived here from the auto- and cross-APS are a factor of 5 less stringent than the lower limits obtained in Fig. 6 of Ref. [96] from the IGRB intenstity, in their conservative scenario. The REF scenario is also at least a factor of 5 from the dash-dotted grey line showing the lower limits obtained from the combined analysis of 15 dwarf spheroidal galaxies in Ref. [97].

Figs. 35 and 36 in Appendix E show the exclusion limits on $\langle\sigma_{\rm ann}v\rangle$ and τ in the case of the τ- and μ- channels.

B. Fit to the data and realistic exclusion limits

In this section we describe our analysis of the auto- and cross-APS using a 2-component model that includes a Poissonian term and a DM-induced one which, as we noticed in Fig. 24, deviates from a Poissonian behaviour. The Poissonian component is interpreted as the APS of unresolved astrophysical sources, even if we do not try to predict its amplitude in terms of a specific model. This 2-component model will be used to fit the *Fermi* LAT APS as a function of multipole.

The fit minimizes the χ^2 defined as:

$$\chi^2 = \sum_{i,j,\ell} \frac{[\overline{C_\ell}^{i,j} - C^{i,j}_{\ell,\rm DM} - C^{i,j}_{\rm P,astro}]^2}{[\overline{\sigma_\ell}^{i,j}]^2}, \tag{23}$$

where the i,j indexes in the sum extend over all the 91 independent combinations of energy bins and the ℓ index runs over the 10 bins in multipoles contained in the signal region. $\overline{C_\ell}^{i,j}$ indicates the APS measured in the (i,j) combination of energy bins and in the ℓ multipole bin, while $C^{i,j}_{\ell,\rm DM}$ and $C^{i,j}_{\rm P,astro}$ are the DM and Poissonian components of our model in the same combination of energy bins and in the same multipole bin. Finally, $\overline{\sigma_\ell}^{i,j}$ is the experimental error associated to $\overline{C_\ell}^{i,j}$ and provided by PolSpice. The DM APS $C^{i,j}_{\ell,\rm DM}$ are computed for the same 60 values of m_χ as in the previous section, the same 3 annihilation/decay channels, 3 benchmark scenarios and 3 values of $M_{\rm min}$. The only remaining parameter needed to calculate $C^{i,j}_{\ell,\rm DM}$ is either $\langle\sigma_{\rm ann}v\rangle$ or τ: they will be fixed to a specific value every time we compute χ^2. On the other hand, the 91 independent values of $C^{i,j}_{\rm P,astro}$ in Eq. 23 are left free in the fit. Putting the DM term to zero in Eq. 23 defines our null hypothesis. In that case, the fit to the *Fermi* LAT data leads us to the $C_{\rm P}$ estimators discussed in Sec. III, whose auto-APS is plotted in Fig. 8. Including the DM component, for a fixed m_χ, annihilation/decay channel, benchmark scenario and $M_{\rm min}$, we repeat the minimization of χ^2 in Eq. 23, for different values of $\langle\sigma_{\rm ann}v\rangle$ and τ.

We show an example in Fig. 26, for the case of the REF scenario for a DM candidate with a mass of 768.1 GeV, $\langle\sigma_{\rm ann}v\rangle = 6.12\times10^{-24}{\rm cm}^3{\rm s}^{-1}$ annihilating into $b\bar{b}$. The value of the annihilation cross section corresponds approximately to the exclusion upper limit for that value of DM mass, as will be computed later. The red circles show the measured auto-APS as a function of ℓ in the signal region for one reference energy bin, i.e., the one between 10.4 and 21.8 GeV (when masking 3FGL sources). The solid red line with the pink band denotes the best-fit $C_{\rm P}$ in that energy bin for the null hypothesis (i.e., without DM), while the dashed blue line is the best-fit Poissonian component $C_{\rm P,astro}$ when the fit is done with the 2-component model (i.e. including DM). The dashed line is lower than the solid one, since at these energies part of the signal is explained by DM and, therefore, there is less need of a Poissonian component. Energy bins not localized near the peak of the DM emission are only slightly affected by the inclusion of the DM term in the fit. The best-fit configuration for the two-components model is plotted by blue triangles: the inclusion of the DM term makes it multipole-dependent so that it decreases by a factor of $\sim$3 over the signal region.

We note that, including the DM component, it is possible to find a configuration that improves the χ^2 of the best-fit point with respect to the null hypothesis, at least for DM masses above few hundreds of GeV. This is probably due to the fact that the measured auto-APS is slightly multipole-dependent. We can quantify the improvement in the fit provided by the DM component by building a 2-dimensional grid in $(m_\chi, \langle\sigma_{\rm ann}v\rangle)$ for annihilating DM and in (m_χ,τ) for decaying DM and plotting the TS $\Delta\chi^2$, i.e. the difference between the χ^2 of the best fit for the null hypothesis and the χ^2 of the best fit in the case of the 2-component model. This is shown in Fig. 27, where the left panel refers to annihilating DM and the right one to decaying DM (for the b channel and a REF scenario with $M_{\rm min} = 10^{-6}M_\odot$). In both panels, the closed area indicate the region where the 2-component model is preferred over the null hypothesis at a 68% CL. The 90% and 95% CL regions are open and bounded by the corresponding white lines[28]. This tells us that including the DM component in the model provides a better fit to the auto- and cross-APS measured in Sec. III,

[28] The 68% CL ares is obtained by identifying the region where the best-fit solution for the 2-component model has a TS $\Delta\chi^2$ of 2.30 larger than the null hypothesis. The values are 4.61 and 5.99 for the 90% and 95% CL regions.

with a significance between 1 and 1.6σ. This is too small to consider as significant. Thus, we conclude that the data do not significantly prefer the addition of a DM component and we use the measured auto- and cross-APS to derive constraints on the DM signal.

The contour plots for the τ- and the μ-channel can be seen in Appendix E. In both cases, the 68% CL region is the only closed one.

For each value of m_χ, $M_{\rm min}$, annihilation/decay channel and benchmark scenario, the exclusion limits on $\langle\sigma_{\rm ann}v\rangle$ and τ are derived by scanning on $\langle\sigma_{\rm ann}v\rangle$ and τ until we find the values that correspond to a best fit with a TS $\Delta\chi^2$ of 3.84 with respect to the null hypothesis. Such a value is derived assuming that $\Delta\chi^2$ follows a χ^2 probability distribution with one degree of freedom (i.e., $\langle\sigma_{\rm ann}v\rangle$ or τ) and noting that values larger than 3.84 fall outside 5% of the cumulative distribution probability. This recipe provides the 95% CL exclusion limits on $\langle\sigma_{\rm ann}v\rangle$ and τ that are summarised in the left and right panels of Fig. 28, respectively.

In the left panel, as in Fig. 25, the black, blue and red solid lines correspond to the REF, MIN and MAX scenarios. The difference between MIN and MAX covers slightly more than a factor of 5. The blue and red shaded regions around the solid lines of the same color indicate how the upper limits change when we leave $M_{\rm min}$ free to vary. This extends the range of the total systematic uncertainty to approximately a factor of 20. For comparison, the black dashed line is the REF upper limit in its conservative version (from Fig. 25). Fitting the data with the 2-component model generates exclusion limits that are approximately a factor of 10 stronger, at least at low DM masses. As the mass increases, the method employed in this section starts to perform progressively worse and the solid black line gets closer to the dashed one. This is due to the fact that, for $m_\chi > 150$ GeV, the data slightly prefer the interpretation with DM as opposed to the null hypothesis. The figure also includes the thermal cross section from Ref. [94] as a long-dashed grey line: our upper limit for the REF case is slightly above it, below 10 GeV. It is also more than a factor 10 weaker than the upper limit derived from the observation of 15 dwarf spheroidal galaxies in Ref. [95]. Finally, the short-dashed grey line indicates the exclusion limits obtained in Ref. [98] by studying the intensity of the IGRB with a 2-component model that, similarly to what is done here, includes both a generic model-independent astrophysical contribution and a DM one. Our REF limit is slightly stronger than the short-dashed grey line for $m_\chi < 30$ GeV, suggesting that the study of the IGRB anisotropies could *in principle* be a more effective way of constraining DM than the IGRB intensity. However, for larger DM masses, our limit gets worse due, again, to the fact that the data slightly prefer an interpretation that includes DM.

The same color coding is used in the right panel for decaying DM. With no dependence on $M_{\rm min}$, the band of the systematic uncertainty covers a factor 2, and the REF upper limit is even one order of magnitude above the conservative one, at least at 60-70 GeV. For larger masses our limit worsens for the same reason as in the left panel. As in Fig. 25, the short-dashed grey line is the lower limit obtained from the analysis of the IGRB intensity from Ref. [96]. The line refers to the case in which the IGRB is modeled in terms of a component with a power-law energy spectrum and a DM contribution. Above 20 GeV, where both lines are available, the analysis of the IGRB intensity is always more powerful than the anisotropy study performed here. Finally, the dot-dashed grey line is the lower limit obtained from the analysis of 15 dwarf spheroidal galaxies in Ref. [97]. Our REF scenario is always below this line, at least by a factor of 2.

In Appendix E we include the exclusion limits for the τ- and μ-channels.

When fitting with the 2-component model, the 91 $C^{i,j}_{\rm P,astro}$ can vary independently and they react to the presence of the DM component by reproducing the measured APS in those combinations of energy bins where the DM component is subdominant. Therefore, it may difficult to interpret a best-fit set of $C^{i,j}_{\rm P,astro}$ in terms of one or more populations of actual astrophysical sources, e.g. unresolved blazars or star-forming galaxies. A more physical approach can be obtained by considering the phenomenological description presented in Sec. VI. In this case, the astrophysical component in the 2-component fit is described by means of the two-broken-power-law scenario (see Tab. III). The latter depends on 8 free parameters instead of 91. We employ this revised version of the 2-component model to fit the binned auto- and cross-APS $\overline{C_\ell}$ in all the combinations of energy bins. The exclusion limits on $\langle\sigma_{\rm ann}v\rangle$ and τ are obtained by finding the configuration that yields a χ^2 that is larger by 3.84 than the best-fit χ^2 of the null hypothesis (i.e. no DM). The resulting upper limits are compatible with the ones showed in Fig. 28 and, therefore, we decided not to show them.

IX. DISCUSSION AND CONCLUSION

In this paper we measure the auto-correlation and cross-correlation angular power spectrum (APS) of the diffuse gamma-ray emission detected by *Fermi* LAT at high Galactic latitudes in 81 months of observation. The measurement builds on a similar analysis based on 22 months of data and published in Ref. [1]. With respect to the latter, this work takes advantage of the larger statistics, as well as of the improved event reconstruction achieved for Pass 7 Reprocessed events and instrument response functions. Other improvements, with respect to Ref. [1], consist of a

revised method for binning the data in multipole and to compute the Poissonian auto- and cross-APS. We also correct the estimate of the photon noise and we employ a different method to account for the effect of the mask. Finally, we consider a more recent model of the diffuse Galactic foreground associated with the Milky Way (MW) disk.

The second part of the paper focuses on the auto- and cross-APS expected from annihilation or decay of DM. We employ a hybrid approach to model the distribution of DM, making use of catalogs of DM halos and subhalos from state-of-the-art N-body simulations and combining them with analytical recipes to account for DM structures below the mass resolution of the simulations. The methodology follows what was done in Ref. [34]. Compared to the latter, this work discards the possibility of very large subhalo boost factors induced by naïve power-law extrapolations of the concentration parameter to low halo masses. We also account for the uncertainty associated with the mass of the MW, and we correct for the possibility of having very bright Galactic DM subhalos that would be individually resolved as gamma-ray sources.

The main results of this papers are summarized in the following list.

- *Detection of auto- and cross-APS:* because of the instrumental improvements and of the refinements in the analysis mentioned before, the measurement presented here probes a larger energy range (compared to the original analysis in Ref. [1]), between 0.5 and 500 GeV, divided in 13 energy bins. We also compute, for the first time, the cross-APS between different energy bins. We detect significant auto-APS in almost all the energy bins below 21.83 GeV. Significant cross-APS is also measured in most combinations of energy bins (see Tabs. I and II).

- *Independence on angular multipole:* our results cover a larger range in multipoles than the original analysis, i.e., from $\ell = 49$ and 706. In this multipole range, the detected auto- and cross-APS are consistent with being Poissonian, i.e. constant in multipole. An alternative ℓ-dependent model is also employed to fit the data but there is no significant preference for the ℓ-dependent model over the Poissonian interpretation. If future data sets were able to detect a non-Poissonian behaviour, it would represent the first detection of scale dependence in gamma-ray anisotropies. Such a result would provide valuable insight into the nature of the Isotropic Gamma-Ray Background (IGRB), e.g. an upper limit on the contribution of sources like blazars or misaligned active galactic nuclei, which are associated with a Poissonian APS. It would also probe other possible sources like star-forming galaxies or Dark Matter (DM) structures, from which we expect a ℓ-dependent auto- and cross-APS [8].

- *Detection of multiple source classes:* the anisotropy energy spectrum (i.e. the dependence of the auto- and cross-APS on the energy) is not featureless and it is best fitted by two populations of sources with broken-power-law energy spectra. The interpretation in terms of only one source population (whether emitting as a power law or broken power law) is excluded at 95% CL. This suggests that the auto- and cross-APS result from a class of objects emitting mainly at low energies with a soft energy spectrum $\propto E^{-\alpha_1}$ with $\alpha_1 \sim 2.58$, and a second population of harder objects with $\alpha_2 \sim 2.10$. The cross-over between the two source classes, according to our fit, happens at approximately 2 GeV. The harder spectral slope is compatible with that expected from BL Lacertae [38], which are thought to dominate the IGRB at high energies. At lower energies, the spectral slope is similar to that of Flat-Spectrum Radio Quasars [99] or of normal star-forming galaxies [8, 100] (see also Ref. [101]).

- *Presence of an high-energy cut-off:* our best-fit interpretation shows a cut-off at around 85 GeV. This may be related to the absorption of the extragalactic background light (EBL), since a similar feature is detected in the intensity energy spectrum of the IGRB in Ref. [4][29]. If we were able to confirm that the cut-off is associated with the EBL, this would be the first time that the absorption by the EBL is detected via anisotropies. One way to achieve such a confirmation would be to detect a significant cross-correlation between the same data set employed here and a catalog of tracers of the Large-Scale Structure of the Universe. The possibility of binning the catalog in redshift would allow us to perform a tomographic analysis and to select the emission coming from different comoving distances [21, 22]. Alternatively, the cut-off may be an intrinsic feature of the energy spectrum of the sources responsible for the auto- and cross-APS at high energies.

- *Systematic uncertainties in the anisotropies induced by annihilating DM:* in the case of an annihilating DM candidate, an uncertainty of a factor 4 in the mass of the MW induces a variation of a factor $\sim$30 in the auto- and cross-APS associated with Galactic subhalos. For a MW mass of the order of $10^{12} M_\odot$, Galactic subhalos dominate the expected anisotropic signal from DM. If the MW is less massive, i.e., few times $10^{11} M_\odot$, the

[29] The cut-off in the IGRB energy spectrum detected in Ref. [4] is at slightly higher energies, namely around 200 GeV, depending on the model of the diffuse Galactic foreground employed. Notice, however, that the measurement in Ref. [4] is performed masking the sources in the 2FGL, while the value of E_b=85 GeV quoted above refers to the measurement after masking the sources in the 3FGL. Thus, it is possible for the two cut-offs to be located at different energies.

extragalactic component starts to be important, at least for large subhalo boost models. For DM annihilations occuring in extragalactic DM halos and subhalos, the uncertainties on the subhalo boost factor (for a fixed $M_{\rm min}$) induce an uncertainty of a factor $\sim$20 on the expected auto- and cross-APS from this component. The gamma-ray emission produced by DM annihilations in the smooth halo of the MW generates a negligible anisotropic signal outside the adopted mask. The overall uncertainty on the predicted DM-induced APS (for a fixed $M_{\rm min}$) is of a factor of 20, similar to the one estimated in Ref. [31] for the intensity of all-sky gamma-ray emission. Changing the value of $M_{\rm min}$ from 10^{-12} to 1 $M_\odot$ approximately doubles the systematic uncertainty.

- *Systematic uncertainties in the anisotropies induced by decaying DM:* In the case of decaying DM, the extragalactic signal dominates the expected auto- and cross-APS and the prediction is independent of the value of the subhalo boost factor. Decays in the smooth halo of the MW or in its subhalos are subdominant. The overall uncertainty (for a fixed value of $M_{\rm min}$) is less than a factor of 2. Varying $M_{\rm min}$ over the range mentioned before has a negligible effect in the case of decaying DM.

- *Conservative exclusion limits on DM:* requiring that the DM-induced auto- and cross-APS does not exceed the measurement in any energy bin or combination of energy bins yields an upper limit on $\langle\sigma_{\rm ann}v\rangle$ that is at least a factor of 2 less stringent that the one obtained in Ref. [31] from the analysis of the IGRB energy spectrum (for the REF scenario and the b channel). In the case of annihilations into $b\bar{b}$, the constraint on the annihilation cross section reaches a value as low as $10^{-25}{\rm cm}^3{\rm s}^{-1}$ for a DM mass of 5 GeV and, therefore, it is approximately two orders of magnitude less constraining than the one inferred from the observation of dwarf spheroidals galaxies. For decaying DM, the lower limit on τ is a factor of 5 weaker than the one from the IGRB intensity [96] and, at least, a factor of 5 weaker than the one from the analysis of dwarf spheroidal galaxies [97] (for the REF case and decays into $b\bar{b}$).

- *Exclusion limits from the 2-component fit:* fitting the data with a 2-component model that includes DM provides more constraining exclusion limits. The resulting upper limit for annihilating DM (in the REF scenario for a $M_{\rm min}$ of $10^{-6}M_\odot/h$ and annihilations into $b\bar{b}$) is still a factor of 10 less constraining than the combined analysis of dwarf spheroidals from Ref. [95]. However, below a DM mass of 30 GeV, it is slightly better than what was derived in Ref. [98] from the analysis of the IGRB intensity energy spectrum in terms of a 2-component model. For decaying DM, the lower limits on τ are, at least, a factor of 2 less stringent than those obtained from the IGRB intensity energy spectrum [96] or from the combined analysis of dwarf spheroidals [97].

The exclusion limits on DM, although they do not exclude new regions of the DM parameter space, are complementary to those computed from the intensity of the IGRB or from the observation of dwarf spheroidals and, therefore, they provide independent information. Also, they are expected to become more stringent as the measurement of the auto- and cross-APS will improve during the next years. Beside making use of the data collected after May 2015, future analyses will rely on Pass 8 data, benefiting from the new event classes and data selections available (see Sec. V C). Also, future catalogs of sources, deeper than 3FGL, will explore faint sources that are now unresolved and will improve our modelling of those source classes. It will certainly be interesting to complement the measurement of gamma-ray anisotropies performed here with a similar observation at higher energies (which will be possible in the near future with the Cherenkov Telescope Array [102, 103]) or in the sub-GeV regime (with future satellites like ASTROGAM[30] and ComPair [104]). Finally, in a multi-messenger perspective, the study of gamma-ray anisotropies can be interfaced with similar analyses on the high-energy neutrinos recently discovered by IceCube [105–108]. Since the same sources that contribute to the IGRB (e.g. blazars, star-forming or radio galaxies) are expected to emit also neutrinos, the auto- and cross-APS measured in this work represents a useful indication for the *minimal* level of anisotropies that can be found in the distribution of neutrinos. A quantitative estimate of IceCube prospects to detect anisotropies can be found in Ref. [109].

ACKNOWLEDGMENTS

The *Fermi* LAT Collaboration acknowledges generous ongoing support from a number of agencies and institutes that have supported both the development and the operation of the LAT as well as scientific data analysis. These include the National Aeronautics and Space Administration and the Department of Energy in the United States, the Commissariat à l'Energie Atomique and the Centre National de la Recherche Scientifique / Institut National de Physique Nucléaire et de Physique des Particules in France, the Agenzia Spaziale Italiana and the Istituto Nazionale di

[30] http://astrogam.iaps.inaf.it/

Fisica Nucleare in Italy, the Ministry of Education, Culture, Sports, Science and Technology (MEXT), High Energy Accelerator Research Organization (KEK) and Japan Aerospace Exploration Agency (JAXA) in Japan, and the K. A. Wallenberg Foundation, the Swedish Research Council and the Swedish National Space Board in Sweden.

Additional support for science analysis during the operations phase is gratefully acknowledged from the Istituto Nazionale di Astrofisica in Italy and the Centre National d'Études Spatiales in France.

We thank Dr. Shin'ichiro Ando for useful discussion and for providing us with the lower limits on the decay lifetime from Ref. [96]. We also thanks Prof. John F. Beacom for the valuable discussion during the last stages of the work.

MF gratefully acknowledges support from the Netherlands Organization for Scientific Research (NWO) through a Vidi grant (P.I.: Dr. Shin'ichiro Ando), from the the Leverhulme Trust and the project MultiDark CSD2009-00064. The Dark Cosmology Centre is funded by the DNRF. JZ is supported by the EU under a Marie Curie International Incoming Fellowship, contract PIIF-GA-2013-62772. JG acknowledges support from NASA through Einstein Postdoctoral Fellowship grant PF1-120089 awarded by the Chandra X-ray Center, which is operated by the Smithsonian Astrophysical Observatory for NASA under contract NAS8-03060, and from a Marie Curie International Incoming Fellowship, contract PIIF-GA-2013-628997. GAGV is supported by CONICYT FONDECYT/POSTODOCTORADO/3160153, the Spanish MINECO's Consolider Ingenio 2010 Programme under grant MultiDark CSD2009-00064 and also partly by MINECO under grant FPA2012-34694. MASC is a Wenner-Gren Fellow and acknowldeges the support of the Wenner-Gren Foundantions to develop his research. EK thanks J.U. Lange for useful discussion on the bias in $C_{\rm P}$ due to binning presented in Sec. IV A. FP acknowledges support from the Spanish MICINNs Consolider-Ingenio 2010 Programme under grant MultiDark CSD2009-00064, MINECO Centro de Excelencia Severo Ochoa Programme under grant SEV-2012-0249 and MINECO grant AYA2014-60641-C2-1-P. FZ acknowledges the support of the NWO through a Veni grant.

Appendix A: Derivation of the photon noise $C_{\rm N}$

Let n_i be the number of photons in a pixel i, $\bar{n}_i$ be its expectation value, and $\delta n_i \equiv n_i - \bar{n}_i$ be a fluctuation around the mean. The photon flux is given by n_i/A_i, where A_i is the exposure in pixel i. Then, the photon flux per unit solid angle is given by $n_i/(A_i\Omega_{\rm pix})$ where $\Omega_{\rm pix}$ is the solid angle of pixel i.

The spherical harmonics coefficients $a_{\ell,m}$ are

$$a_{\ell,m} = \int d\Omega_i \, \frac{\delta n_i}{A_i \Omega_{\rm pix}} Y^*_{\ell,m}(\Omega_i) \,, \tag{A1}$$

where Ω_i denotes the direction of pixel i. The expectation value of the product between two coefficients is

$$\langle a_{\ell,m} a^*_{\ell',m'} \rangle = \int d\Omega_i \int d\Omega_j \, \frac{\langle \delta n_i \delta n_j \rangle}{A_i A_j \Omega^2_{\rm pix}} \, Y^*_{\ell m}(\Omega_i) Y_{\ell' m'}(\Omega_j) \,. \tag{A2}$$

If δn_i is purely Poisson noise, $\langle \delta n_i \delta n_j \rangle / \Omega^2_{\rm pix} = (\bar{n}_i/\Omega_{\rm pix}) \, \delta(\Omega_i - \Omega_j)$ where δ is the Dirac delta function. Thus:

$$\langle a_{\ell,m} a^*_{\ell',m'} \rangle = \int d\Omega_i \, \frac{\bar{n}_i}{A_i^2 \Omega_{\rm pix}} \, Y_{\ell m}(\Omega_i) Y^*_{\ell' m'}(\Omega_i) \,. \tag{A3}$$

Now, we calculate the diagonal element, i.e., $C_\ell \equiv \sum_m \langle a_{\ell,m} a^*_{\ell,m} \rangle / (2\ell+1)$, obtaining:

$$C_\ell = \int \frac{d\Omega_i}{4\pi} \, \frac{\bar{n}_i}{A_i^2 \Omega_{\rm pix}} \,. \tag{A4}$$

The latter is independent on multipole ℓ and equivalent to the definition of $C^k_{\rm N}$ in Eq. 5.

Appendix B: Auto-correlation angular spectra for all the energy bins

Figs. 29 and 30 show the binned auto-APS $\overline{C_\ell}$ obtained as described in Sec. III, for all 13 energy bins considered. The auto-APS is shown only within the signal region, i.e. between a multipole of 49 and 706. Red circles refer to the data set obtained with our default mask covering the sources in 3FGL and the solid red line marks the corresponding best-fit $C_{\rm P}$. The pink band denotes the 68% CL error on $C_{\rm P}$. The blue data points are for the same data set but using the default mask covering sources in 2FGL. The dashed blue line stands for the Poissonian best-fit to the blue triangles. Data are available at https://www-glast.stanford.edu/pub_data/552.

Appendix C: Anisotropy energy spectrum for the cross-correlation angular power spectrum

Figs. 31 and 32 show the best-fit $C_{\rm P}$ for the cross-APS as a function of energy. Red circles refer to the mask covering 3FGL sources and blue triangles to the mask of 2FGL sources. The solid black line denotes the best-fit solution discussed in Sec. VI, i.e., the one in terms of two populations of unresolved sources with broken-power-law energy spectra. The short-dashed and long-dashed black lines indicate the two source populations independently. Data are available at https://www-glast.stanford.edu/pub_data/552.

Appendix D: The dependence on energy of the cross-correlation coefficients

Figs. 33 and 34 show the cross-correlation coefficients $r_{i,j}$ defined in Sec. V B in terms of the best-fit auto- and cross-APS $C_{\rm P}$. Each panel shows $r_{i,j}$ at a specific energy E_i, as a function of E_j. Red circles refer to the mask covering 3FGL sources and blue triangles to the mask around 2FGL sources. The solid black line shows the cross-correlation coefficents corresponding to the best-fit solution discussed in Sec. VI in the case of two populations of unresolved sources with broken-power-law energy spectra and masking 3FGL sources. The fact that the blue triangles decrease with energy in the first panels, while they increase towards 1 in the last panels indicates the lack of correlation between low and high energies. The same trend is noted for the red circles, but with a lower significance.

Appendix E: Exclusion limit on Dark Matter for the τ and μ channel

Sec. VIII shows exclusion limits on the DM $\langle\sigma_{\rm ann}v\rangle$ and τ in the case of annihilations/decay into $b\bar{b}$. Here we calculate the same exclusion limits for two additional channels. Fig. 35 shows the upper limits on $\langle\sigma_{\rm ann}v\rangle$ (left panel) and on τ (right panel) as a function of the DM mass m_χ, in the case of annihilations/decays into $\tau^+\tau^-$. The exclusion limits are obtained following the conservative approach described in Sec. VIII A. The solid black line refers to the REF scenario, while the solid red and solid blue ones stand for the MAX and MIN benchmark. The solid red and solid black lines almost exactly overlap in the right panel. The dashed black, blue and red lines are obtained considering only the auto-APS measurement. The red and blue shaded band indicate the variability of the exclusion limits in the MAX and MIN scenario when $M_{\rm min}$ is left free to vary between 1 $M_\odot$ and $10^{-12}M_\odot$. The long-dashed grey line in the left panel shows the thermal annihilation cross section, as computed in Ref. [94], while the dot-dashed grey line is the upper limit obtained in Ref. [95] from the analysis of 15 dwarf spheroidal galaxies. Finally, the short-dashed grey line derives from the analysis of the IGRB intensity performed in Ref. [31]. On the other hand, the short-dashed grey line in the right panel of Fig. 35 is obtained from the study of the IGRB intensity in Ref. [96] and the dot-dashed grey line comes from the observation of 15 dwarf spheroidal galaxies performed in Ref. [97].

Fig. 36 shows the same exclusion limits as in Fig 35 but for annihilations/decays into the $\mu^+\mu^-$. Between approximately 20 and 200 GeV, the DM-induced signal is dominated by the IC emission associated with the smooth halo of the MW. That is the reason why the solid black and red lines overlap, since the REF and MAX scenarios only differ in the computation of the boost factor for the extragalactic component. For the same reason the blue and red shaded bands are reduced in width. Above 200 GeV, the IC emission for the extragalactic component starts to contribute more and the solid black and red lines deviate one from the other again.

The 2-component model developed in Sec.VIII B is used to fit the measured auto-APS and cross-APS, for different values of DM mass, annihilation cross section or decay lifetime. Fig. 37 shows the TS defined as the difference between the χ^2 of the best fit for the null hypothesis (i.e. with no DM) and the χ^2 of the best fit in the case with the DM component. The top panels are for annihilation/decay into $\tau^+\tau^-$ and the bottom ones for the μ-channel. The ones on the right are for an annihilating DM candidate and the ones on the left for decaying DM. They all refer to the REF scenario with $M_{\rm min} = 10^{-6}M_\odot/h$. As indicated in the labels, the white lines determine the 68%, 90% and 95% CL regions.

Assuming that the measured auto- and cross-APS are well described simply by a Poissonian component, the 2-component model is used to derive exclusion limits on DM as done in Sec. VIII B but in the case of annihilations/decays into $\tau^+\tau^-$ (Fig. 38) and into $\mu^+\mu^-$ (Fig. 39). In both figures the left panel is for annihilating DM and the right one for decaying DM. The solid black, red and blue line show the REF, MAX and MIN scenario for $M_{\rm min} = 10^{-6}M_\odot/h$, respectively and the blue and shaded areas around the corresponding solid lines indicate how the limits change when $M_{\rm min}$ is left free to vary. The dashed black is the exclusion limit in the conservative scenario, from Fig. 35 and 36. In the left panels, the long-dashed grey line is the thermal annihilation cross section from Ref. [94] and the dot-dashed line is the upper limit derived in Ref. [95] from the combined analysis of 15 dwarf spheroidals. Also, the short-dashed grey line comes from the analysis of the IGRB intensity performed in Ref. [98]. On the other hand, in the right panels,

the short-dashed grey line represents the lower limit from Fig. 5 of Ref. [96] from the IGRB intensity. The dot-dashed grey line is the lower limit from the analysis of 15 dwarf spheroidal galaxies performed in Ref. [97].

[1] M. Ackermann *et al.* (Fermi-LAT), Phys. Rev. **D85**, 083007 (2012), arXiv:1202.2856 [astro-ph.HE].
[2] A. A. Abdo *et al.* (Fermi-LAT), Astrophys. J. Suppl. **188**, 405 (2010), arXiv:1002.2280 [astro-ph.HE].
[3] A. A. Abdo *et al.* (Fermi-LAT), Phys. Rev. Lett. **104**, 101101 (2010), arXiv:1002.3603 [astro-ph.HE].
[4] M. Ackermann *et al.* (Fermi-LAT), Astrophys. J. **799**, 86 (2015), arXiv:1410.3696 [astro-ph.HE].
[5] M. Fornasa and M. A. Snchez-Conde, Phys. Rept. **598**, 1 (2015), arXiv:1502.02866 [astro-ph.CO].
[6] P.-J. Zhang and J. F. Beacom, Astrophys. J. **614**, 37 (2004), arXiv:astro-ph/0401351 [astro-ph].
[7] S. Ando, E. Komatsu, T. Narumoto, and T. Totani, Mon.Not.Roy.Astron.Soc. **376**, 1635 (2007), arXiv:astro-ph/0610155 [astro-ph].
[8] S. Ando and V. Pavlidou, Mon. Not. Roy. Astron. Soc. **400**, 2122 (2009), arXiv:0908.3890 [astro-ph.HE].
[9] J. M. Siegal-Gaskins, R. Reesman, V. Pavlidou, S. Profumo, and T. P. Walker, Mon.Not.Roy.Astron.Soc. **415**, 1074S (2011), arXiv:1011.5501 [astro-ph.HE].
[10] A. Cuoco, E. Komatsu, and J. M. Siegal-Gaskins, Phys. Rev. **D86**, 063004 (2012), arXiv:1202.5309 [astro-ph.CO].
[11] J. P. Harding and K. N. Abazajian, JCAP **1211**, 026 (2012), arXiv:1206.4734 [astro-ph.HE].
[12] M. Di Mauro, F. Calore, F. Donato, M. Ajello, and L. Latronico, Astrophys. J. **780**, 161 (2014), arXiv:1304.0908 [astro-ph.HE].
[13] F. Zandanel, I. Tamborra, S. Gabici, and S. Ando, Astron. Astrophys. **578**, A32 (2015), arXiv:1410.8697 [astro-ph.HE].
[14] S. Ando and E. Komatsu, Phys. Rev. **D87**, 123539 (2013), arXiv:1301.5901 [astro-ph.CO].
[15] D. Hooper, T. Linden, and A. Lopez, JCAP **1608**, 019 (2016), arXiv:1604.08505 [astro-ph.HE].
[16] M. Di Mauro, A. Cuoco, F. Donato, and J. M. Siegal-Gaskins, JCAP **1411**, 021 (2014), arXiv:1407.3275 [astro-ph.HE].
[17] J.-Q. Xia, A. Cuoco, E. Branchini, and M. Viel, Astrophys. J. Suppl. **217**, 15 (2015), arXiv:1503.05918 [astro-ph.CO].
[18] M. Shirasaki, S. Horiuchi, and N. Yoshida, Phys. Rev. **D92**, 123540 (2015), arXiv:1511.07092 [astro-ph.CO].
[19] A. Cuoco, J.-Q. Xia, M. Regis, E. Branchini, N. Fornengo, and M. Viel, Astrophys. J. Suppl. **221**, 29 (2015), arXiv:1506.01030 [astro-ph.HE].
[20] M. Regis, J.-Q. Xia, A. Cuoco, E. Branchini, N. Fornengo, and M. Viel, Phys. Rev. Lett. **114**, 241301 (2015), arXiv:1503.05922 [astro-ph.CO].
[21] S. Ando, A. Benoit-Lvy, and E. Komatsu, Phys. Rev. **D90**, 023514 (2014), arXiv:1312.4403 [astro-ph.CO].
[22] S. Ando, JCAP **1410**, 061 (2014), arXiv:1407.8502 [astro-ph.CO].
[23] M. Shirasaki, S. Horiuchi, and N. Yoshida, Phys. Rev. **D90**, 063502 (2014), arXiv:1404.5503 [astro-ph.CO].
[24] N. Fornengo, L. Perotto, M. Regis, and S. Camera, Astrophys. J. **802**, L1 (2015), arXiv:1410.4997 [astro-ph.CO].
[25] D. Malyshev and D. W. Hogg, Astrophys. J. **738**, 181 (2011), arXiv:1104.0010 [astro-ph.CO].
[26] H.-S. Zechlin, A. Cuoco, F. Donato, N. Fornengo, and A. Vittino, Astrophys. J. Suppl. **225**, 18 (2016), arXiv:1512.07190 [astro-ph.HE].
[27] H.-S. Zechlin, A. Cuoco, F. Donato, N. Fornengo, and M. Regis, Astrophys. J. **826**, L31 (2016), arXiv:1605.04256 [astro-ph.HE].
[28] J. M. Siegal-Gaskins and V. Pavlidou, Phys. Rev. Lett. **102**, 241301 (2009), arXiv:0901.3776 [astro-ph.HE].
[29] J. Zavala, V. Springel, and M. Boylan-Kolchin, Mon. Not. Roy. Astron. Soc. **405**, 593 (2010), arXiv:0908.2428 [astro-ph.CO].
[30] A. Cuoco, A. Sellerholm, J. Conrad, and S. Hannestad, Mon. Not. Roy. Astron. Soc. **414**, 2040 (2011), arXiv:1005.0843 [astro-ph.HE].
[31] M. Ackermann *et al.* (Fermi-LAT), JCAP **1509**, 008 (2015), arXiv:1501.05464 [astro-ph.CO].
[32] G. A. Gomez-Vargas, A. Cuoco, T. Linden, M. A. Sanchez-Conde, J. M. Siegal-Gaskins, T. Delahaye, M. Fornasa, E. Komatsu, F. Prada, and J. Zavala (Fermi-LAT), *Proceedings, 4th Roma International Conference on Astro-Particle Physics (RICAP 13)*, Nucl. Instrum. Meth. **A742**, 149 (2014).
[33] J. U. Lange and M. C. Chu, Mon. Not. Roy. Astron. Soc. **447**, 939 (2015), arXiv:1412.5749 [astro-ph.CO].
[34] M. Fornasa, J. Zavala, M. A. Sanchez-Conde, J. M. Siegal-Gaskins, T. Delahaye, F. Prada, M. Vogelsberger, F. Zandanel, and C. S. Frenk, Mon. Not. Roy. Astron. Soc. **429**, 1529 (2013), arXiv:1207.0502 [astro-ph.HE].
[35] K. M. Gorski, E. Hivon, A. J. Banday, B. D. Wandelt, F. K. Hansen, M. Reinecke, and M. Bartelman, Astrophys. J. **622**, 759 (2005), arXiv:astro-ph/0409513 [astro-ph].
[36] M. Ackermann, G. Johannesson, S. Digel, I. V. Moskalenko, T. Porter, O. Reimer, and A. Strong (Fermi-LAT), *4th Heidelberg International Symposium on High-Energy Gamma Ray Astronomy Heidelberg, Germany, July 7-11, 2008*, AIP Conf. Proc. **1085**, 763 (2009).
[37] A. Challinor, G. Chon, S. Colombi, H. Eric, S. Prunet, and I. Szaput, *PolSpice: Spatially Inhomogeneous Correlation Estimator for Temperature and Polarisation* (Astrophysics Source Code Library, 2011).
[38] F. Acero, Astrophys. J. Suppl. **218**, 23 (2015).
[39] P. L. Nolan *et al.* (Fermi-LAT), Astrophys. J. Suppl. **199**, 31 (2012), arXiv:1108.1435 [astro-ph.HE].
[40] F. Acero *et al.* (Fermi-LAT), Astrophys. J. Suppl. **223**, 26 (2016), arXiv:1602.07246 [astro-ph.HE].
[41] L. Knox, Phys. Rev. **D52**, 4307 (1995), arXiv:astro-ph/9504054 [astro-ph].
[42] S. S. Campbell, Mon. Not. Roy. Astron. Soc. **448**, 2854 (2015), arXiv:1411.4031 [astro-ph.CO].
[43] B. S. Hensley, J. M. Siegal-Gaskins, and V. Pavlidou, Astrophys. J. **723**, 277 (2010), arXiv:0912.1854 [astro-ph.CO].
[44] B. S. Hensley, V. Pavlidou, and J. M. Siegal-Gaskins, Mon. Not. Roy. Astron. Soc. **433**, 591 (2013), arXiv:1210.7239 [astro-ph.CO].

[45] S. Ando and E. Komatsu, Phys. Rev. **D73**, 023521 (2006), arXiv:astro-ph/0512217 [astro-ph].
[46] N. Fornengo and M. Regis, Front. Physics **2**, 6 (2014), arXiv:1312.4835 [astro-ph.CO].
[47] W. Atwood *et al.* (Fermi-LAT) (2013) arXiv:1303.3514 [astro-ph.IM].
[48] A. A. Abdo *et al.* (Fermi-LAT), Astrophys. J. **734**, 116 (2011), arXiv:1104.2093 [astro-ph.HE].
[49] K. C. Y. Ng, J. F. Beacom, A. H. G. Peter, and C. Rott, Phys. Rev. **D94**, 023004 (2016), arXiv:1508.06276 [astro-ph.HE].
[50] D. Seckel, T. Stanev, and T. K. Gaisser, Astrophys. J. **382**, 652 (1991).
[51] E. Orlando and A. Strong, *The Multi-Messenger Approach to High-Energy Gamma-Ray Sources*, Astrophys. Space Sci. **309**, 359 (2007), arXiv:astro-ph/0607563 [astro-ph].
[52] I. V. Moskalenko, T. A. Porter, and S. W. Digel, Astrophys. J. **652**, L65 (2006), [Erratum: Astrophys. J.664,L143(2007)], arXiv:astro-ph/0607521 [astro-ph].
[53] E. Orlando and A. Strong, (2013), arXiv:1307.6798 [astro-ph.HE].
[54] M. Ackermann *et al.* (Fermi-LAT), Phys. Rev. **D93**, 082001 (2016), arXiv:1604.03349 [astro-ph.HE].
[55] A. E. Broderick, C. Pfrommer, E. Puchwein, K. M. Smith, and P. Chang (Heidelberg Institute for Theoretical Studies, Perimeter Institute for Theoretical Physics), Astrophys. J. **796**, 12 (2014), arXiv:1308.0015 [astro-ph.CO].
[56] F. Feroz and M. P. Hobson, Mon. Not. Roy. Astron. Soc. **384**, 449 (2008), arXiv:0704.3704 [astro-ph].
[57] F. Feroz, M. P. Hobson, and M. Bridges, Mon. Not. Roy. Astron. Soc. **398**, 1601 (2009), arXiv:0809.3437 [astro-ph].
[58] F. Feroz, M. P. Hobson, E. Cameron, and A. N. Pettitt, (2013), arXiv:1306.2144 [astro-ph.IM].
[59] R. Trotta, Contemp. Phys. **49**, 71 (2008), arXiv:0803.4089 [astro-ph].
[60] M. Boylan-Kolchin, V. Springel, S. D. M. White, A. Jenkins, and G. Lemson, Mon. Not. Roy. Astron. Soc. **398**, 1150 (2009), arXiv:0903.3041 [astro-ph.CO].
[61] J. F. Navarro, A. Ludlow, V. Springel, J. Wang, M. Vogelsberger, S. D. M. White, A. Jenkins, C. S. Frenk, and A. Helmi, Mon. Not. Roy. Astron. Soc. **402**, 21 (2010), arXiv:0810.1522 [astro-ph].
[62] V. Springel, J. Wang, M. Vogelsberger, A. Ludlow, A. Jenkins, A. Helmi, J. F. Navarro, C. S. Frenk, and S. D. M. White, Mon. Not. Roy. Astron. Soc. **391**, 1685 (2008), arXiv:0809.0898 [astro-ph].
[63] S. Profumo and T. E. Jeltema, JCAP **0907**, 020 (2009), arXiv:0906.0001 [astro-ph.CO].
[64] A. Dominguez *et al.*, Mon. Not. Roy. Astron. Soc. **410**, 2556 (2011), arXiv:1007.1459 [astro-ph.CO].
[65] J. F. Navarro, C. S. Frenk, and S. D. M. White, Astrophys. J. **490**, 493 (1997), arXiv:astro-ph/9611107 [astro-ph].
[66] B. Moore, T. R. Quinn, F. Governato, J. Stadel, and G. Lake, Mon. Not. Roy. Astron. Soc. **310**, 1147 (1999), arXiv:astro-ph/9903164 [astro-ph].
[67] A. Burkert, *IAU Symposium 171: New Light on Galaxy Evolution Heidelberg, Germany, June 26-30, 1995*, IAU Symp. **171**, 175 (1996), [Astrophys. J.447,L25(1995)], arXiv:astro-ph/9504041 [astro-ph].
[68] P. A. R. Ade *et al.* (Planck), (2015), arXiv:1502.01589 [astro-ph.CO].
[69] Q. Guo, S. White, R. E. Angulo, B. Henriques, G. Lemson, M. Boylan-Kolchin, P. Thomas, and C. Short, Mon. Not. Roy. Astron. Soc. **428**, 1351 (2013), arXiv:1206.0052 [astro-ph.CO].
[70] A. D. Ludlow, J. F. Navarro, R. E. Angulo, M. Boylan-Kolchin, V. Springel, C. Frenk, and S. D. M. White, Mon. Not. Roy. Astron. Soc. **441**, 378 (2014), arXiv:1312.0945 [astro-ph.CO].
[71] M. Cirelli, G. Corcella, A. Hektor, G. Hutsi, M. Kadastik, P. Panci, M. Raidal, F. Sala, and A. Strumia, JCAP **1103**, 051 (2011), [Erratum: JCAP1210,E01(2012)], arXiv:1012.4515 [hep-ph].
[72] S. Profumo, K. Sigurdson, and M. Kamionkowski, Phys. Rev. Lett. **97**, 031301 (2006), arXiv:astro-ph/0603373 [astro-ph].
[73] T. Bringmann, New J. Phys. **11**, 105027 (2009), arXiv:0903.0189 [astro-ph.CO].
[74] M. A. Snchez-Conde and F. Prada, Mon. Not. Roy. Astron. Soc. **442**, 2271 (2014), arXiv:1312.1729 [astro-ph.CO].
[75] D. Anderhalden and J. Diemand, JCAP **1304**, 009 (2013), [Erratum: JCAP1308,E02(2013)], arXiv:1302.0003 [astro-ph.CO].
[76] T. Ishiyama, Astrophys. J. **788**, 27 (2014), arXiv:1404.1650 [astro-ph.CO].
[77] V. Springel, S. D. M. White, C. S. Frenk, J. F. Navarro, A. Jenkins, M. Vogelsberger, J. Wang, A. Ludlow, and A. Helmi, Nature **456N7218**, 73 (2008).
[78] L. Gao, C. S. Frenk, A. Jenkins, V. Springel, and S. D. M. White, Mon. Not. Roy. Astron. Soc. **419**, 1721 (2012), arXiv:1107.1916 [astro-ph.CO].
[79] M. Kamionkowski, S. M. Koushiappas, and M. Kuhlen, Phys. Rev. **D81**, 043532 (2010), arXiv:1001.3144 [astro-ph.GA].
[80] M. A. Sanchez-Conde, M. Cannoni, F. Zandanel, M. E. Gomez, and F. Prada, JCAP **1112**, 011 (2011), arXiv:1104.3530 [astro-ph.HE].
[81] R. Bartels and S. Ando, Phys. Rev. **D92**, 123508 (2015), arXiv:1507.08656 [astro-ph.CO].
[82] . Molin, M. A. Snchez-Conde, S. Palomares-Ruiz, and F. Prada, (2016), arXiv:1603.04057 [astro-ph.CO].
[83] J. Zavala and N. Afshordi, Mon. Not. Roy. Astron. Soc. **441**, 1317 (2014), arXiv:1308.1098 [astro-ph.CO].
[84] J. Zavala and N. Afshordi, Mon. Not. Roy. Astron. Soc. **441**, 1329 (2014), arXiv:1311.3296 [astro-ph.CO].
[85] J. Zavala and N. Afshordi, Mon. Not. Roy. Astron. Soc. **457**, 986 (2016), arXiv:1508.02713 [astro-ph.CO].
[86] J. Einasto, Trudy Inst. Astroz. Alma-Ata **51**, 87 (1965).
[87] W. Wang, J. Han, A. P. Cooper, S. Cole, C. Frenk, and B. Lowing, Mon. Not. Roy. Astron. Soc. **453**, 377 (2015), arXiv:1502.03477 [astro-ph.GA].
[88] G. Bertone, M. Cirelli, A. Strumia, and M. Taoso, JCAP **0903**, 009 (2009), arXiv:0811.3744 [astro-ph].
[89] S. Ando, Phys. Rev. **D80**, 023520 (2009), arXiv:0903.4685 [astro-ph.CO].
[90] M. Boylan-Kolchin, V. Springel, S. D. M. White, and A. Jenkins, Mon. Not. Roy. Astron. Soc. **406**, 896 (2010), arXiv:0911.4484 [astro-ph.CO].
[91] A. Klypin, S. Trujillo-Gomez, and J. Primack, Astrophys. J. **740**, 102 (2011), arXiv:1002.3660 [astro-ph.CO].

[92] M. Ackermann *et al.* (Fermi-LAT), Astrophys. J. **810**, 14 (2015), arXiv:1501.06054 [astro-ph.HE].
[93] M. Fornasa, L. Pieri, G. Bertone, and E. Branchini, Phys. Rev. **D80**, 023518 (2009), arXiv:0901.2921 [astro-ph.CO].
[94] G. Steigman, B. Dasgupta, and J. F. Beacom, Phys. Rev. **D86**, 023506 (2012), arXiv:1204.3622 [hep-ph].
[95] M. Ackermann *et al.* (Fermi-LAT), Phys. Rev. Lett. **115**, 231301 (2015), arXiv:1503.02641 [astro-ph.HE].
[96] S. Ando and K. Ishiwata, JCAP **1505**, 024 (2015), arXiv:1502.02007 [astro-ph.CO].
[97] M. G. Baring, T. Ghosh, F. S. Queiroz, and K. Sinha, Phys. Rev. **D93**, 103009 (2016), arXiv:1510.00389 [hep-ph].
[98] M. Ajello *et al.*, Astrophys. J. **800**, L27 (2015), arXiv:1501.05301 [astro-ph.HE].
[99] M. Ajello *et al.*, Astrophys. J. **751**, 108 (2012), arXiv:1110.3787 [astro-ph.CO].
[100] I. Tamborra, S. Ando, and K. Murase, JCAP **1409**, 043 (2014), arXiv:1404.1189 [astro-ph.HE].
[101] A. M. Brown, C. Boehm, J. Graham, T. Lacroix, P. M. Chadwick, and J. Silk, (2016), arXiv:1603.05469 [astro-ph.HE].
[102] J. Ripken, A. Cuoco, H.-S. Zechlin, J. Conrad, and D. Horns, JCAP **1401**, 049 (2014), arXiv:1211.6922 [astro-ph.HE].
[103] B. S. Acharya *et al.*, Astropart. Phys. **43**, 3 (2013).
[104] A. A. Moiseev *et al.*, (2015), arXiv:1508.07349 [astro-ph.IM].
[105] M. G. Aartsen *et al.* (IceCube), Phys. Rev. Lett. **111**, 021103 (2013), arXiv:1304.5356 [astro-ph.HE].
[106] M. G. Aartsen *et al.* (IceCube), Science **342**, 1242856 (2013), arXiv:1311.5238 [astro-ph.HE].
[107] M. G. Aartsen *et al.* (IceCube), Phys. Rev. Lett. **113**, 101101 (2014), arXiv:1405.5303 [astro-ph.HE].
[108] M. G. Aartsen *et al.* (IceCube), (2016), arXiv:1607.08006 [astro-ph.HE].
[109] M. G. Aartsen *et al.* (IceCube), Astropart. Phys. **66**, 39 (2015), arXiv:1408.0634 [astro-ph.HE].

FIGURES

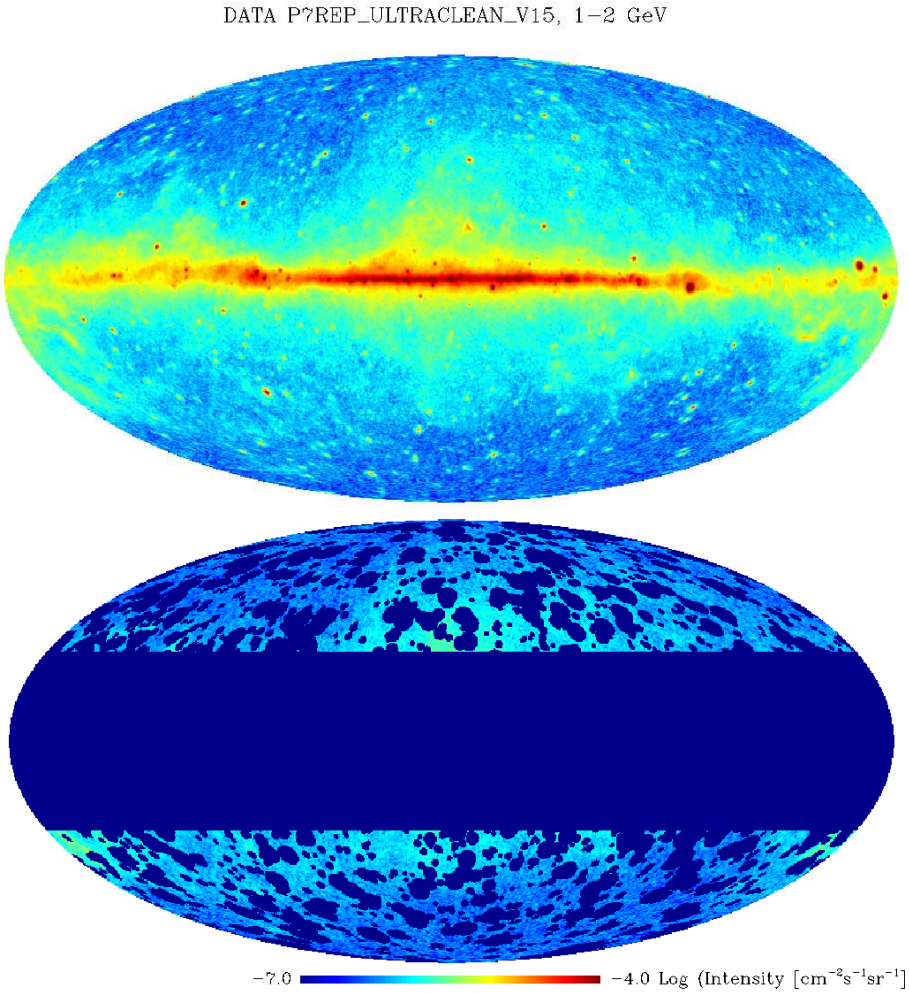

FIG. 1. Intensity maps (in $\mathrm{cm}^{-2}\mathrm{s}^{-1}\mathrm{sr}^{-1}$) in Galactic coordinates for energies between 1.0 and 2.0 GeV, shown unmasked (*top*) and after applying the default mask removing sources in 3FGL, as described in Sec. III B (*bottom*). Data used here follow the default processing (see Sec. II), but they include both front- and back-converting events. Both maps have been smoothed with a gaussian beam with $\sigma = 0.5^\circ$ and their projection scheme is Mollweide.

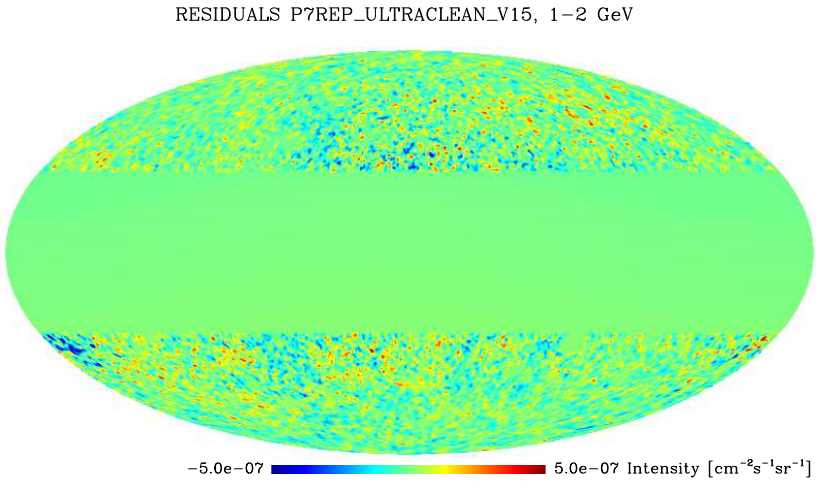

FIG. 2. Same as the bottom panel of Fig. 1 but with our model for the Galactic foreground subtracted (see Sec. III C). The residuals have been smoothed with a gaussian beam with $\sigma = 1^\circ$. The projection scheme is Mollweide.

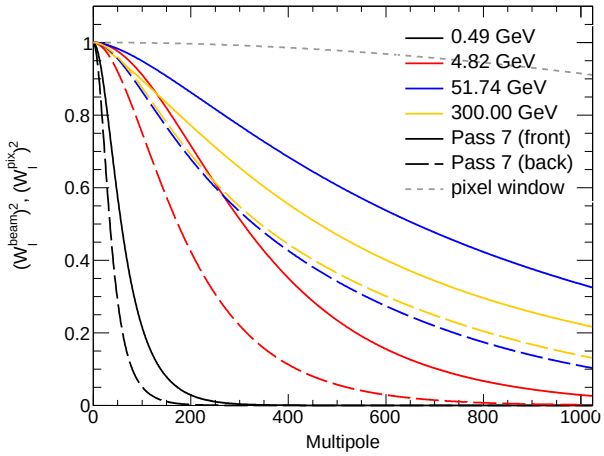

FIG. 3. Pixel and beam window functions as a function of energy and for different data selections. The gray short-dashed line shows the pixel window function of a HEALPix map with `Nside`=1024. The pixel window function is independent of energy and IRFs. The solid and long-dashed lines show the beam window functions for P7REP_ULTRACLEAN_V15 IRFs. The solid lines are for front-converting events and the long-dashed ones for back-converting events. The different colors stand for 4 different representative energies.

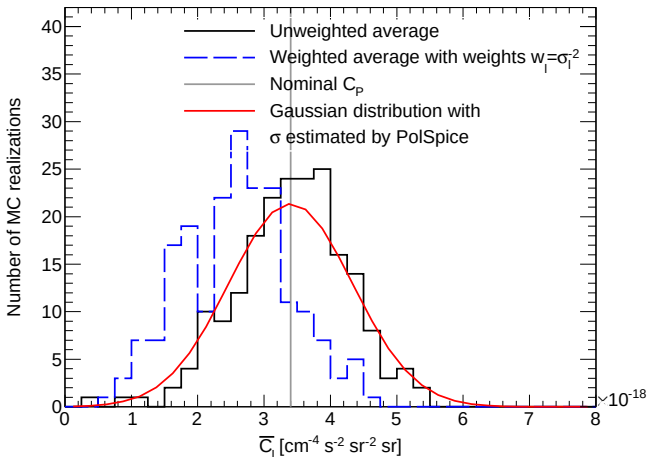

FIG. 4. Comparison between different methods to bin the auto-APS measured in the bin between $\ell = 243$ and 317 from the MC simulations described in the text. The nominal $C_{\rm P}$ is represented by the vertical grey line. The solid black histogram shows the distribution of the measured $\overline{C_\ell}$ for the 200 simulated realizations, where the binned auto-APS is computed by an unweighted average. The dashed blue histogram denotes the case of a weighted average with weights given in Eq. 8. The solid red curves is a Gaussian distribution centered on the nominal $C_{\rm P}$ and with a standard deviation of $9.3 \times 10^{-19}\,{\rm cm}^{-4}{\rm s}^{-2}{\rm sr}^{-1}$, as estimated with PolSpice.

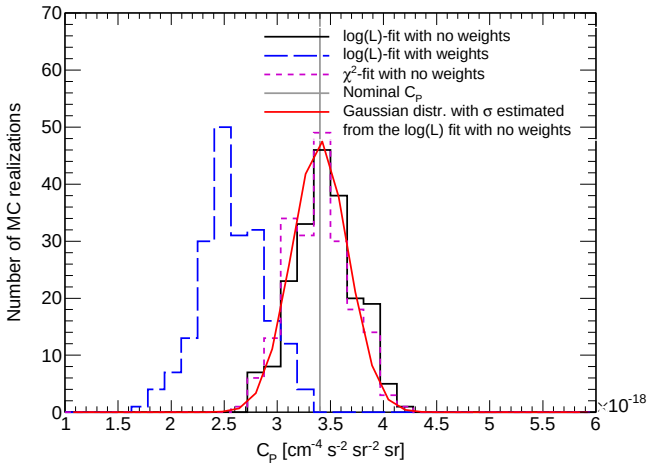

FIG. 5. Comparison between different methods to measure the Poissonian $C_{\rm P}$ in the MC simulations, given the binned $\overline{C_\ell}$. The nominal $C_{\rm P}$ is represented by the vertical grey line. The solid black histogram shows the distribution of the Poissonian $C_{\rm P}$ for the 200 simulated realizations obtained by maximazing the $\log\mathcal{L}$ in Eq. 10 over the multipole range from 49 to 706. The binned $\overline{C_\ell}$ in Eq. 10 are computed with no weights. If the weighted average is considered, the distribution of $C_{\rm P}$ is shown by the long-dashed blue histogram, which is clearly biased low. The short-dashed pink histogram shows the distribution of $C_{\rm P}$ computed by the minimization of the χ^2 in Eq. 9 from $\overline{C_\ell}$ binned with no weights. The solid red curve is a Gaussian distribution centered on the nominal $C_{\rm P}$ and with a standard deviation of $2.6 \times 10^{-19}{\rm cm}^{-4}{\rm s}^{-2}{\rm sr}^{-1}$, as estimated from the $\log\mathcal{L}$ method.

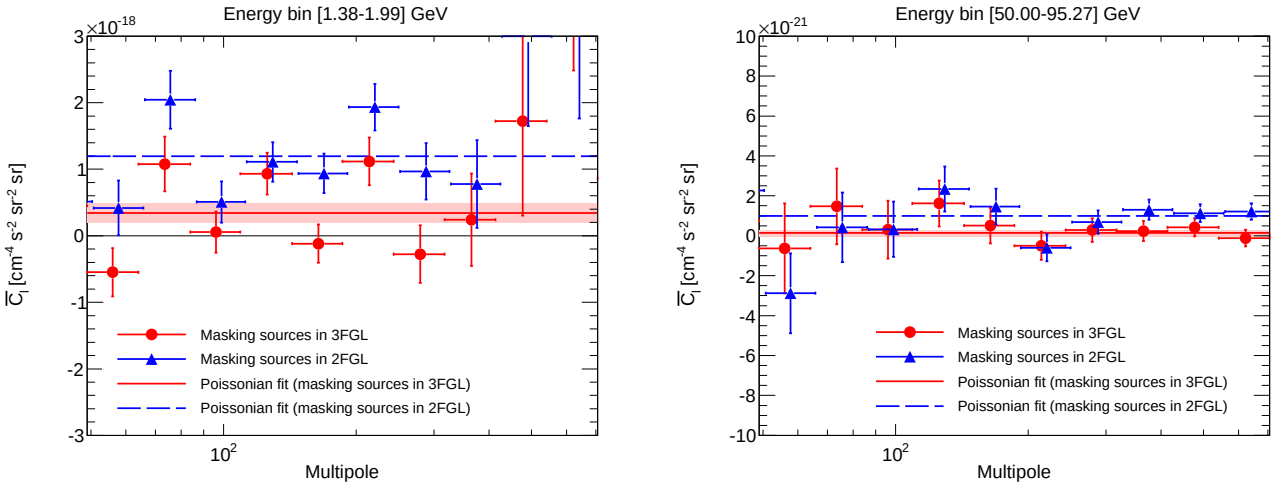

FIG. 6. Auto-APS of the IGRB for 2 representative energy bins (between 1.38 and 1.99 GeV in the left panel and between 50.0 and 95.27 GeV in the right panel) and for the reference data set (P7REP_ULTRACLEAN_V15 front events) using the reference mask which excludes $|b| < 30^\circ$ and 3FGL sources (red circles). The blue triangles show the same but masking the sources in 2FGL. Data have been binned as described in Sec. IV A. The solid red line shows the best-fit $C_{\rm P}$ for the red data points, with the pink band indicating its 68% CL error. The dashed blue line corresponds to the best-fit $C_{\rm P}$ for the blue data points. Note that only the results in our signal region (i.e. between $\ell = 49$ and 706) are plotted and that the scale of the y-axis varies in the two panels. Also, the blue triangles have been slightly shifted horizontally with respect to the red circles to increase the readibility of the plots. This will happen also in many of the following plots.

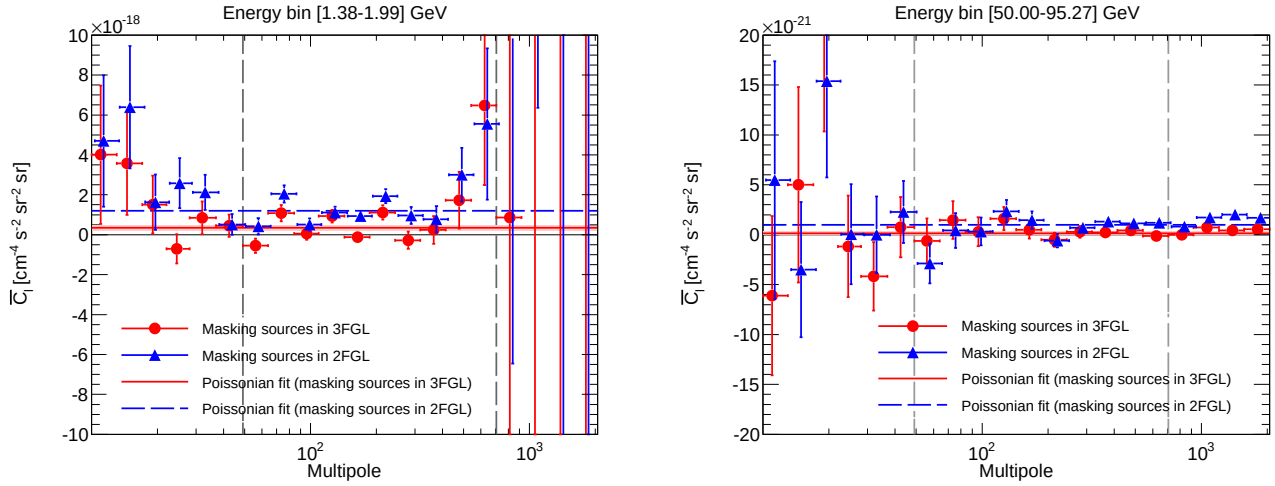

FIG. 7. Same as Fig. 6, but showing a wider range in multipole, going from $\ell = 10$ to 2000. The two dashed grey vertical lines indicate the lower and upper bounds of the multipole range used for the present analysis. Note the different scale of the y-axis in each panel.

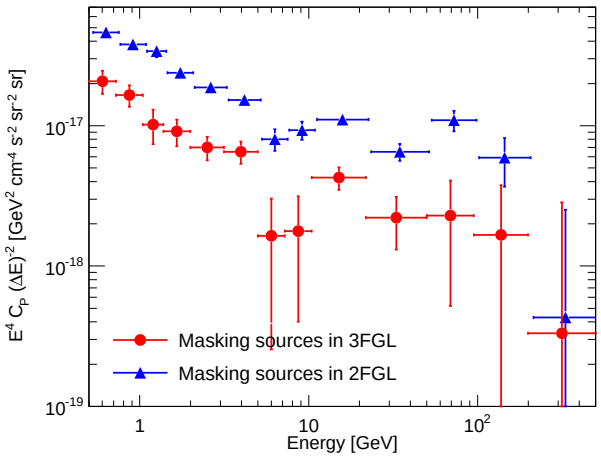

FIG. 8. Anisotropy energy spectra for the auto-APS using the reference data set with the default 3FGL mask (red circles) in comparison with the case in which we use the default mask around 2FGL sources (blue triangles).

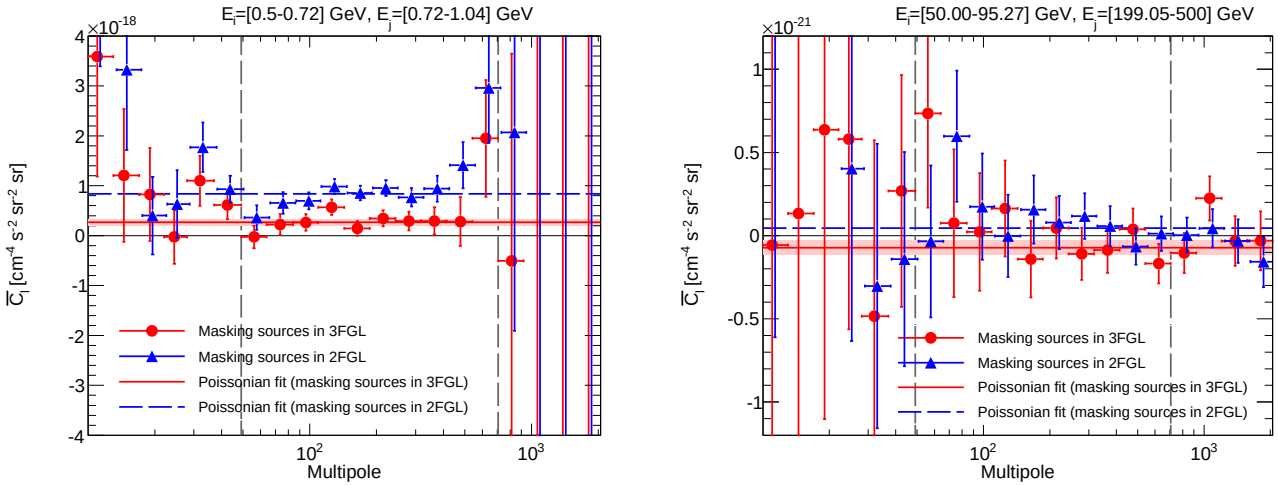

FIG. 9. Cross-APS for two representative combinations of energy bins as indicated above the two panels. The default data set and 3FGL mask are used to compute the red circles, while the blue triangles are for the mask excluding 2FGL sources. The vertical dashed grey lines denote the bounds of the multipole range used in the analysis. The best-fit C_P is shown as a solid red line in the case of the mask around 3FGL sources, with a pink band indicating its 68% CL error. The dashed blue line corresponds to the best-fit C_P for the blue data points (i.e. masking 2FGL sources).

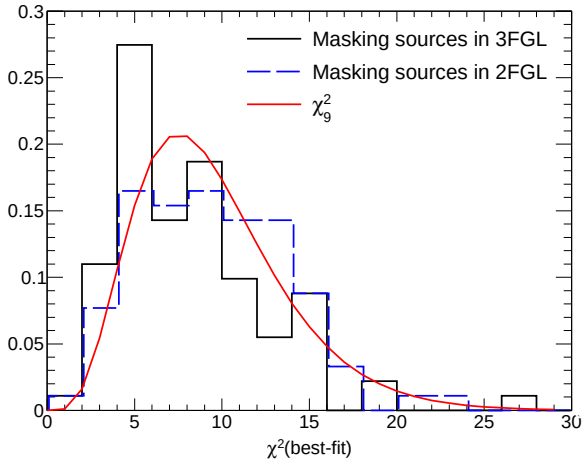

FIG. 10. Normalized distribution of the χ^2 (defined as in Eq. 9) for the best-fit Poissonian $C_{\rm P}$ for all 91 independent combinations of energy bins. The solid black line is for the case when 3FGL sources are masked and the dashed blue line is for the mask covering 2FGL sources. The solid red curve is a χ^2 distribution with 9 degrees of freedom.

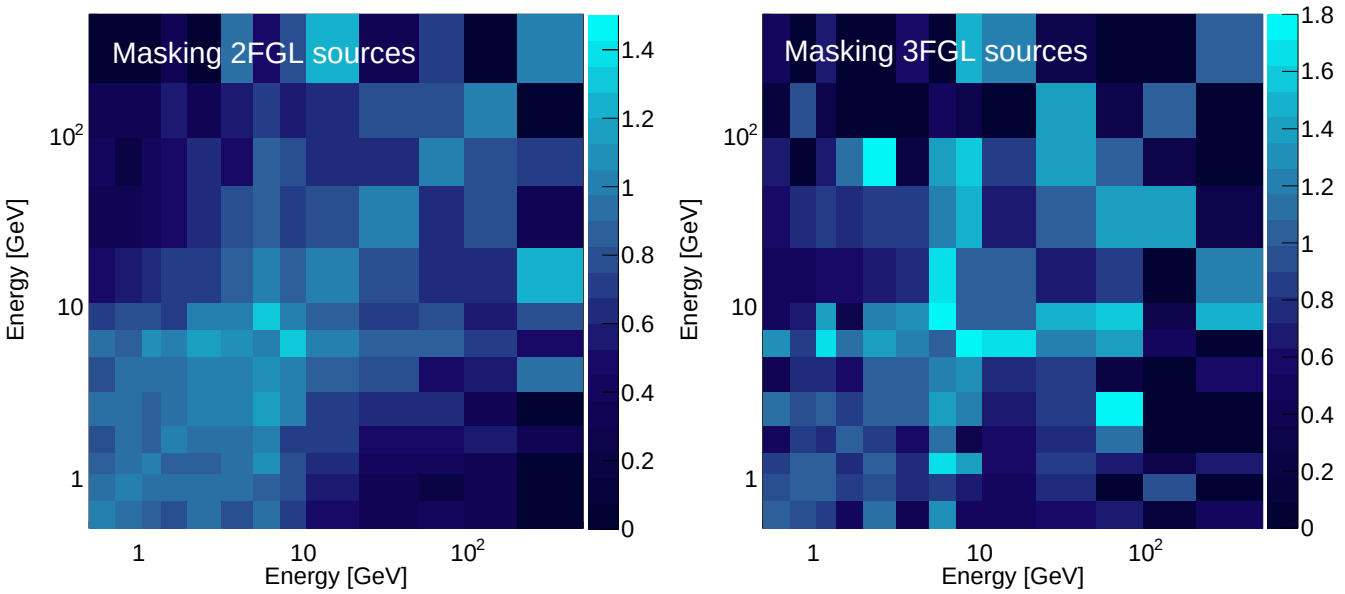

FIG. 11. Cross-correlation coefficients between energy bins. Each pixel in the panels corresponds to a pair (i, j) of energy bins and it is colored according to the cross-correlation coefficent $r_{i,j}$. By construction the panels are symmetric with respect to the diagonal. The panel on the left refers to the default data set with a mask that covers the sources in 2FGL, while the one on the right is for the mask covering 3FGL sources. Cross-correlation coefficents below 1 indicate that the signal is due to multiple populations of sources.

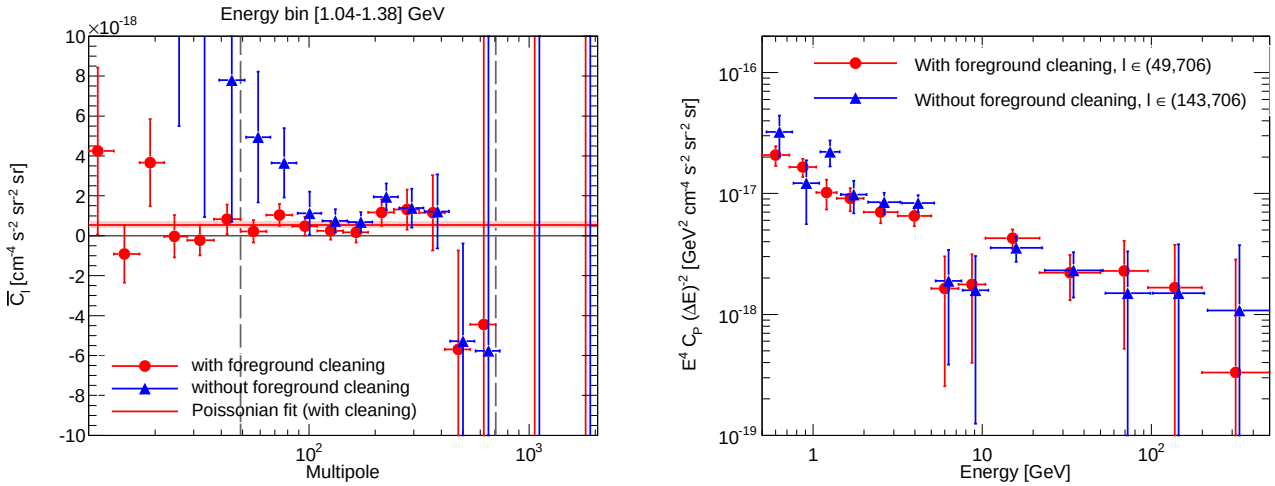

FIG. 12. *Left:* Auto-APS in the energy bin between 1.04 and 1.38 GeV, comparing the data with (red circles) and without (blue triangles) foreground cleaning. The solid red line indicates the best-fit $C_{\rm P}$ for the case with foreground cleaning, and the pink band its 68% CL error. The two dashed vertical lines mark our signal region in multipole. *Right:* Poissonian auto-APS as a function of the energy for the case with foreground cleaning and a signal region between $\ell = 49$ and 706 (red circles) and for the case without foreground cleaning and a signal region between $\ell = 143$ and 706 (blue triangles). Default data selection and 3FGL mask are used.

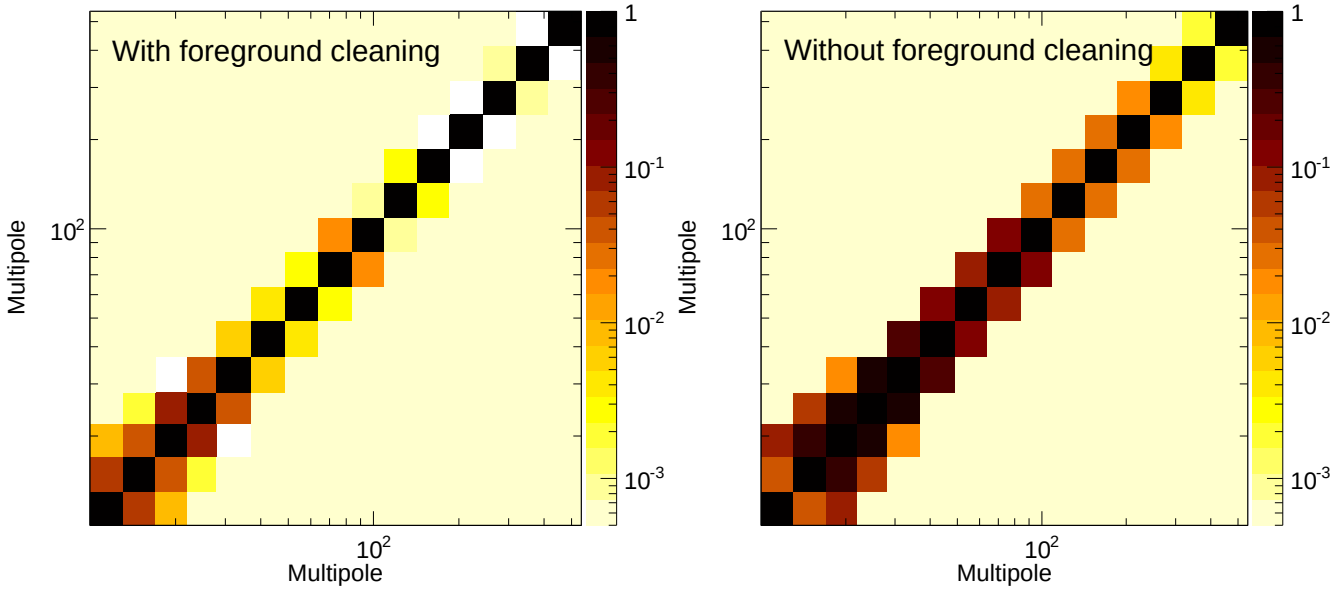

FIG. 13. Normalized covariance matrix ($\sigma_{i,j}/\sqrt{\sigma_{i,i}\sigma_{j,j}}$) of the binned $\overline{C_\ell}$ shown in the left panel of Fig. 12, i.e., for the energy bin between 1.04 and 1.38 GeV, default data selection and default mask covering 3FGL sources. The left panel shows the case with foreground cleaning, while the right panel is for the uncleaned case. The comparison between the two panels indicates that large covariances are present in the case without foreground cleaning up to multipoles $\ell \sim 100$.

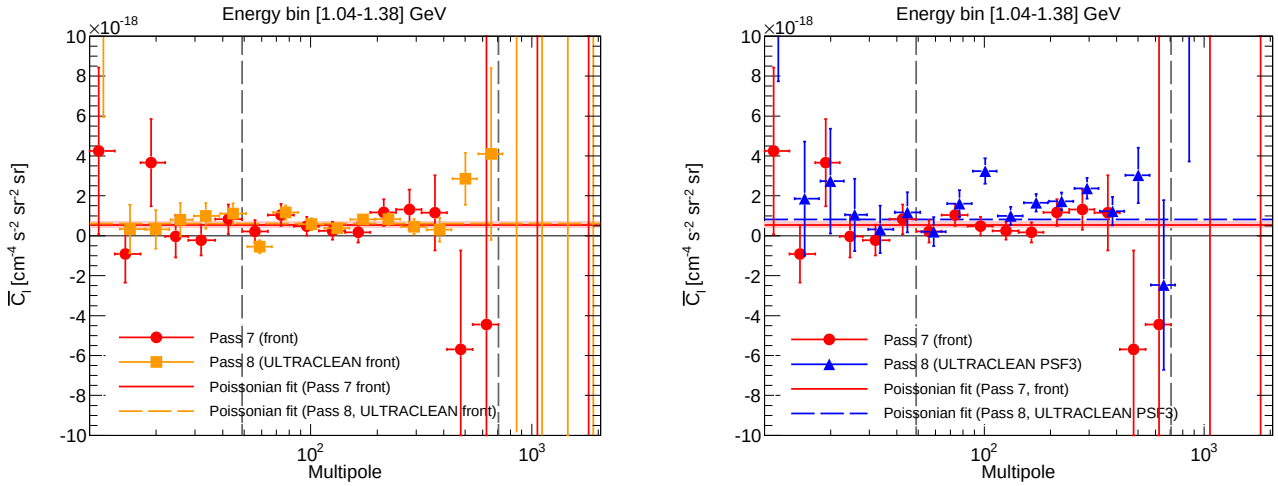

FIG. 14. *Left:* Comparison of the auto-APS measurement in the energy bin between 1.04 and 1.38 GeV between the default Pass 7 data set (red circles) and the Pass 8 front event selection (orange squares). *Right:* same as the left panel but the comparison is between the Pass 7 data (red circles) and the Pass 8 PSF3 event selection (blue triangles). The solid red line marks the best-fit $C_{\rm P}$ for the default Pass 7 data set, with the pink band indicating its 68% CL error. The dashed orange (blue) line gives the best-fit $C_{\rm P}$ for Pass 8 front (PSF3) in the left (right) panel. The vertical grey dashed lines mark the signal region between $\ell = 49$ and 706. The default mask covering 3FGL sources is applied.

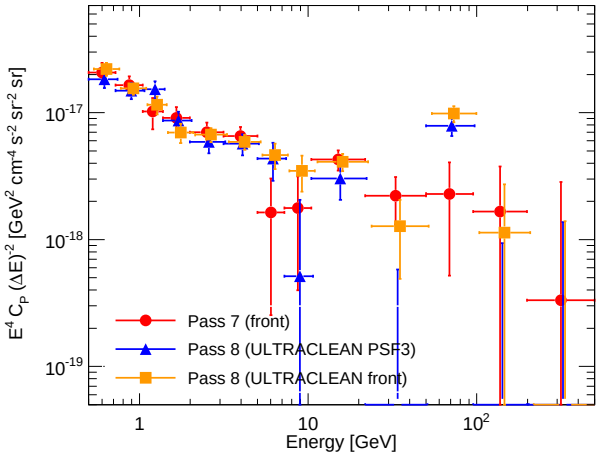

FIG. 15. Poissonian auto-APS as a function of energy for the Pass 7 (red circles), Pass 8 front (orange squares) and Pass 8 PSF3 (blue triangles) data sets. The default mask covering 3FGL sources is applied.

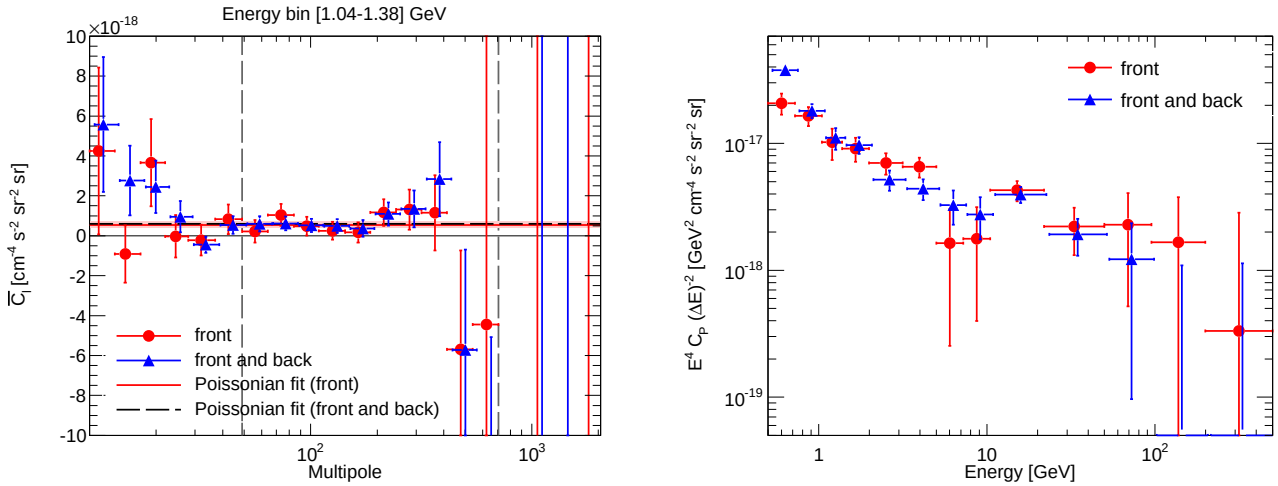

FIG. 16. *Left:* Comparison of the auto-APS in the energy bin between 1.04 and 1.38 GeV between the default data set which uses only front events (red circles) and the front+back data set (blue triangles). The solid red line marks the best-fit $C_{\rm P}$ for the default front-converting data, with the pink band indicating its 68% CL error. The dashed blue line gives the best-fit $C_{\rm P}$ for the front+back data set. The vertical grey dashed lines mark the signal region between $\ell = 49$ and 706. *Right:* Poissonian auto-APS as a function of energy for the front events (red circles) and the front+back ones (blue triangles). The default mask covering 3FGL sources is applied for both panels.

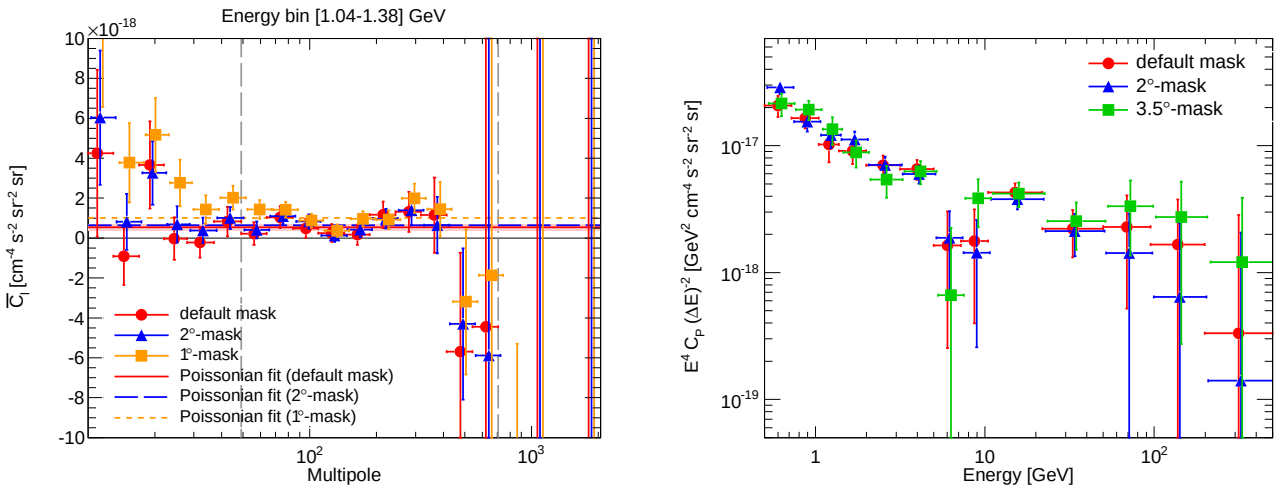

FIG. 17. *Left:* Comparison of the auto-APS in the energy bin from 1.04 to 1.38 GeV among the case with the default mask covering the sources in 3FGL (red circles), the case with the 2°-mask (blue triangles) and the one with the 1°-mask (orange squares). The solid red line marks the best-fit $C_{\rm P}$ for the default mask, with the pink band indicating its 68% CL error. The long-dashed blue line gives the best-fit $C_{\rm P}$ when the 2°-mask is employed and the short-dashed orange one for the case with the 1°-mask. The vertical grey dashed lines mark the signal region between $\ell = 49$ and 706. *Right:* Poissonian auto-APS as a function of energy for the case with the default mask (red circles), the 2°-mask (blue triangles) and the 3.5°-mask (green squares).

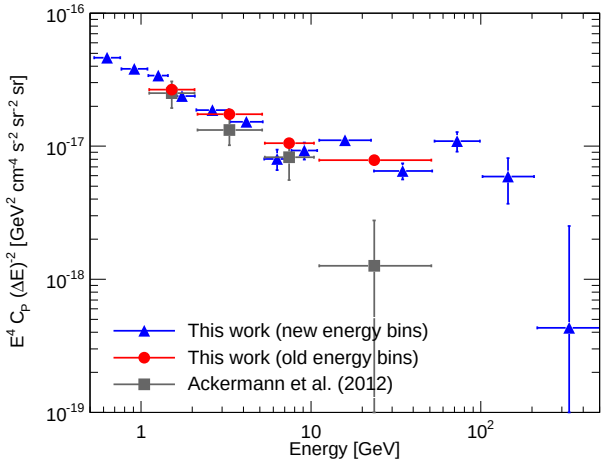

FIG. 18. Poissonian auto-APS as a function of energy for the default data set in this analysis, with 13 energy bins (blue triangles) and with the 4 energy bins used in Ref. [1] (red circles). Note that data are obtained using the mask that covers a 2°-circle around each source in 2FGL. The grey squares denote the measurement from Ref.[1] using the same mask.

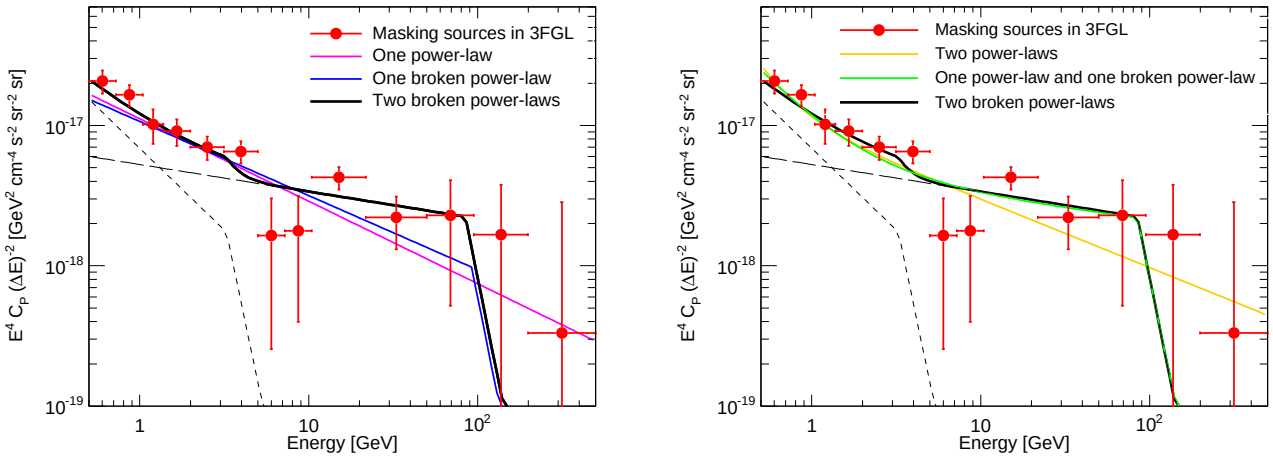

FIG. 19. Anisotropy energy spectrum for the default data set masking the sources in 3FGL (red circles). The different lines correspond to the best-fit models to the measured auto- and cross-APS with one or two populations of unresolved sources. The solid magenta line and the solid blue one (left panel) are for one population emitting as a power law or as a broken power law, respectively. The solid yellow line (right panel) is for two populations with power-law energy spectra. The solid green line (right panel) shows the best-fit in the case of one population emitting as a power law and another as a broken power law. Finally, the thicker solid black line (present in both panels) represents the case of two populations emitting as broken power laws. This is the scenario that best fits the data. In this case, the contribution of the two components are shown as short-dashed and long-dashed black lines.

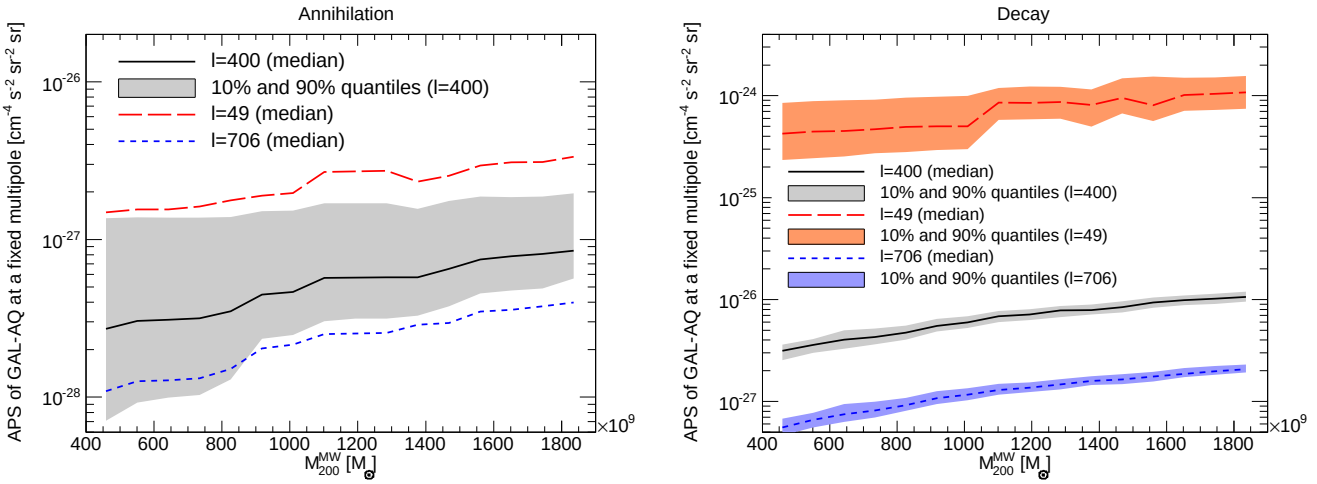

FIG. 20. Dependence of the APS of the GAL-AQ component on the MW mass. *Left:* The lines show the auto-APS at a fixed multipole ($\ell = 49$ for the long-dashed red line, $\ell = 400$ for the solid black one and $\ell = 706$ for the short-dashed blue one) as a function of the mass of the DM halo of the MW, in our simulation of GAL-AQ described in the text. The auto-APS is computed between 0.5 and 0.72 GeV, for $m_\chi = 2.203$ TeV with a thermal annihilation cross section $\langle \sigma_{\rm ann} v \rangle = 3 \times 10^{-26} {\rm cm}^3 {\rm s}^{-1}$ and for annihilations into $b\bar{b}$. For each value of the MW mass, 100 realizations of GAL-AQ are computed for different positions of the observer. The lines refer to the median of the distribution of the corresponding auto-APS, while the grey band denotes the variability between the 10% and the 90% quantiles of the distribution. The band is present only for the case with $\ell = 400$ for clarity. *Right*: The same as in the left panel but for decaying DM. The auto-APS is computed in the same energy bin, for the same m_χ and a decay lifetime of 2×10^{27}s.

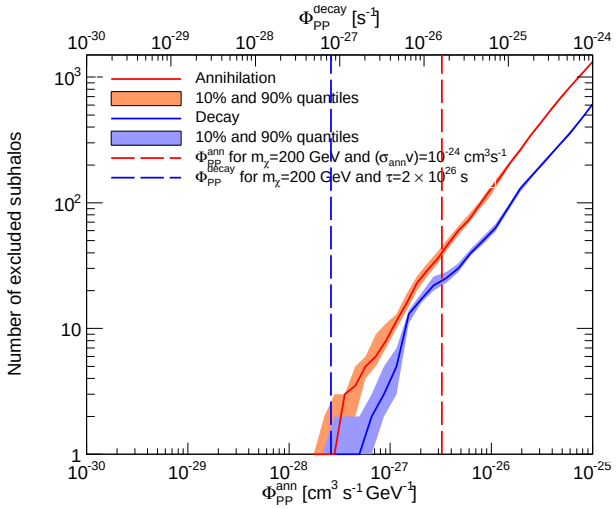

FIG. 21. The solid lines show the number of the DM subhalos in GAL-AQ with an energy flux above 0.1 GeV that is larger than 3×10^{-12}erg cm^{-2}s^{-1}, i.e., the point-source sensitivity of *Fermi* LAT in the 3FGL catalog [92]. The solid lines denote the median over 100 independent realizations differing by the position of the observer and they are plotted as a function of the particle physics factor, in the case of an annihilating DM candidate (red line and bottom axis) and for a decaying one (blue line and top axis). In both cases, annihilations/decays into $b\bar{b}$ are considered. The colored bands indicate the 10% and 90% quantiles among the 100 realizations. For reference, the $\Phi_{\rm PP}^{\rm ann}$ for $m_\chi = 200$ GeV, $\langle \sigma_{\rm ann} v \rangle = 10^{-24} {\rm cm}^3 {\rm s}^{-1}$ and annihilation into $b\bar{b}$ is marked by the dashed red line. Finally, the dashed blue line corresponds to the $\Phi_{\rm PP}^{\rm decay}$ for $m_\chi = 200$ GeV, $\tau = 2 \times 10^{26}$s and decaying into $b\bar{b}$.

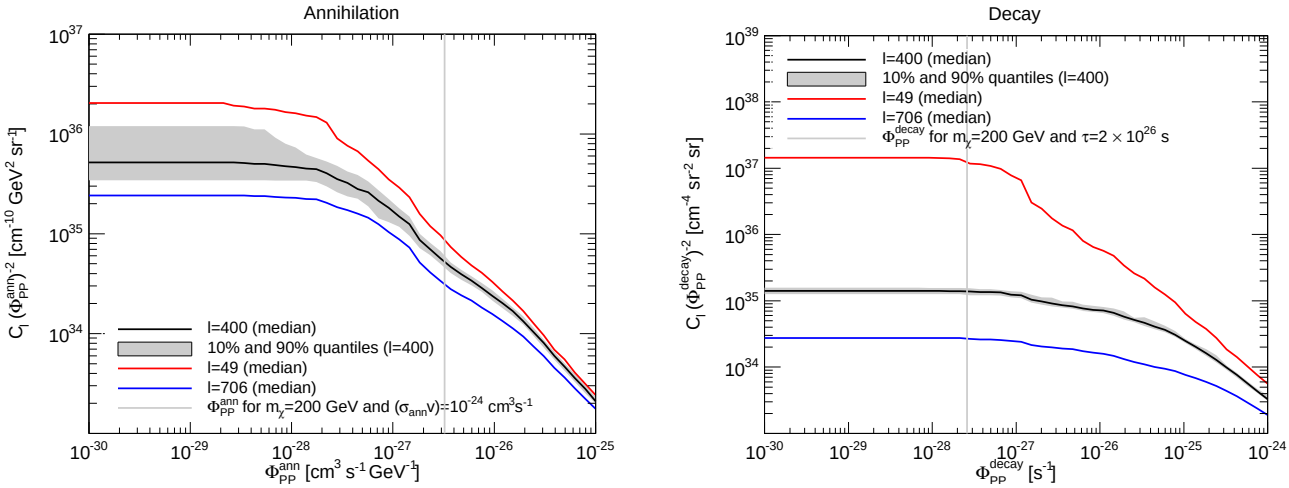

FIG. 22. Dependence of the APS of the GAL-AQ component on the Particle Physics factor defined in the text. *Left:* The solid lines show the DM-induced APS (computed above 0.1 GeV, for a fixed multipole and multiplied by $(\Phi_{\rm PP}^{\rm ann})^{-2}$) as a function of $\Phi_{\rm PP}^{\rm ann}$, neglecting the DM subhalos that would be detected individually according to the *Fermi* LAT sensitivity threshold in the 3FGL catalog [92]. The black, red and blue lines are for $\ell = 400$, $\ell = 49$ and $\ell = 706$. They indicate the median over the 100 realizations with different positions for the observer, while the grey band (only for the case with $\ell = 400$) shows the variabilty between the 10% and 90% quantiles. For reference, the value of $\Phi_{\rm PP}^{\rm ann}$ for $m_\chi = 200$ GeV, $\langle\sigma_{\rm ann}v\rangle = 10^{-24}{\rm cm}^3{\rm s}^{-1}$ and annihilation into $b\bar{b}$ is marked by the grey vertical line. *Right:* The same as in the left panel, but for a decaying DM candidate. The vertical grey line is the particle physics factor of a DM candidate with $m_\chi = 200$ GeV, $\tau = 2\times10^{26}$s and decaying into $b\bar{b}$. Note that the default mask covering 3FGL sources is employed when computing the auto-APS.

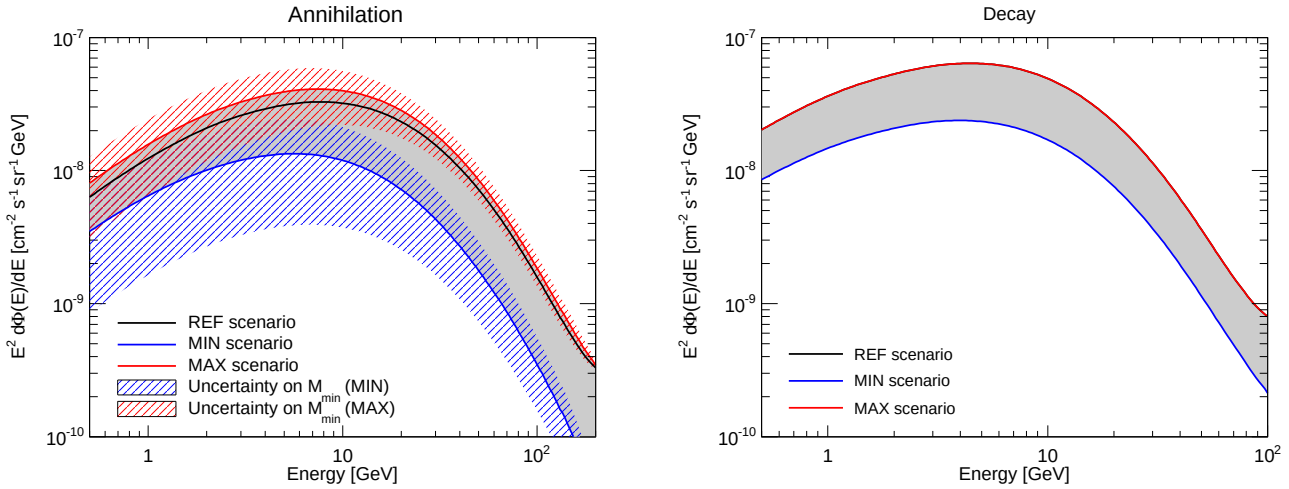

FIG. 23. *Left:* The predicted energy spectrum of the gamma-ray emission induced by the annihilation of a DM particle with a mass of 212 GeV, $\langle\sigma_{\rm ann}v\rangle = 3\times10^{-26}{\rm cm}^3{\rm s}^{-1}$ and annihilation into $b\bar{b}$. The black line stands for the REF scenario, while the red and blue ones are for the MAX and MIN cases. Thus, the grey band determines the variability between the MIN and MAX scenarios. In all cases $M_{\rm min} = 10^{-6}M_\odot$ (see text for details). The red and blue shaded areas indicate how the MAX and MIN benchmarks change if we let $M_{\rm min}$ vary between 10^{-6} and 1 $M_\odot$. *Right*: The same as in the left panel but for a decaying DM particle with a mass of 212 GeV and a decaying lifetime of 2×10^{27} s. The red and black lines overlap.

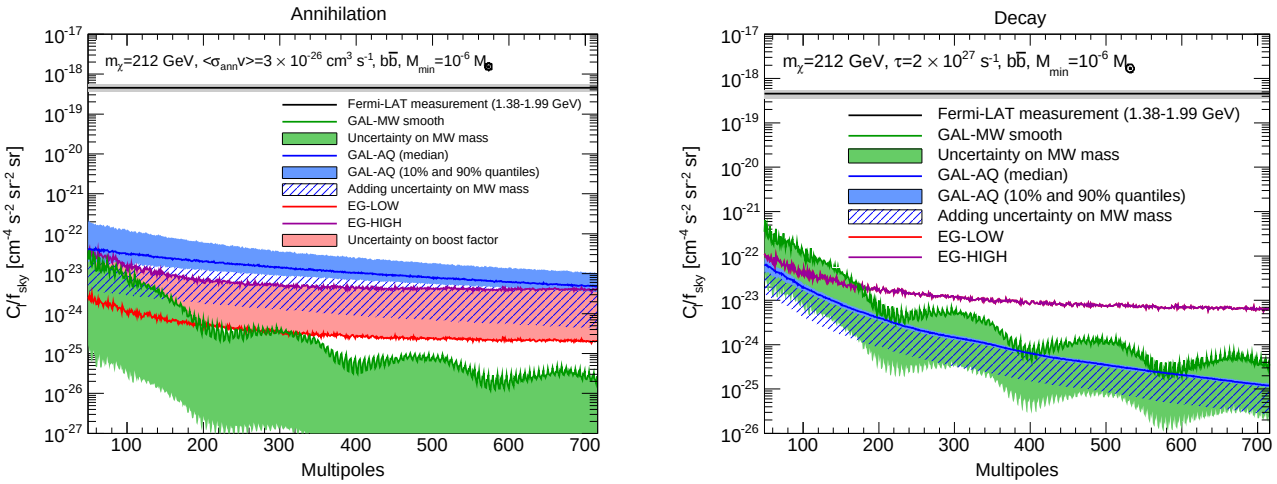

FIG. 24. *Left:* Auto-APS in the energy bin between 1.38 and 1.99 GeV, for a DM candidate with a mass of 212 GeV, $\langle\sigma_{\rm ann}v\rangle = 3\times10^{-26}{\rm cm}^3{\rm s}^{-1}$ and annihilation into $b\bar{b}$. The auto-APS is divided by $f_{\rm sky}$ to correct for the presence of the mask described in Sec. III B. The black solid line and the grey band indicate the Poissonian auto-APS measured in this energy bin and for the mask around 3FGL sources (see Sec. V). The solid blue line is the median of the auto-APS for GAL-AQ over the 100 realizations with different positions for the observer and the blue band shows the variability between the 10% and 90% quantiles. The uncertainty band on GAL-AQ extends downwards (shaded blue area) if we account for an uncertainty of a factor 4 in the value of the mass of MW DM halo. The red and purple lines show the auto-APS for EG-LOW and EG-HIGH, for $M_{\rm min} = 10^{-6}M_\odot$. The green line stands for the GAL-MWsmooth component and the green band accounts for an uncertainty of a factor 4 in the mass of MW DM halo. The wiggles in this component are due to the mask applied to cover the Galactic plane (see text for details). *Right*: The same as in the left panel but for a decaying DM particle with a mass of 212 GeV and a decaying lifetime of 2×10^{27} s. The red and and purple lines overlap.

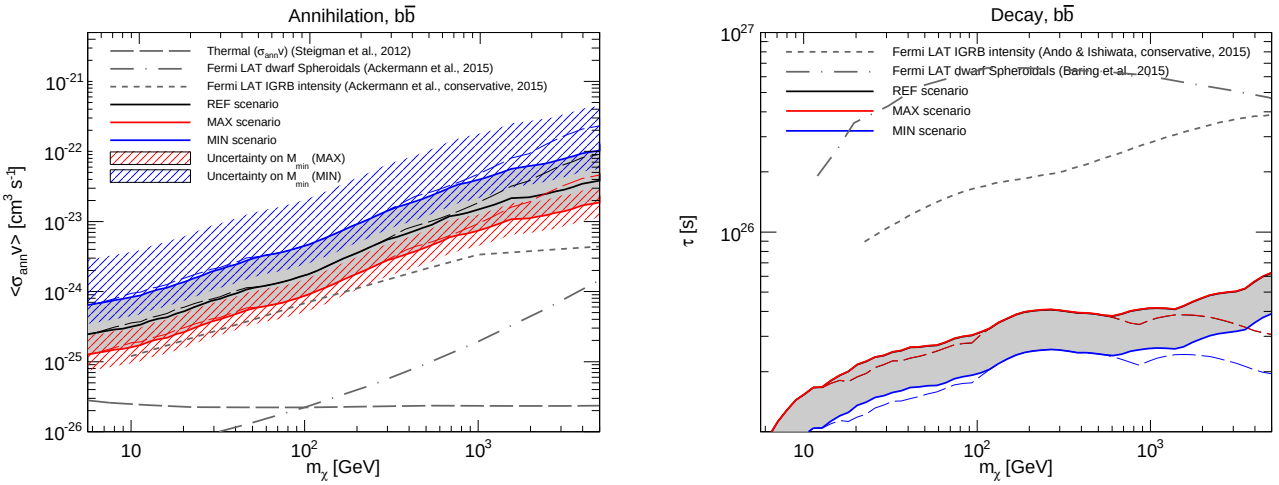

FIG. 25. Conservative exclusion limits on annihilating and decaying DM from the new APS measurement. *Left:* The solid lines show the upper limits on $\langle\sigma_{\rm ann}v\rangle$ derived from the auto- and cross-APS measured in Sec. III, as a function of m_χ, for $M_{\rm min} = 10^{-6}M_\odot$ and annihilations into $b\bar{b}$. The limits follow the conservative approach described in the text. The black line is for the REF scenario, while the red and blue ones are for MAX and MIN, respectively. The grey band between the MIN and MAX scenario represents our estimated total astrophysical uncertainty for $M_{\rm min} = 10^{-6}M_\odot$, accounting for all the sources of uncertainty mentioned in Sec. VII. The red and blue shaded bands describe the effect of changing $M_{\rm min}$ between $10^{-12}M_\odot$ and 1 $M_\odot$, for the MAX and MIN scenario. In the case of the black, red and blue dashed lines, the upper limits are derived only considering the measured auto-APS and neglecting the cross-APS. For comparison, the long-dashed grey line marks the annihilation cross section for thermal relics from Ref. [94] and the dash-dotted grey line the upper limit obtained in Ref. [95] from the combined analysis of 15 dwarf spheroidal galaxies. Finally, the short-dashed grey line shows the conservative upper limit derived in Ref. [31] from the intensity of the IGRB. *Right*: The same as in the left panel but for the lower limits on τ for decaying DM. The short-dashed grey line represents the lower limit obtained in Fig. 6 of Ref. [96] from the IGRB intensity, while the dash-dotted grey one is obtained from the combined analysis of 15 dwarf spheroidal galaxies in Ref. [97].

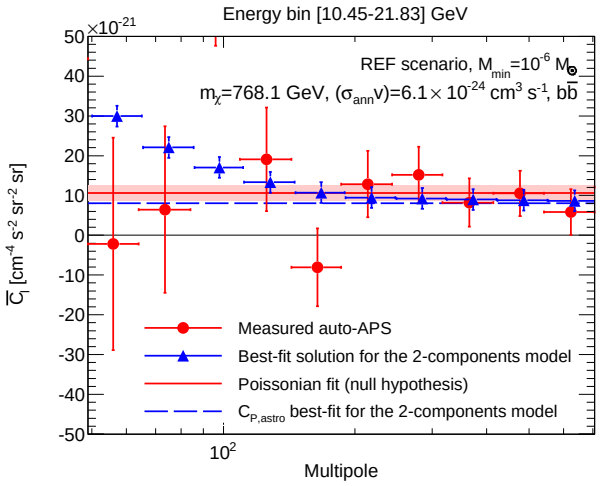

FIG. 26. Example of a fit to the binned APS $\overline{C_\ell}$ in our particular energy bins, in terms of the 2-component model described in the text. The red circles show the measured auto-APS in the energy bin between 10.4 and 21.8 GeV, as a function of multipole. The solid red line is the Poissonian best-fit APS in the null hypothesis and the pink band denotes its estimated 68% CL error. The dashed blue line denotes the best-fit of the Poissonian component when DM is included in the fit, for a DM mass of 768.1 GeV and a $\langle\sigma_{\rm ann}v\rangle$ of $6.12\times10^{-24}{\rm cm}^3{\rm s}^{-1}$, annihilation into $b\bar{b}$ and a REF scenario with $M_{\rm min}=10^{-6}M_\odot$. The best-fit signal (Poissonian plus DM component) is plotted by means of the blue triangles.

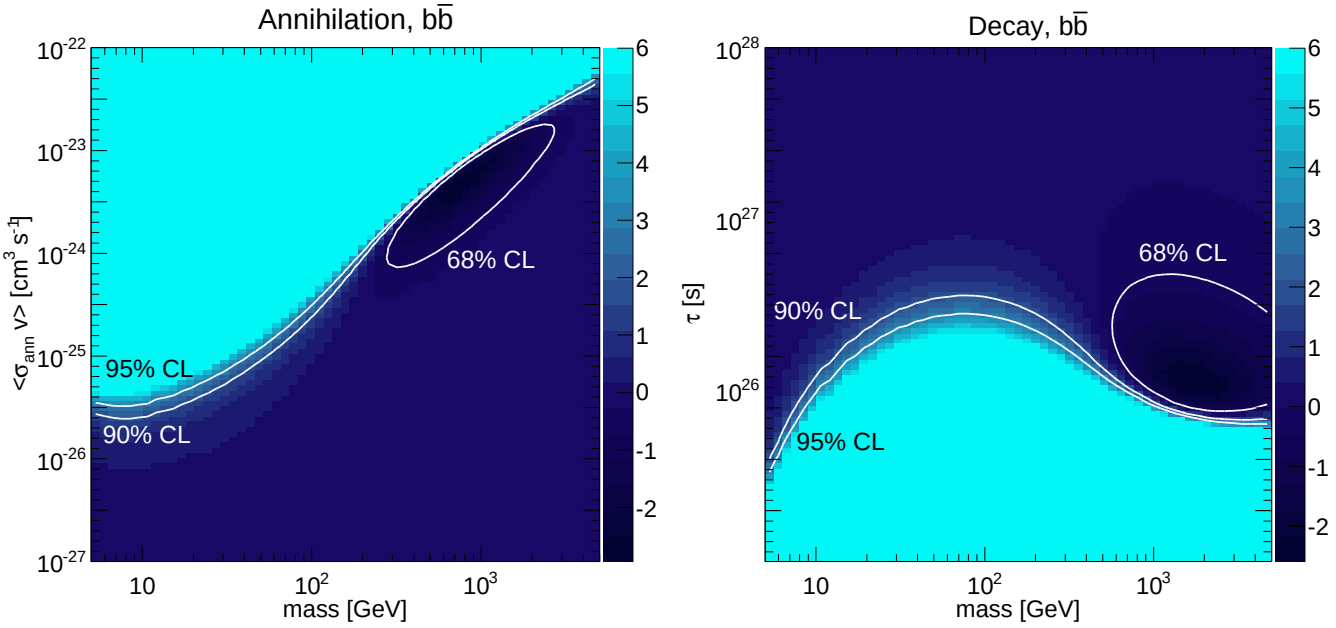

FIG. 27. $\Delta\chi^2$ between the best-fit solution for the 2-component scenario and the best fit in the null hypothesis. Results presented here refer to the REF scenario for annihilation/decay into $b\bar{b}$ and $M_{\rm min}=10^{-6}M_\odot$. *Left:* Each point in the $(m_\chi,\langle\sigma_{\rm ann}v\rangle)$ parameter space is colored according to its $\Delta\chi^2$, i.e. the difference between the χ^2 of the best fit to the auto- and cross-APS in terms of the 2-component model and the χ^2 of the best fit of the null hypothesis (i.e. no DM). The closed white contour marks the 68% CL region. The 90% and 95% CL regions are below the white open curves labelled "90% CL" and "95% CL" respectively. *Right*: The same as the left panel but for decaying DM.

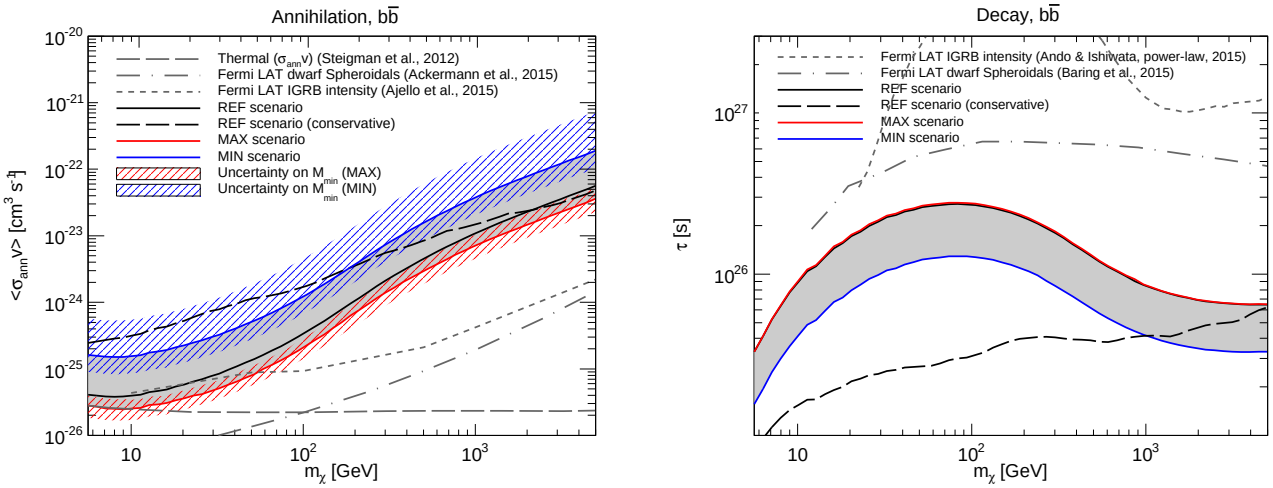

FIG. 28. Exclusion limits on annihilating and decaying DM from the fit to the binned $\overline{C_\ell}$ in terms of the 2-component model. *Left:* The solid lines show the upper limits that can be derived on $\langle\sigma_{\rm ann}v\rangle$ as a function of m_χ (for annihilations into $b\bar{b}$ quarks and $M_{\rm min} = 10^{-6}M_\odot$) by fitting the *Fermi* LAT data with a 2-component model that includes astrophysical sources and DM (see text for details). The black, blue and red lines correspond to the REF, MIN and MAX scenario. The blue and red shaded areas indicate how the MIN and MAX upper limits change when leaving $M_{\rm min}$ free to vary between $10^{-12}M_\odot$ and 1 $M_\odot$. The black dashed line is the REF upper limit in the conservative case, from Fig. 25, while the long-dashed grey line is the thermal annihilation cross section from Ref. [94]. The dot-dashed grey line is the upper limits derived in Ref. [95] from the combined analysis of 15 dwarf spheroidals, while the short-dashed grey line comes from the analysis of the IGRB intensity performed in Ref. [98]. *Right*: The same as in the left panel but for the lower limits on τ, in the case of decaying DM. The short-dashed grey line represents the lower limit obtained in Ref. [96] from the IGRB intensity. The line is taken from Fig. 5 of Ref. [96], where the IGRB is interpreted in terms of a component with a power-law emission spectrum and a DM contribution. Finally, the dot-dashed grey line is the upper limit from the analysis of 15 dwarf spheroidal galaxies performed in Ref. [97].

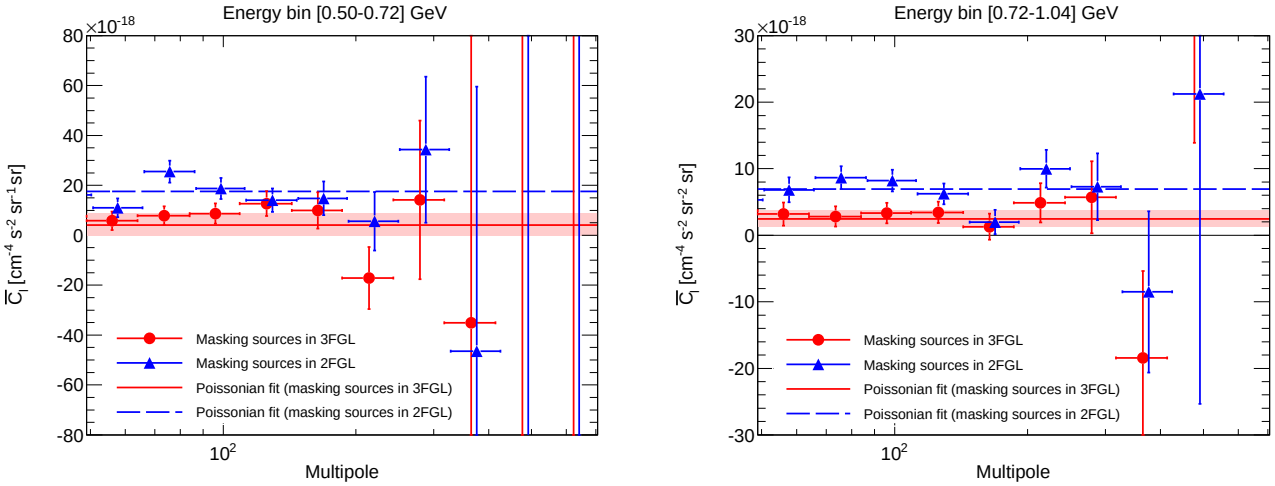

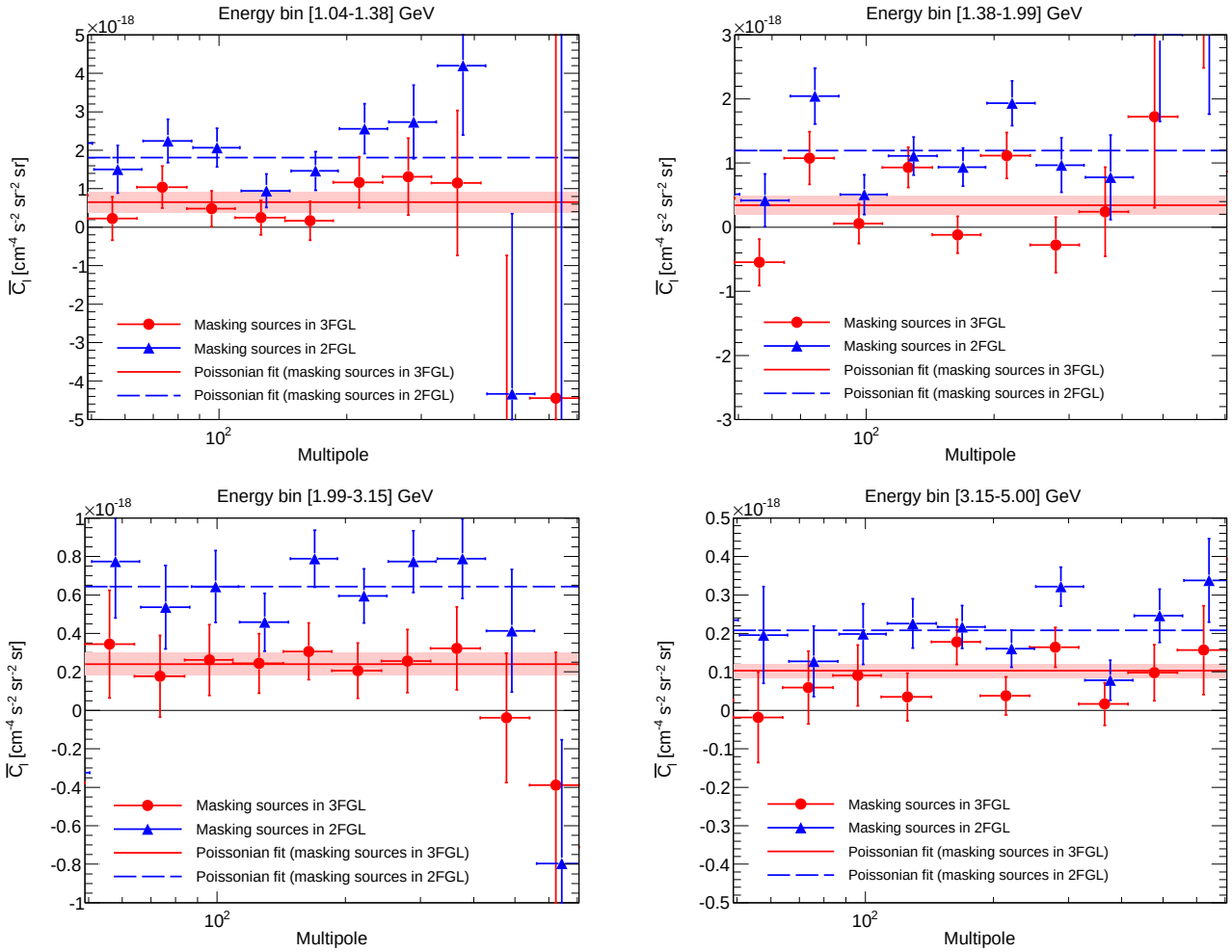

FIG. 29. Auto-APS of the IGRB for the first 6 energy bins and for the reference data set (P7REP_ULTRACLEAN_V15 front events) using the reference mask which excludes $|b| < 30^\circ$ and 3FGL sources (red circles). The blue triangles show the same but masking the sources in 2FGL, instead. Data have been binned as described in Sec. IV A. The solid red line shows the best-fit $C_{\rm P}$ for the red data points, with the pink band indicating its 68% CL error. The dashed blue line corresponds to the best-fit $C_{\rm P}$ for the blue data points. The energy range is indicated on the top of each panel. Note that only the results in our signal region (i.e. between $\ell = 49$ and 706) are plotted and that the scale of the y-axis can vary from panel to panel.

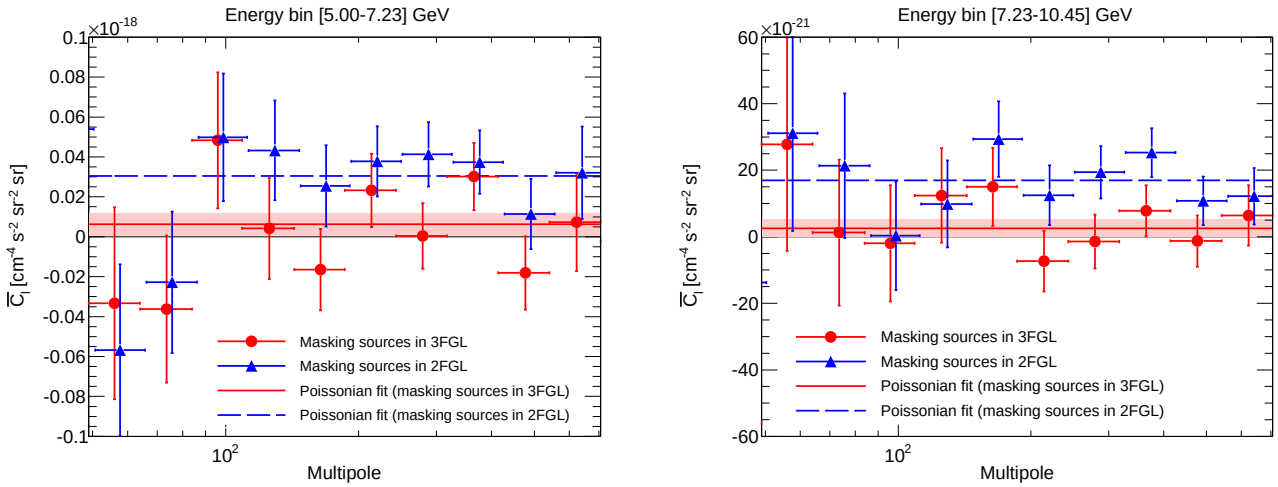

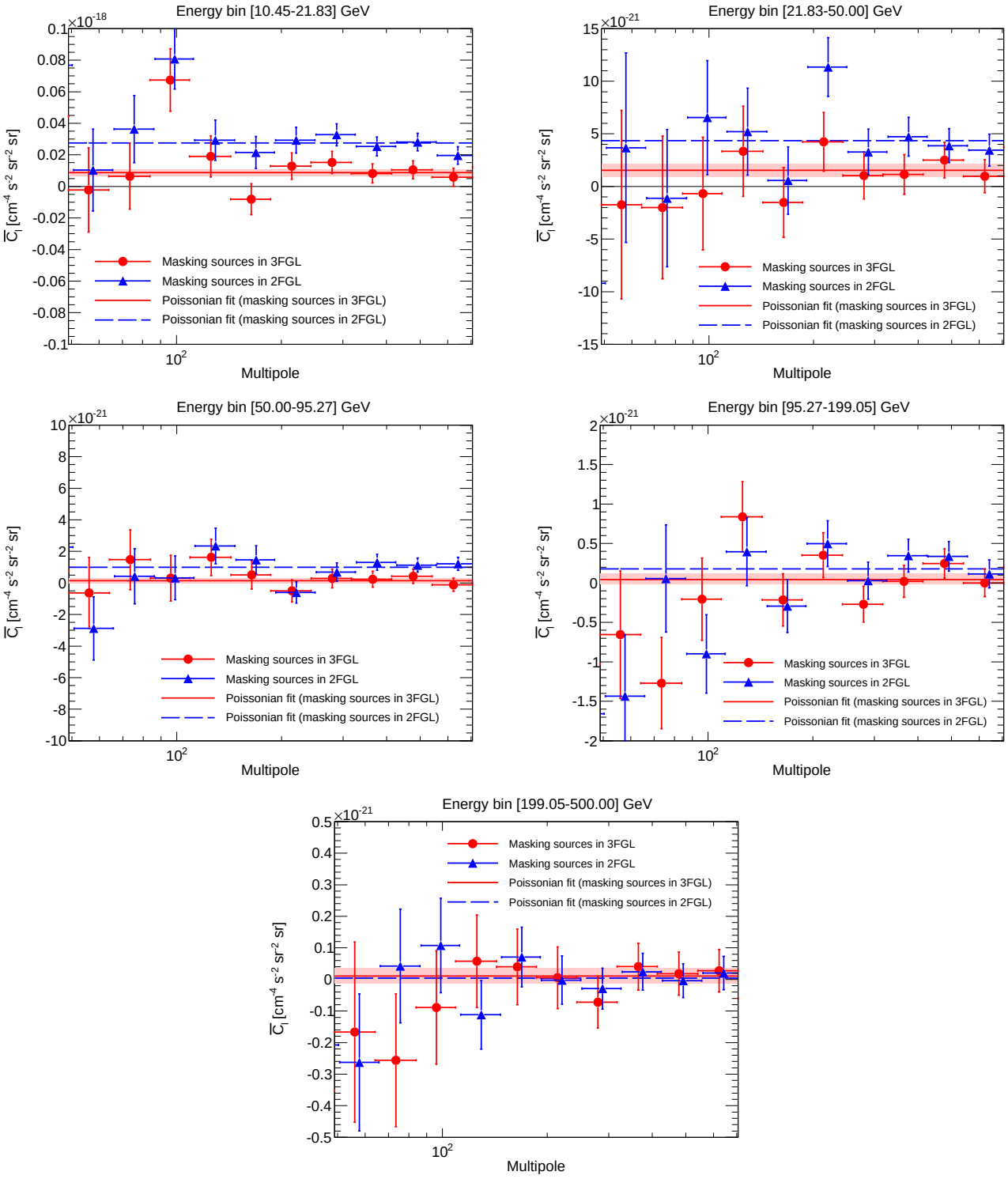

FIG. 30. Same as Fig. 29 but for the last 7 energy bins.

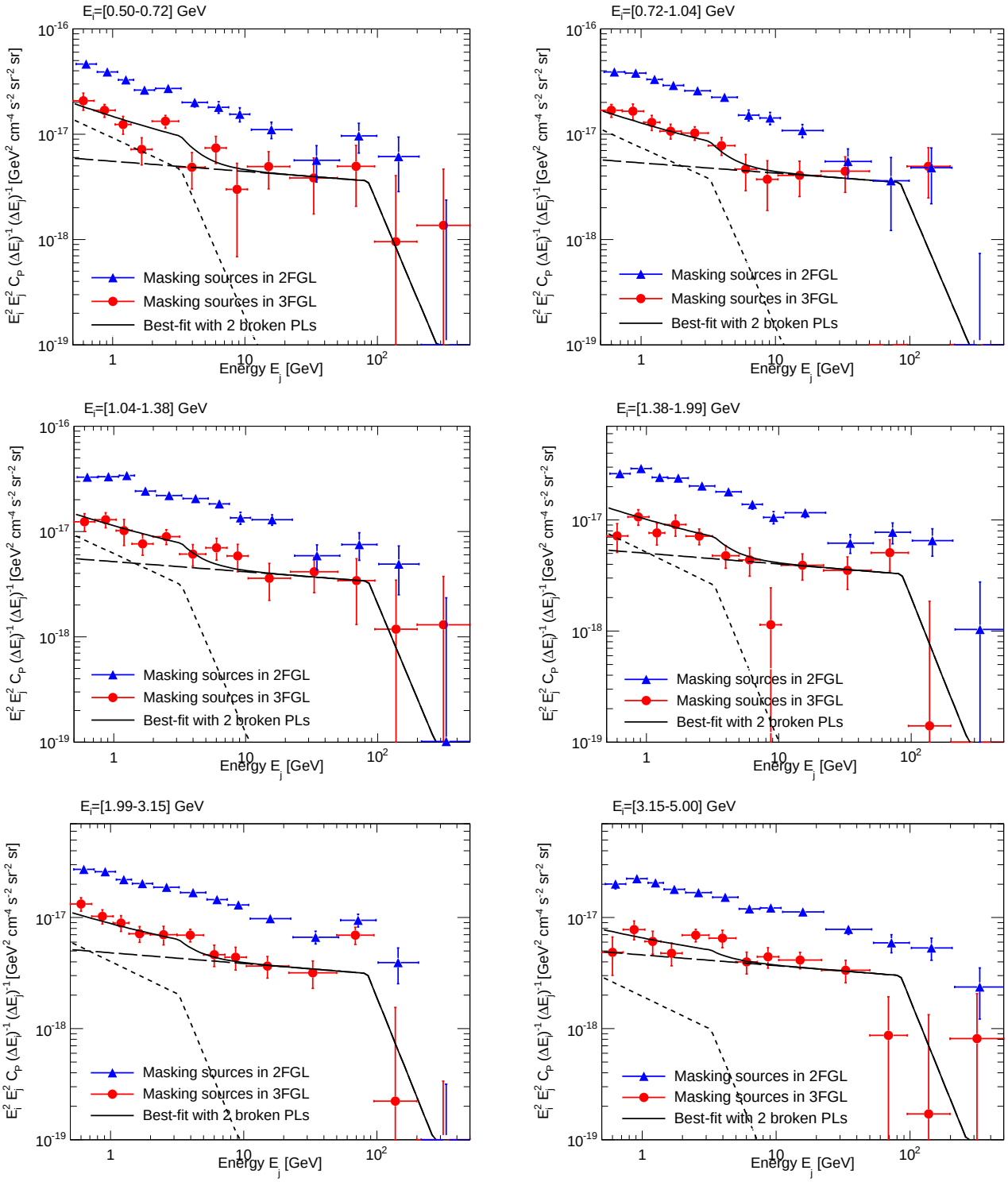

FIG. 31. Depedence of the cross-APS on the energy. Each panel shows the best-fit Poissonian $C_{\rm P}$ for the cross-APS between the i-th and the j-th energy bins, as a function of E_j. Red circles are for the reference data set (P7REP_ULTRACLEAN_V15 front events) using the default mask masking 3FGL sources, while the blue triangles show the result for the same data set and for the default mask excluding 2FGL sources. The first 6 energy bins are shown in this figure and E_i is indicated in the top of each panel. The solid black line is the best-fit solution when data are fitted assuming two independent populations of sources with broken-power-law energy spectra. The short-dashed and long-dashed black lines show the two populations independently.

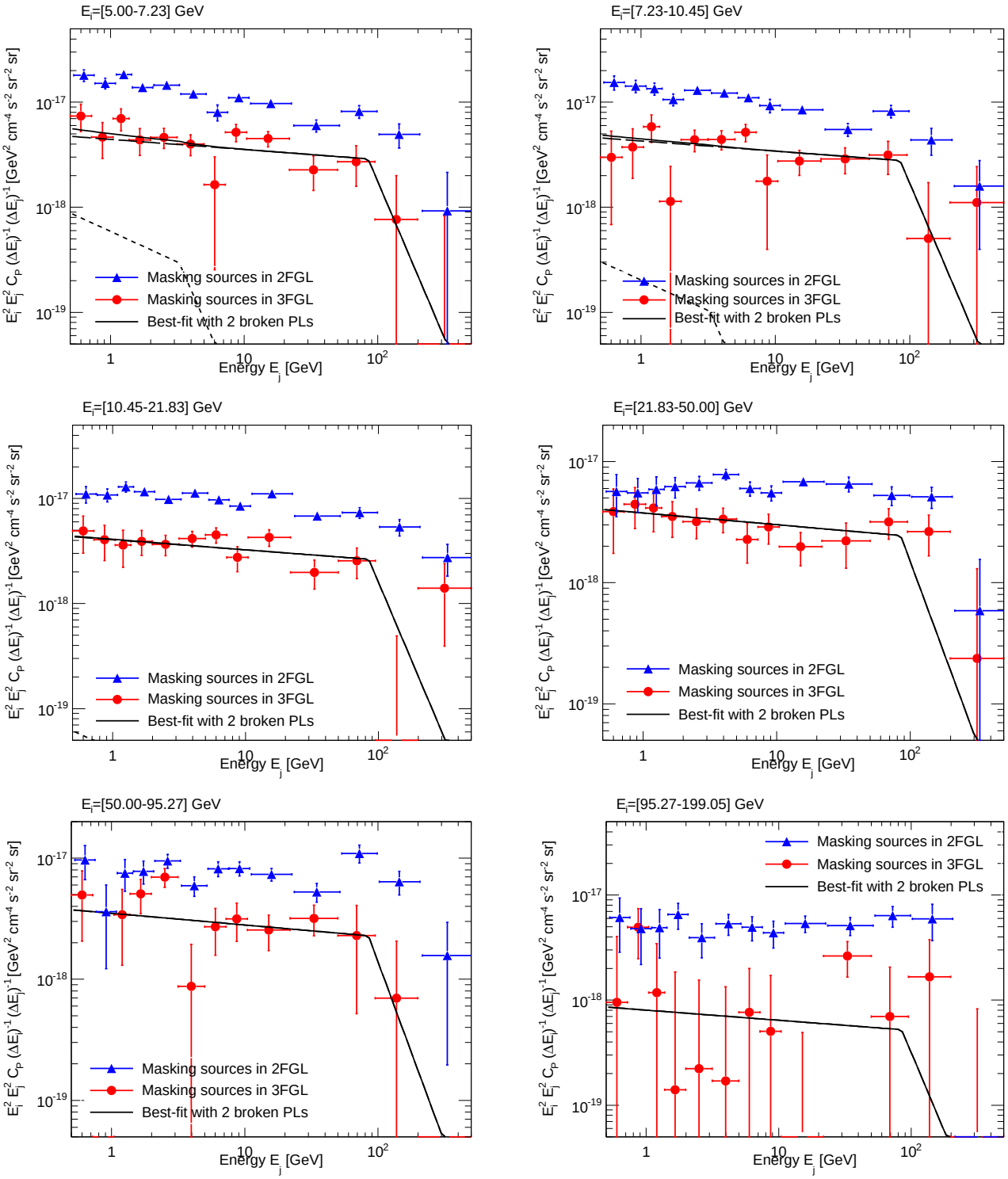
E_i=[5.00-7.23] GeV
E_i=[7.23-10.45] GeV
E_i=[10.45-21.83] GeV
E_i=[21.83-50.00] GeV
E_i=[50.00-95.27] GeV
E_i=[95.27-199.05] GeV
E_i^2 E_j^2 C_P (ΔE_j)^-1 (ΔE_j)^-1 [GeV^2 cm^-4 s^-2 sr^-2 sr]
Energy E_j [GeV]
Masking sources in 2FGL
Masking sources in 3FGL
Best-fit with 2 broken PLs

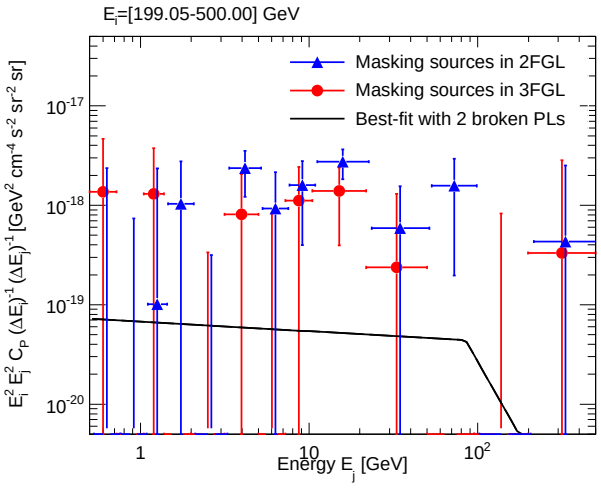

FIG. 32. Same as Fig. 31, for the last 7 energy bins.

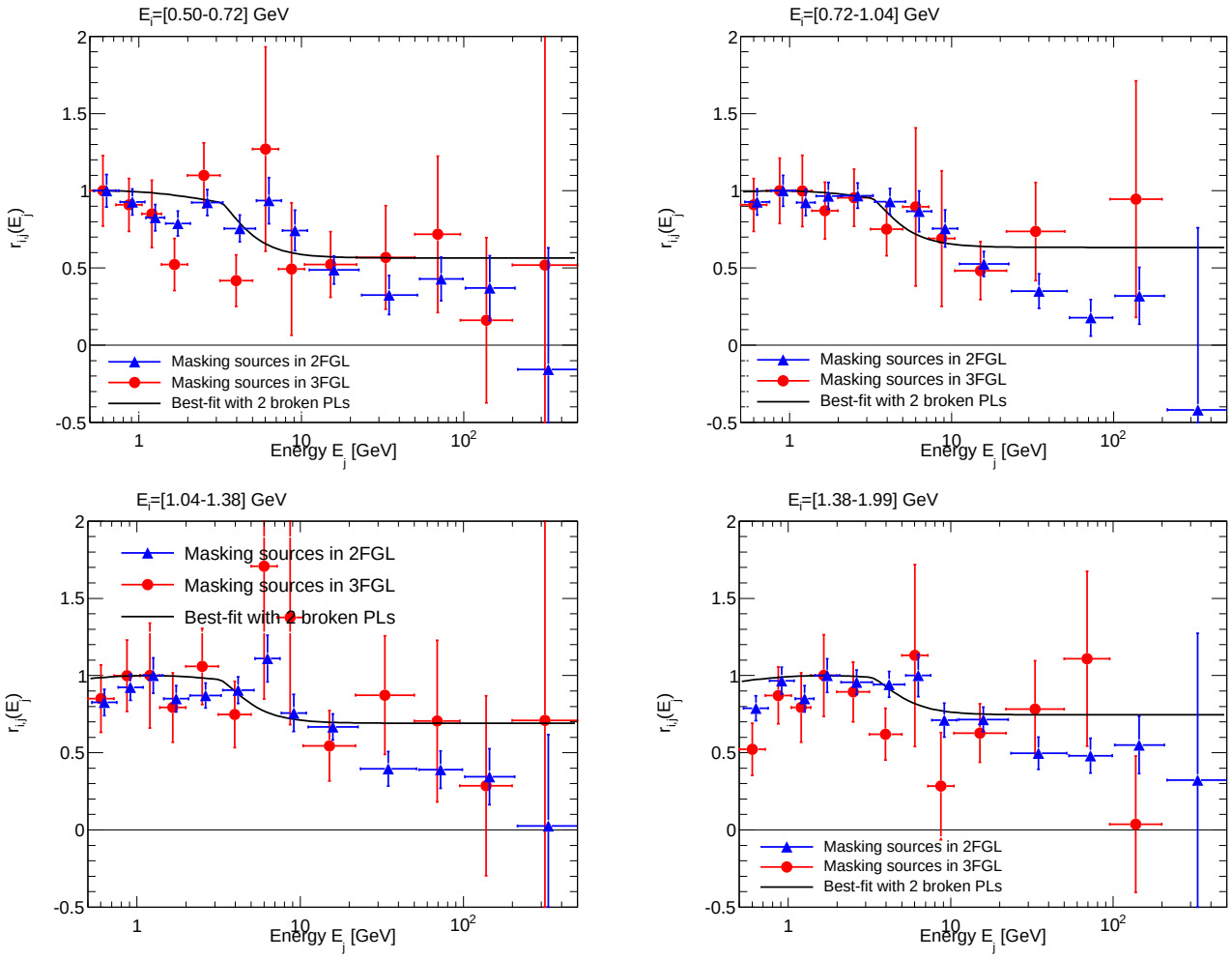

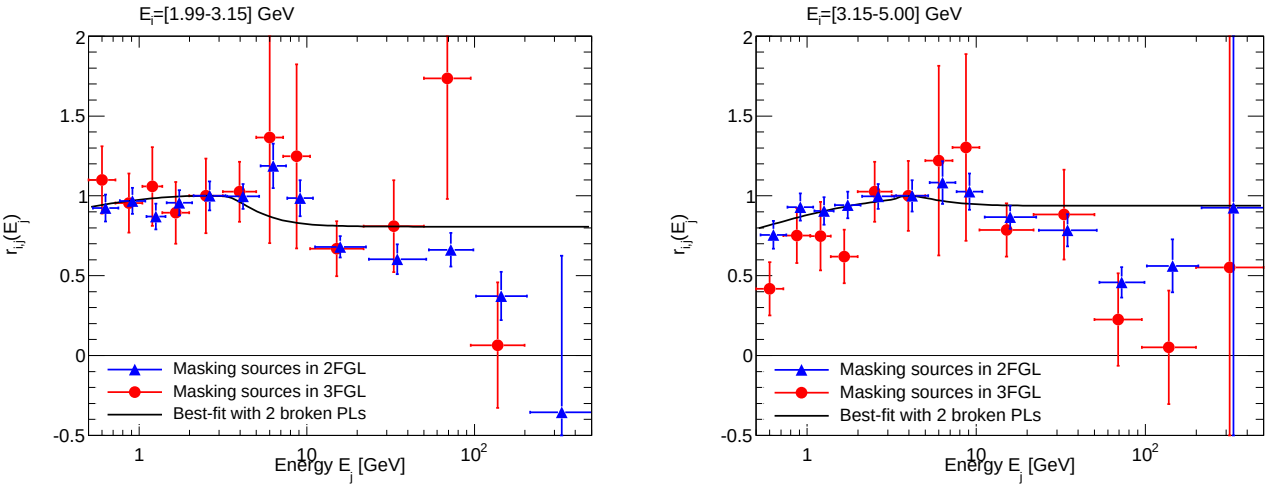

FIG. 33. Dependence of the cross-correlation coefficients on the energy. Each panel shows the cross-correlation coefficients $r_{i,j}$ defined in Sec. V B between the i-th and the j-th energy bins, as a function of E_j. Red circles are for the reference data set (P7REP_ULTRACLEAN_V15 front events) using the default mask masking 3FGL sources, while the blue triangles show the result for the same data set and for the default mask excluding 2FGL sources. The first 6 energy bins are shown in this figure and E_i is indicated in the top of each panel. The solid black line shows the $r_{i,j}$ corresponding to the best-fit solution when data are fitted masking 3FGL sources and assuming two independent populations of sources with broken-power-law energy spectra (see Sec. VI).

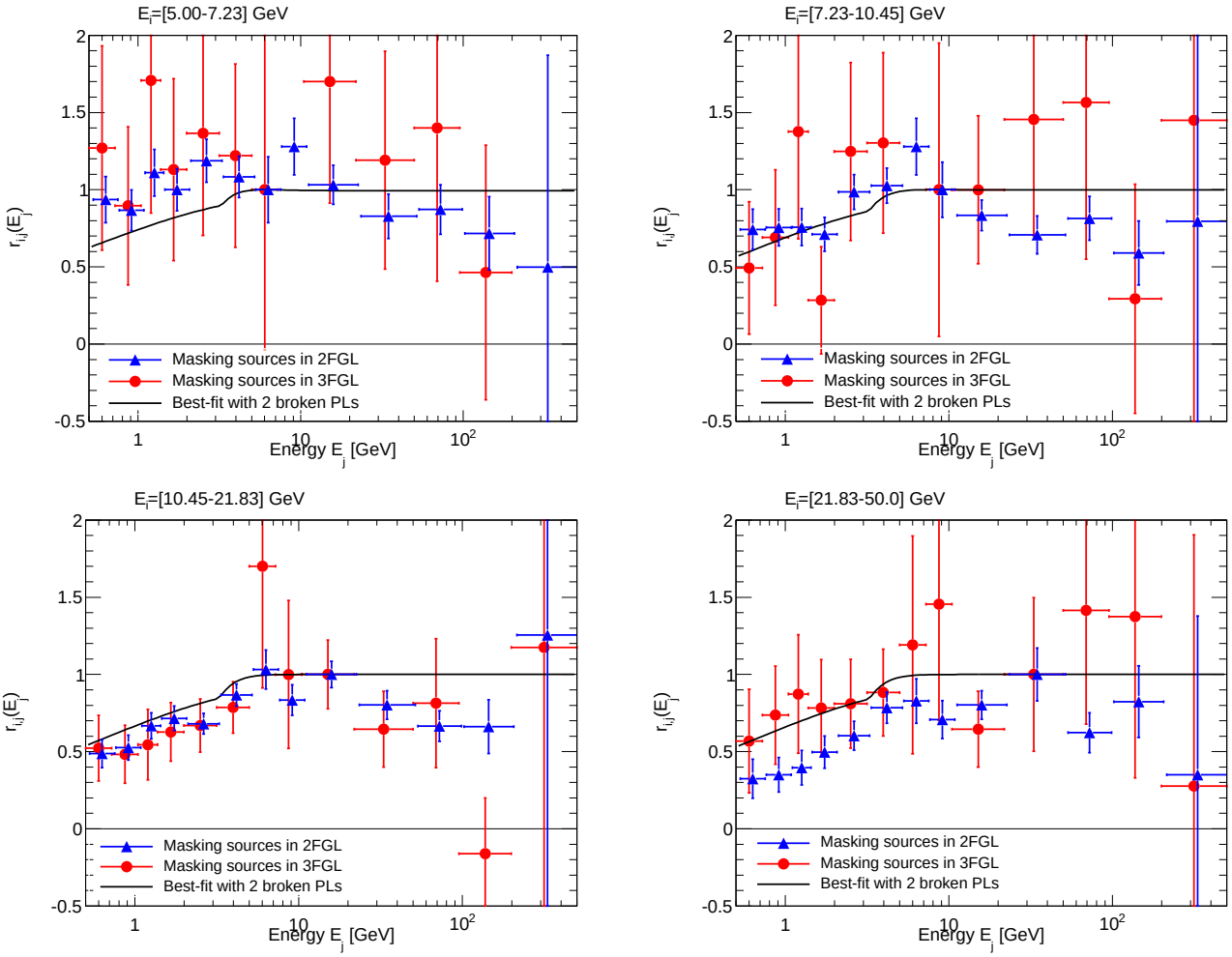

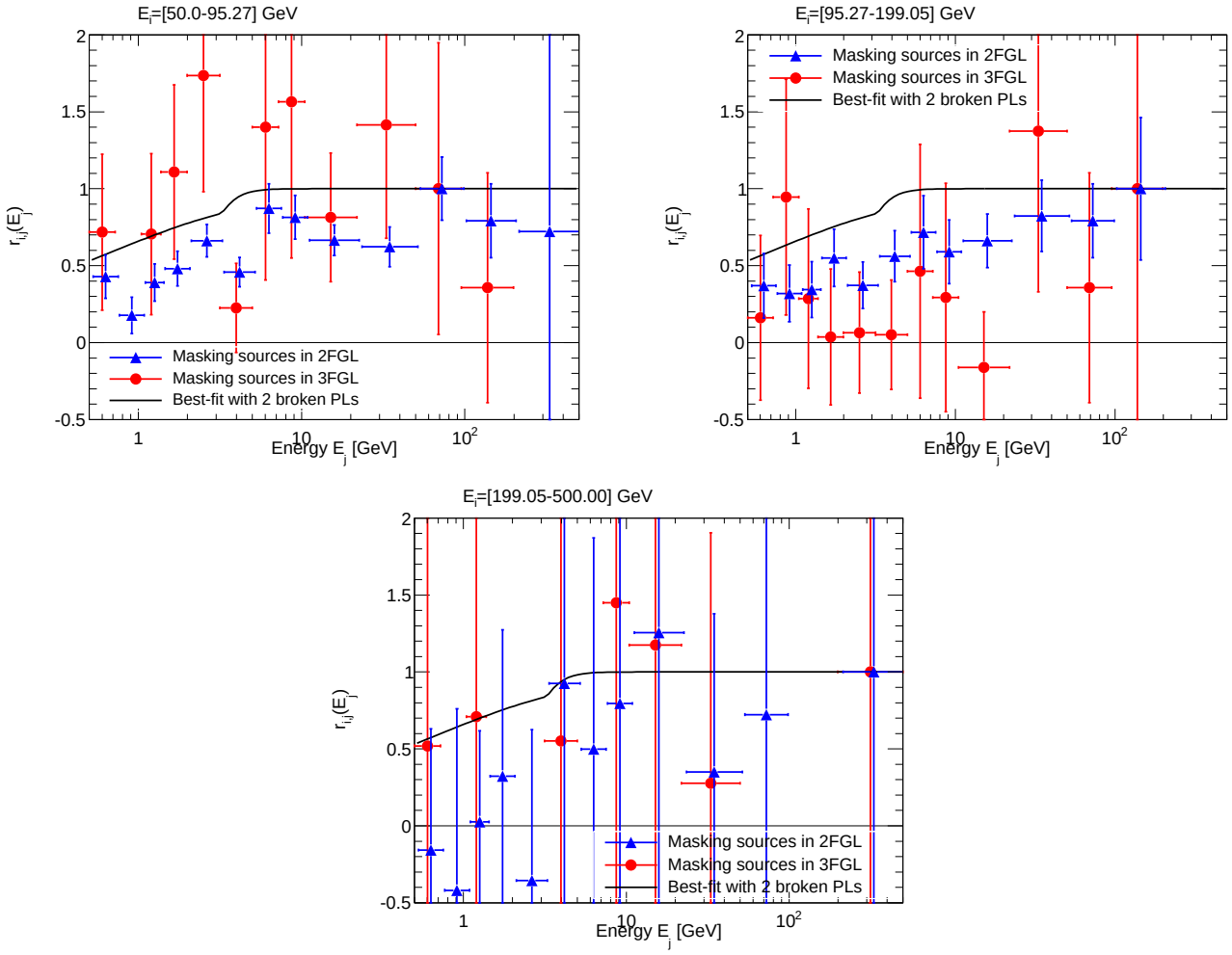

FIG. 34. Same as Fig. 33, for the last 7 energy bins.

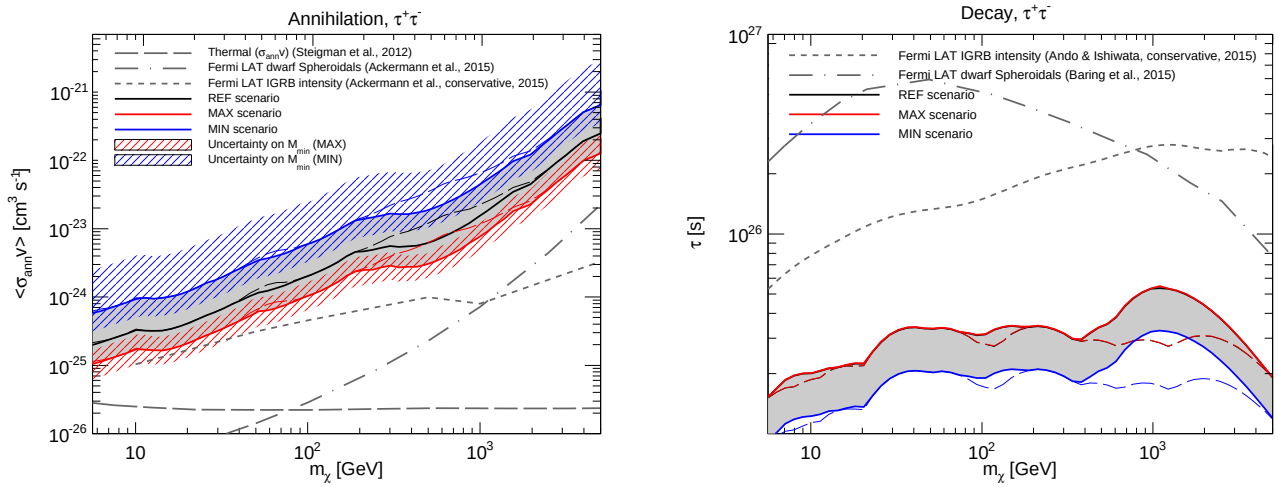

FIG. 35. Conservative exclusion limits on annihilating and decaying DM from the new APS measurement, for the τ channel. *Left:* The solid lines show the upper limits on $\langle\sigma_{\rm ann}v\rangle$ derived from the auto- and cross-APS measured in Sec. III, as a function of m_χ, for $M_{\rm min} = 10^{-6}M_\odot$ and annihilations into $\tau^+\tau^-$. The limits follow the conservative approach described in Sec. VIII A. The black line is for the REF scenario, while the red and blue ones are for MAX and MIN. The grey band between the MIN and MAX scenario represents our estimated total astrophysical uncertainty for $M_{\rm min} = 10^{-6}M_\odot$, accounting for all the sources of uncertainty mentioned in Sec. VII. The red and blue shaded bands describe the effect of changing $M_{\rm min}$ between $10^{-12}M_{\rm min}$ and 1 $M_{\rm min}$, for the MAX and MIN scenario, respectively. In the case of the black, red and blue dashed lines, the upper limits are derived only considering the measured auto-APS and neglecting the cross-APS. For comparison, the long-dashed grey line marks the annihilation cross section for thermal relics from Ref. [94] and the dash-dotted grey line the upper limit obtained in Ref. [95] from the combined analysis of 15 dwarf spheroidal galaxies. Finally, the short-dashed grey line shows the conservative upper limit derived in Ref. [31] from the intensity of the IGRB. *Right*: The same as in the left panel but for the lower limits on τ for decaying DM. The short-dashed grey line represents the lower limit obtained in Fig. 6 of Ref. [96] from the IGRB intensity, while the dash-dotted grey one is obtained from the combined analysis of 15 dwarf spheroidal galaxies in Ref. [97].

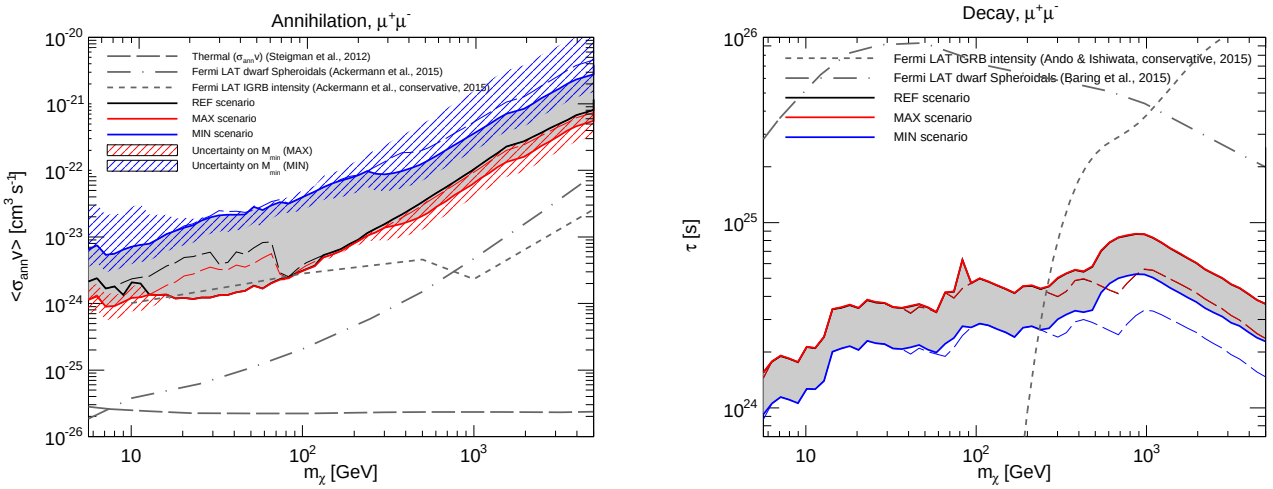

FIG. 36. Same as Fig. 35 but for annihilations/decays into $\mu^+\mu^-$.

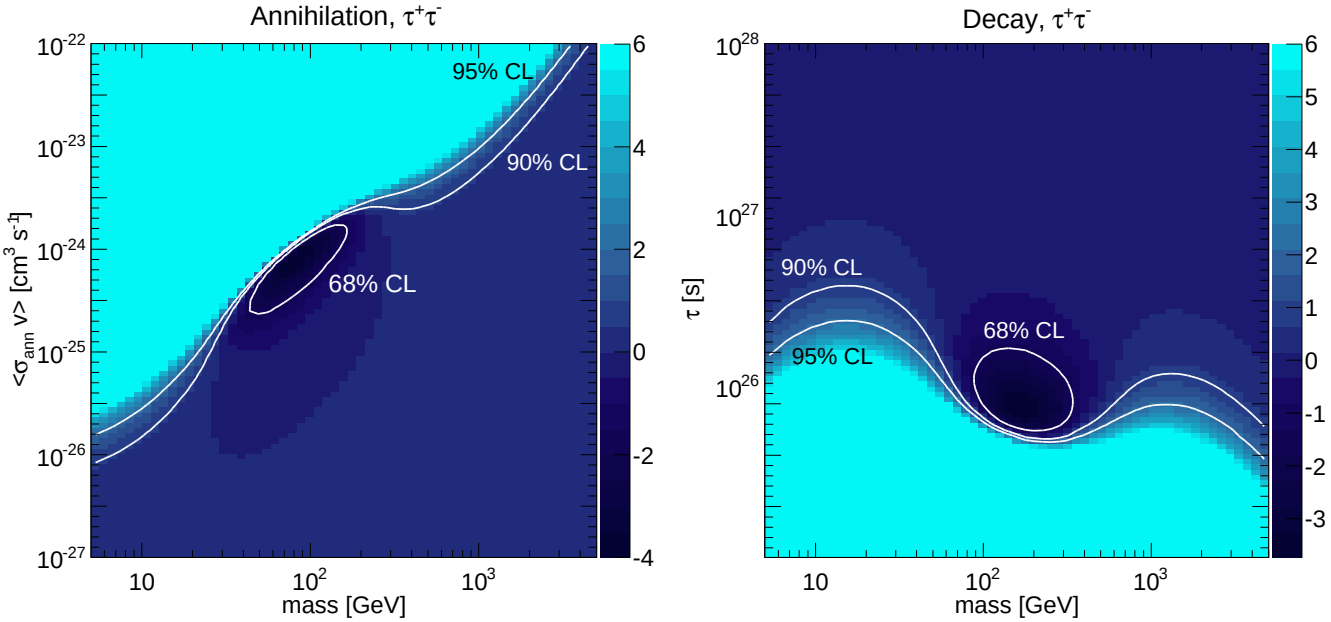

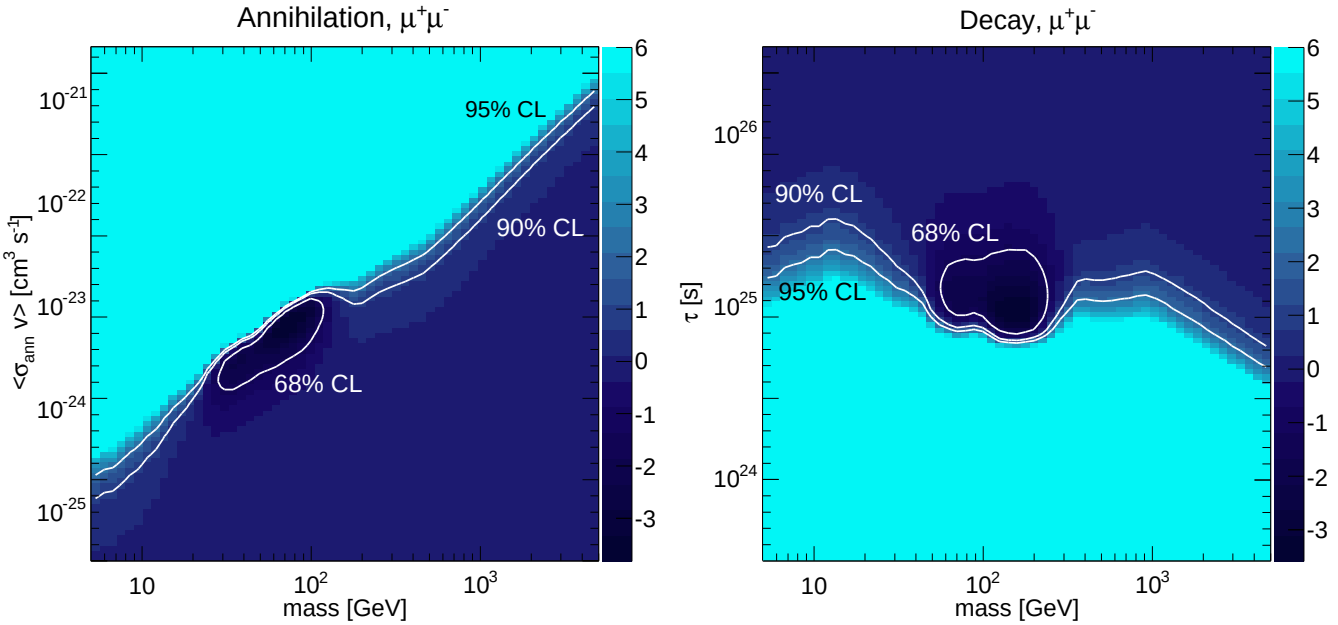

FIG. 37. $\Delta\chi^2$ between the best-fit solution for the 2-component scenario and the best fit of the null hypothesis. Results presented here refer to the REF scenario with $M_{\rm min} = 10^{-6} M_\odot/h$ and annihilation/decay into $\tau^+\tau^-$ (top panels) or $\mu^+\mu^-$ (bottom panels). The panels on the left are for annihilating DM and the ones on the right for decaying DM. Each point in the bi-dimensional parameter space is colored according to its $\Delta\chi^2$, i.e. the difference between the χ^2 of the best fit to the auto- and cross-APS in terms of the 2-component model and the χ^2 of the best fit of the null hypothesis (i.e. no DM). The closed white contour marks the 68% CL region. The 90% and 95% CL ones in the left (right) panels contain all the region below (above) the white open curves labelled "90% CL" and "95% CL".

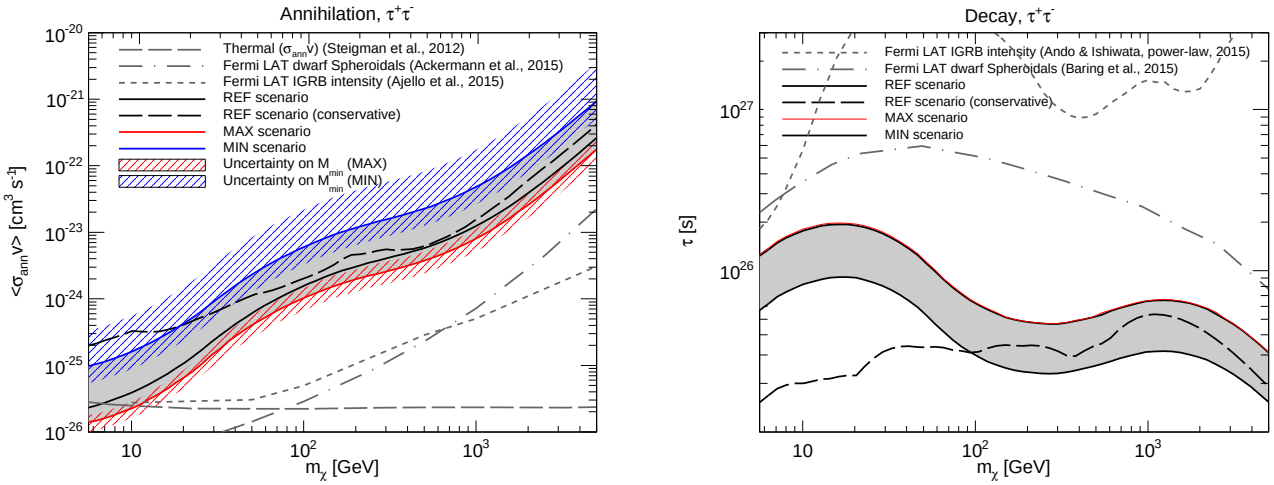

FIG. 38. Exclusion limits on annihilating and decaying DM (for the τ channel) from the fit to the binned $\overline{C_\ell}$ in terms of the 2-component model. *Left:* The solid lines show the upper limits that can be derived on $\langle\sigma_{\rm ann}v\rangle$ as a function of m_χ (for annihilation into $\tau^+\tau^-$ quarks and $M_{\rm min} = 10^{-6}M_\odot$) by fitting the *Fermi* LAT data with a 2-component model that includes astrophysical sources and DM (see text for details). The black, blue and red lines correspond to the REF, MIN and MAX scenario. The blue and red shaded areas indicate how the MIN and MAX upper limits change when leaving $M_{\rm min}$ free to vary between $10^{-12}M_\odot$ and 1 $M_\odot$. The black dashed line is the REF upper limit in the conservative case, from Fig. 35, while the long-dashed grey line is the thermal annihilation cross section from Ref. [94]. The dot-dashed line is the upper limits derived in Ref. [95] from the combined analysis of 15 dwarf spheroidals, while the short-dashed grey line comes from the analysis of the IGRB intensity performed in Ref. [98]. *Right*: The same as in the left panel but for the lower limits on τ, in the case of decaying DM. The short-dashed grey line represents the lower limit obtained in Ref. [96] from the IGRB intensity. The line is taken from Fig. 5 of Ref. [96], where the IGRB is interpreted in terms of a component with a power-law emission spectrum and a DM contribution. Finally, the dot-dashed grey line is the upper limit from the analysis of 15 dwarf spheroidal galaxies performed in Ref. [97].

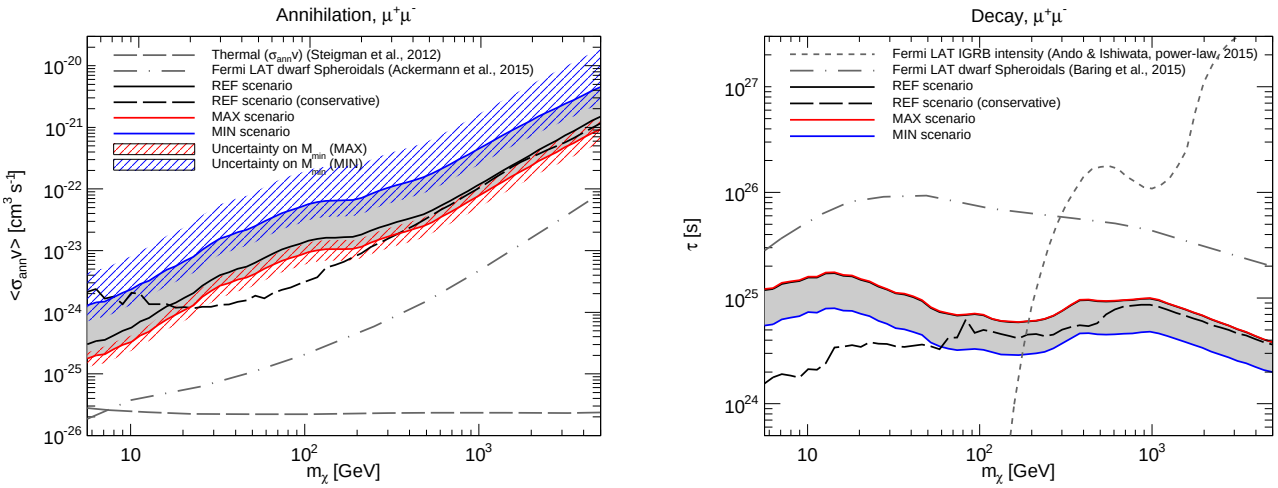

FIG. 39. Same as in Fig. 38 but for annihilations/decays into $\mu^+\mu^-$.

TABLES

TABLE I. Best-fit Poisson auto- and cross-APS $C_{\rm P}$ for the default data set and for the mask covering all sources in 3FGL, in units of $\rm cm^{-4}s^{-2}sr^{-1}$. The numbers in italics indicate the significance of the detection in units of standard deviation (see text), while the numbers in bold give the χ^2 associated with the corresponding $C_{\rm P}$. The entries marked in grey correspond to the auto-APS.

Energy bin [GeV]	0.50-0.72	0.72-1.04	1.04-1.38	1.38-1.99	1.99-3.15	3.15-5.00	5.00-7.23	7.23-10.45	10.45-21.83	21.83-50.00	50.00-95.27	95.27-199.05	199.05-500.00
0.50-0.72	$(7.88 \pm 1.47) \times 10^{-18}$ *6.2*, **5.76**												
0.72-1.04	$(4.42 \pm 0.62) \times 10^{-18}$ *7.1*, **4.12**	$(3.00 \pm 0.52) \times 10^{-18}$ *6.3*, **8.52**											
1.04-1.38	$(1.76 \pm 0.34) \times 10^{-18}$ *5.1*, **14.43**	$(1.28 \pm 0.21) \times 10^{-18}$ *6.2*, **18.03**	$(5.45 \pm 1.51) \times 10^{-19}$ *3.7*, **5.36**										
1.38-1.99	$(9.92 \pm 2.86) \times 10^{-19}$ *3.5*, **15.34**	$(1.02 \pm 0.16) \times 10^{-18}$ *6.2*, **13.19**	$(3.95 \pm 0.88) \times 10^{-19}$ *4.5*, **2.58**	$(4.56 \pm 0.98) \times 10^{-19}$ *4.9*, **26.21**									
1.99-3.15	$(1.51 \pm 0.21) \times 10^{-18}$ *7.4*, **3.91**	$(8.12 \pm 1.18) \times 10^{-19}$ *6.9*, **5.68**	$(3.83 \pm 0.62) \times 10^{-19}$ *6.2*, **8.85**	$(2.96 \pm 0.48) \times 10^{-19}$ *6.2*, **8.40**	$(2.41 \pm 0.46) \times 10^{-19}$ *5.6*, **2.17**								
3.15-5.00	$(3.51 \pm 1.32) \times 10^{-19}$ *2.7*, **8.39**	$(3.89 \pm 0.75) \times 10^{-19}$ *5.2*, **15.75**	$(1.65 \pm 0.39) \times 10^{-19}$ *4.3*, **8.83**	$(1.25 \pm 0.29) \times 10^{-19}$ *4.3*, **8.84**	$(1.51 \pm 0.19) \times 10^{-19}$ *7.8*, **7.62**	$(8.94 \pm 1.60) \times 10^{-20}$ *5.8*, **9.21**							
5.00-7.23	$(2.81 \pm 0.82) \times 10^{-19}$ *3.4*, **8.25**	$(1.22 \pm 0.46) \times 10^{-19}$ *2.7*, **6.64**	$(9.96 \pm 2.35) \times 10^{-20}$ *4.3*, **1.79**	$(6.02 \pm 1.73) \times 10^{-20}$ *3.5*, **14.43**	$(5.29 \pm 1.15) \times 10^{-20}$ *4.7*, **5.55**	$(2.88 \pm 0.64) \times 10^{-20}$ *4.5*, **10.33**	$(6.23 \pm 5.26) \times 10^{-21}$ *1.2*, **9.48**						
7.23-10.24	$(7.86 \pm 6.06) \times 10^{-20}$ *1.3*, **15.77**	$(6.79 \pm 3.36) \times 10^{-20}$ *2.0*, **4.47**	$(5.77 \pm 1.69) \times 10^{-20}$ *3.4*, **7.64**	$(1.09 \pm 1.26) \times 10^{-20}$ *0.9*, **6.29**	$(3.47 \pm 0.81) \times 10^{-20}$ *4.3*, **2.67**	$(2.21 \pm 0.46) \times 10^{-20}$ *4.9*, **15.62**	$(1.36 \pm 0.25) \times 10^{-20}$ *5.3*, **8.11**	$(3.22 \pm 2.50) \times 10^{-21}$ *1.3*, **4.61**					
10.24-21.83 21.83	$(1.51 \pm 0.58) \times 10^{-19}$ *2.6*, **6.15**	$(8.63 \pm 3.18) \times 10^{-20}$ *2.7*, **4.63**	$(4.15 \pm 1.60) \times 10^{-20}$ *2.6*, **4.90**	$(4.37 \pm 1.16) \times 10^{-20}$ *3.8*, **6.66**	$(3.39 \pm 0.75) \times 10^{-20}$ *4.6*, **6.90**	$(2.43 \pm 0.41) \times 10^{-20}$ *5.9*, **12.80**	$(1.38 \pm 0.23) \times 10^{-20}$ *6.0*, **4.40**	$(5.85 \pm 1.56) \times 10^{-21}$ *3.7*, **11.35**	$(1.06 \pm 0.19) \times 10^{-20}$ *5.6*, **13.87**				
21.83-50.00	$(6.13 \pm 3.35) \times 10^{-20}$ *1.8*, **14.23**	$(4.90 \pm 1.82) \times 10^{-20}$ *2.7*, **5.22**	$(2.47 \pm 0.91) \times 10^{-20}$ *2.7*, **11.01**	$(2.03 \pm 0.66) \times 10^{-20}$ *3.0*, **4.13**	$(1.53 \pm 0.42) \times 10^{-20}$ *3.6*, **8.44**	$(1.01 \pm 0.23) \times 10^{-20}$ *4.4*, **9.82**	$(3.61 \pm 1.31) \times 10^{-21}$ *2.8*, **6.50**	$(3.17 \pm 0.88) \times 10^{-21}$ *3.6*, **4.52**	$(2.56 \pm 0.79) \times 10^{-21}$ *3.3*, **18.78**	$(1.47 \pm 0.60) \times 10^{-21}$ *2.5*, **3.08**			
50.00-95.27 95.27	$(2.90 \pm 1.69) \times 10^{-20}$ *1.7*, **10.92**	$(-1.34 \pm 0.93) \times 10^{-20}$ *1.4*, **11.02**	$(7.50 \pm 4.63) \times 10^{-21}$ *1.6*, **10.31**	$(1.08 \pm 0.34) \times 10^{-20}$ *3.2*, **5.82**	$(1.23 \pm 0.22) \times 10^{-20}$ *5.7*, **2.86**	$(0.97 \pm 1.18) \times 10^{-21}$ *0.8*, **9.59**	$(1.59 \pm 0.66) \times 10^{-21}$ *2.4*, **9.41**	$(1.28 \pm 0.44) \times 10^{-21}$ *2.9*, **13.96**	$(1.21 \pm 0.39) \times 10^{-21}$ *3.0*, **5.61**	$(7.82 \pm 2.22) \times 10^{-22}$ *3.6*, **1.29**	$(2.07 \pm 1.60) \times 10^{-22}$ *1.3*, **4.07**		
95.27-199.05	$(0.32 \pm 1.04) \times 10^{-20}$ *0.3*, **5.10**	$(1.16 \pm 0.58) \times 10^{-20}$ *2.0*, **8.35**	$(1.49 \pm 2.88) \times 10^{-21}$ *0.5*, **5.55**	$(0.17 \pm 2.10) \times 10^{-21}$ *0.1*, **1.16**	$(0.23 \pm 1.35) \times 10^{-21}$ *0.2*, **7.96**	$(1.09 \pm 7.48) \times 10^{-22}$ *0.2*, **6.23**	$(2.58 \pm 4.15) \times 10^{-22}$ *0.6*, **11.13**	$(1.18 \pm 2.84) \times 10^{-22}$ *0.4*, **7.34**	$(-1.17 \pm 2.52) \times 10^{-22}$ *0.5*, **2.59**	$(3.72 \pm 1.38) \times 10^{-22}$ *2.7*, **4.39**	$(3.63 \pm 7.09) \times 10^{-23}$ *0.5*, **4.25**	$(4.98 \pm 6.30) \times 10^{-23}$ *0.7*, **14.18**	
199.05-500.0	$(2.54 \pm 6.16) \times 10^{-21}$ *0.4*, **7.64**	$(-4.13 \pm 3.43) \times 10^{-21}$ *1.2*, **5.81**	$(0.91 \pm 1.71) \times 10^{-21}$ *0.5*, **6.99**	$(-1.77 \pm 1.26) \times 10^{-21}$ *1.4*, **9.91**	$(-6.13 \pm 8.02) \times 10^{-22}$ *0.8*, **9.07**	$(2.87 \pm 4.44) \times 10^{-22}$ *0.6*, **11.64**	$(-0.97 \pm 2.51) \times 10^{-22}$ *0.4*, **5.83**	$(1.43 \pm 1.71) \times 10^{-22}$ *0.8*, **5.30**	$(2.11 \pm 1.52) \times 10^{-22}$ *1.4*, **3.42**	$(1.85 \pm 8.33) \times 10^{-23}$ *0.2*, **3.61**	$(-4.93 \pm 4.32) \times 10^{-23}$ *1.1*, **4.72**	$(-1.37 \pm 2.74) \times 10^{-23}$ *0.5*, **4.82**	$(0.30 \pm 2.30) \times 10^{-23}$ *0.1*, **3.64**

TABLE II. Same as Tab. I but with the mask covering the sources in 2FGL. Data are available at https://www-glast.stanford.edu/pub_data/552.

Energy bin [GeV]	0.50-0.72	0.72-1.04	1.04-1.38	1.38-1.99	1.99-3.15	3.15-5.00	5.00-7.23	7.23-10.45	10.45-21.83	21.83-50.00	50.00-95.27	95.27-199.05	199.05-500.00
0.50-0.72	$(1.76 \pm 0.15) \times 10^{-17}$ *14.7*, **8.81**												
0.72-1.04	$(1.02 \pm 0.07) \times 10^{-17}$ *15.2*, **7.52**	$(6.92 \pm 0.56) \times 10^{-18}$ *15.5*, **14.61**											
1.04-1.38	$(4.66 \pm 0.38) \times 10^{-18}$ *12.6*, **5.82**	$(3.27 \pm 0.22) \times 10^{-18}$ *14.9*, **12.07**	$(1.81 \pm 0.17) \times 10^{-18}$ *12.7*, **11.35**										
1.38-1.99	$(3.61 \pm 0.30) \times 10^{-18}$ *12.0*, **14.57**	$(2.78 \pm 0.19) \times 10^{-18}$ *15.8*, **8.59**	$(1.25 \pm 0.09) \times 10^{-18}$ *13.4*, **4.76**	$(1.19 \pm 0.11) \times 10^{-18}$ *13.2*, **20.84**									
1.99-3.15	$(3.11 \pm 0.22) \times 10^{-18}$ *14.3*, **3.85**	$(2.04 \pm 0.13) \times 10^{-18}$ *16.4*, **9.66**	$(9.40 \pm 0.66) \times 10^{-19}$ *14.5*, **8.88**	$(8.39 \pm 0.49) \times 10^{-19}$ *16.8*, **12.20**	$(6.44 \pm 0.48) \times 10^{-19}$ *15.3*, **9.72**								
3.15-5.00	$(1.45 \pm 0.14) \times 10^{-18}$ *10.5*, **7.55**	$(1.12 \pm 0.08) \times 10^{-18}$ *14.4*, **23.99**	$(5.56 \pm 0.40) \times 10^{-19}$ *13.9*, **14.04**	$(4.70 \pm 0.30) \times 10^{-19}$ *15.7*, **7.33**	$(3.65 \pm 0.20) \times 10^{-19}$ *18.5*, **4.52**	$(2.08 \pm 0.17) \times 10^{-19}$ *14.0*, **14.77**							
5.00-7.23	$(6.86 \pm 0.87) \times 10^{-19}$ *8.1*, **13.94**	$(3.98 \pm 0.47) \times 10^{-19}$ *8.4*, **4.62**	$(2.61 \pm 0.25) \times 10^{-19}$ *10.9*, **4.61**	$(1.91 \pm 0.18) \times 10^{-19}$ *10.7*, **11.95**	$(1.66 \pm 0.12) \times 10^{-19}$ *14.4*, **5.02**	$(8.63 \pm 0.68) \times 10^{-20}$ *13.2*, **11.26**	$(3.05 \pm 0.53) \times 10^{-20}$ *6.0*, **9.03**						
7.23-10.24	$(4.06 \pm 0.63) \times 10^{-19}$ *6.5*, **14.30**	$(2.59 \pm 0.35) \times 10^{-19}$ *7.5*, **9.69**	$(1.33 \pm 0.18) \times 10^{-19}$ *7.6*, **12.06**	$(1.01 \pm 0.13) \times 10^{-19}$ *7.9*, **2.92**	$(1.03 \pm 0.08) \times 10^{-19}$ *12.6*, **9.20**	$(6.10 \pm 0.45) \times 10^{-20}$ *13.4*, **13.67**	$(2.91 \pm 0.25) \times 10^{-20}$ *11.4*, **7.19**	$(1.69 \pm 0.25) \times 10^{-20}$ *7.0*, **5.45**					
10.24-21.83	$(3.39 \pm 0.60) \times 10^{-19}$ *5.6*, **13.66**	$(2.30 \pm 0.33) \times 10^{-19}$ *7.0*, **15.13**	$(1.49 \pm 0.17) \times 10^{-19}$ *9.0*, **1.53**	$(1.30 \pm 0.12) \times 10^{-19}$ *10.8*, **13.47**	$(9.07 \pm 0.77) \times 10^{-20}$ *11.9*, **2.82**	$(6.57 \pm 0.42) \times 10^{-20}$ *15.6*, **12.72**	$(2.99 \pm 0.23) \times 10^{-20}$ *12.8*, **13.79**	$(1.80 \pm 0.16) \times 10^{-20}$ *11.4*, **13.18**	$(2.76 \pm 0.19) \times 10^{-20}$ *14.5*, **11.56**				
21.83-50.00	$(9.00 \pm 3.42) \times 10^{-20}$ *2.6*, **14.20**	$(6.08 \pm 1.89) \times 10^{-20}$ *3.2*, **6.29**	$(3.52 \pm 0.94) \times 10^{-20}$ *3.8*, **8.80**	$(3.58 \pm 0.69) \times 10^{-20}$ *5.3*, **4.51**	$(3.19 \pm 0.42) \times 10^{-20}$ *7.5*, **6.94**	$(2.36 \pm 0.23) \times 10^{-20}$ *10.1*, **11.18**	$(9.54 \pm 1.27) \times 10^{-21}$ *7.4*, **12.72**	$(6.07 \pm 0.85) \times 10^{-21}$ *7.0*, **6.34**	$(8.79 \pm 0.75) \times 10^{-21}$ *11.2*, **17.72**	$(4.35 \pm 0.61) \times 10^{-21}$ *7.4*, **9.31**			
50.00-95.27	$(5.66 \pm 1.77) \times 10^{-20}$ *3.2*, **10.32**	$(1.46 \pm 0.97) \times 10^{-20}$ *1.5*, **7.70**	$(1.65 \pm 0.48) \times 10^{-20}$ *3.4*, **11.91**	$(1.65 \pm 0.35) \times 10^{-20}$ *4.7*, **4.67**	$(1.67 \pm 0.22) \times 10^{-20}$ *7.6*, **5.76**	$(6.58 \pm 1.21) \times 10^{-21}$ *5.4*, **15.15**	$(4.79 \pm 0.67) \times 10^{-21}$ *7.1*, **9.64**	$(3.33 \pm 0.45) \times 10^{-21}$ *7.3*, **10.32**	$(3.48 \pm 0.41) \times 10^{-21}$ *8.5*, **7.88**	$(1.29 \pm 0.23) \times 10^{-21}$ *5.8*, **12.85**	$(9.88 \pm 1.66) \times 10^{-22}$ *6.1*, **12.39**		
95.27-199.05	$(2.07 \pm 1.10) \times 10^{-20}$ *1.9*, **9.32**	$(1.12 \pm 0.61) \times 10^{-20}$ *1.8*, **7.93**	$(6.20 \pm 3.02) \times 10^{-21}$ *2.0*, **16.59**	$(8.01 \pm 2.22) \times 10^{-21}$ *3.6*, **4.21**	$(3.99 \pm 1.42) \times 10^{-21}$ *2.8*, **8.62**	$(3.41 \pm 0.77) \times 10^{-21}$ *4.4*, **5.85**	$(1.67 \pm 0.43) \times 10^{-21}$ *3.9*, **4.06**	$(1.02 \pm 0.29) \times 10^{-21}$ *3.5*, **11.83**	$(1.46 \pm 0.26) \times 10^{-21}$ *5.6*, **3.72**	$(7.23 \pm 1.43) \times 10^{-22}$ *5.0*, **7.81**	$(3.31 \pm 0.74) \times 10^{-22}$ *4.4*, **2.94**	$(1.77 \pm 0.67) \times 10^{-22}$ *2.6*, **14.31**	
199.05-500.0	$(-1.32 \pm 5.74) \times 10^{-21}$ *0.2*, **4.73**	$(-2.19 \pm 3.14) \times 10^{-21}$ *0.7*, **6.78**	$(0.07 \pm 1.57) \times 10^{-21}$ *<0.1*, **11.42**	$(0.70 \pm 1.17) \times 10^{-21}$ *0.6*, **14.07**	$(-5.67 \pm 7.44) \times 10^{-22}$ *0.8*, **10.48**	$(8.39 \pm 4.08) \times 10^{-22}$ *2.1*, **17.24**	$(1.73 \pm 2.27) \times 10^{-22}$ *0.8*, **6.79**	$(2.05 \pm 1.54) \times 10^{-22}$ *1.3*, **6.92**	$(4.14 \pm 1.38) \times 10^{-22}$ *3.0*, **5.18**	$(4.59 \pm 7.58) \times 10^{-23}$ *0.6*, **9.32**	$(4.51 \pm 3.95) \times 10^{-23}$ *1.1*, **3.97**	$(-3.57 \pm 2.54) \times 10^{-23}$ *1.4*, **9.04**	$(0.39 \pm 1.91) \times 10^{-23}$ *<0.1*, **4.17**

TABLE III. Best-fit values for the parameters defining the populations assumed to describe the measured auto- and cross-APS. See the text for the definition of the parameters. The normalizations (A, A_1 and A_2) are measured in $\mathrm{cm}^{-2}\mathrm{s}^{-1}\mathrm{sr}^{-1}$ and the energy breaks (E_b, $E_{b,1}$ and $E_{b,2}$) are measured in GeV. Errors are given at 68% CL. The table also indicates the number of degrees of freedom $N_{\rm dof}$ (i.e., the number of fitted data points minus the number of free parameters), the χ^2 of the best-fit solution, the χ^2 of the best-fit point per degree of freedom and the corresponding p-value.

								$N_{\rm dof}$	χ^2	$\chi^2/N_{\rm dof}$	p-value
One power law											
$\log_{10}(A)$	α										
$-8.48^{+0.01}_{-0.01}$	$2.29^{+0.02}_{-0.01}$							89	135.31	1.52	0.001
One broken power law											
$\log_{10}(A)$	α	β	E_b								
$-8.49^{+0.01}_{-0.01}$	$2.26^{+0.02}_{-0.02}$	>3.74 at 68% CL	$92.20^{+16.02}_{-16.66}$					87	118.57	1.36	0.010
Two power laws											
$\log_{10}(A_1)$	α_1	$\log_{10}(A_2)$	α_2								
$-8.52^{+0.03}_{-0.04}$	$2.24^{+0.03}_{-0.05}$	$-8.81^{+0.14}_{-0.22}$	$3.27^{+0.78}_{-0.45}$					87	127.60	1.47	0.003
Two broken power laws											
$\log_{10}(A_1)$	α_1	β_1	$E_{b,1}$	$\log_{10}(A_2)$	α_2	β_2	$E_{b,2}$				
$-8.58^{+0.04}_{-0.05}$	$2.58^{+0.18}_{-0.12}$	>3.49 at 68% CL	$3.26^{+1.05}_{-0.64}$	$-8.64^{+0.04}_{-0.05}$	$2.10^{+0.05}_{-0.05}$	>3.86 at 68% CL	$84.65^{+10.28}_{-15.71}$	83	91.58	1.10	0.240
One power law and one broken power law											
$\log_{10}(A_1)$	α_1	$\log_{10}(A_2)$	α_2	β_2	$E_{b,2}$						
$-8.56^{+0.06}_{-0.09}$	$2.71^{0.26}_{0.18}$	$-8.68^{+0.10}_{-0.13}$	$2.08^{+0.88}_{-0.45}$	>3.89 at 68% CL	$84.79^{10.60}_{16.13}$			85	98.86	1.16	0.140